# NANOELECTRODE BASED DEVICES FOR RAPID PATHOGEN DETECTION AND IDENTIFICATION

by

FORAM RANJEET MADIYAR

B. Pharm., University of Pune, India, 2009

AN ABSTRACT OF A DISSERTATION

submitted in partial fulfillment of the requirements for the degree

DOCTOR OF PHILOSOPHY

Department of Chemistry
College of Arts and Sciences

KANSAS STATE UNIVERSITY
Manhattan, Kansas

2015

# Abstract

Developing new and rapid methods for pathogen detection with enhanced sensitivity and temporal resolution is critical for protecting general public health and implementing the food and water safety standards. In this research vertically aligned carbon nanofiber nanoelectrode arrays (VACNF NEAs) have been explored as a sample manipulation tool and coupled with fluorescence, surface enhanced Raman scattering (SERS) and impedance techniques for pathogen detection and identification.

The key objective for employing a nanoelectrode array is that the nano-Dielectrophoresis (nano-DEP) at the tip of a carbon nanofiber (CNF) acts as a potential trap to capture pathogens. A microfluidic device was fabricated where nanofibers (~ 100 nm in diameter) were placed at the bottom of a fluidic channel to serve as a 'point array' while an indium tin oxide coated glass slide acted as a macroscale counter electrode. The electric field gradient was highly enhanced at the tips of the CNFs when an AC voltage was applied. The first study focused on the capture of the viral particles (*Bacteriophage* T4r) by employing a frequency of 10.0 kHz, a flow velocity of 0.73 mm/sec, and a voltage of 10.0 $V_{pp}$. A *Lithenburg* type of phenomenon was observed, that were drastically different from the isolated spots of bacteria captured on VACNF tips in previous study. At the lowest employed virus concentration ($1 \times 10^4$ pfu/mL), a capture efficiency of 60% was observed with a fluorescence microscope.

The motivation of the second study was to incorporate the SERS detection for specific pathogen identification. Gold-coated iron-oxide nanoovals labeled with Raman Tags (QSY 21), and antibodies that specifically bound with *E.coli* cells were utilized. The optimum capture was observed at a frequency of 100.0 kHz, a flow velocity of 0.40 mm/sec, and a voltage of 10.0 $V_{pp}$.

The detection limit was ~210 CFU/mL for a portable Raman system with a capture time of 50 seconds.

In the final study, a real-time impedance method was employed to detect *Vaccinia* virus (human virus) in the nano-DEP device at 1.0 kHz and 8.0 $V_{pp}$ giving a detection limit of $2.51 \times 10^3$ pfu/mL.

# NANOELECTRODE BASED DEVICES FOR RAPID PATHOGEN DETECTION AND IDENTIFICATION

by

FORAM RANJEET MADIYAR

B. Pharm., University of Pune, India, 2009

A DISSERTATION

submitted in partial fulfillment of the requirements for the degree

DOCTOR OF PHILOSOPHY

Department of Chemistry
College of Arts and Science

KANSAS STATE UNIVERSITY
Manhattan, Kansas

2015

Approved by:

Major Professor
Dr. Jun Li

# Copyright

# Abstract

Developing new and rapid methods for pathogen detection with enhanced sensitivity and temporal resolution is critical for protecting general public health and implementing the food and water safety standards. In this research vertically aligned carbon nanofiber nanoelectrode arrays (VACNF NEAs) have been explored as a sample manipulation tool and coupled with fluorescence, surface enhanced Raman scattering (SERS) and impedance techniques for pathogen detection and identification.

The key objective for employing a nanoelectrode array is that the nano-Dielectrophoresis (nano-DEP) at the tip of a carbon nanofiber (CNF) acts as a potential trap to capture pathogens. A microfluidic device was fabricated where nanofibers (~ 100 nm in diameter) were placed at the bottom of a fluidic channel to serve as a 'point array' while an indium tin oxide coated glass slide acted as a macroscale counter electrode. The electric field gradient was highly enhanced at the tips of the CNFs when an AC voltage was applied. The first study focused on the capture of the viral particles (*Bacteriophage* T4r) by employing a frequency of 10.0 kHz, a flow velocity of 0.73 mm/sec, and a voltage of 10.0 Vpp. A Lithenburg type of phenomenon was observed, that were drastically different from the isolated spots of bacteria captured on VACNF tips in previous study. At the lowest employed virus concentration ($1 \times 10^4$ pfu/mL), a capture efficiency of 60% was observed with a fluorescence microscope.

The motivation of the second study was to incorporate the SERS detection for specific pathogen identification. Gold-coated iron-oxide nanoovals labeled with Raman Tags (QSY 21), and antibodies that specifically bound with *E.coli* cells were utilized. The optimum capture was observed at a frequency of 100.0 kHz, a flow velocity of 0.40 mm/sec, and a voltage of 10.0

Vpp. The detection limit was ~210 CFU/mL for a portable Raman system with a capture time of 50 seconds.

In the final study, a real-time impedance method was employed to detect *Vaccinia* virus (human virus) in the nano-DEP device at 1.0 kHz and 8.0 Vpp giving a detection limit of $2.51 \times 10^3$ pfu/mL.

# Table of Contents

# List of Figures

# List of Tables

# List of Abbreviations

| | |
|---|---|
| AC | Alternating Current |
| ACV | Alternating Current Voltammetry |
| CE | Counter Electrode |
| CM | Clausius Mossotti |
| CNF | Carbon Nanofiber |
| CNT | Carbon Nanotube |
| CV | Cyclic Voltammetry |
| CVD | Chemical Vapor Deposition |
| DC | Direct Current |
| DEP | Dielectrophoresis |
| DI | Deionized |
| DSNB | Dithiobisnitrobenzoic acid |
| DTSSP | 3,3´Dithiobis(sulfosuccinimidylpropionate) |
| DNA | Deoxyribonucleic acid |
| *E. coli* | *Escherichia coli* |
| EDC | 1-ethyl-3-(3-dimethylaminopropyl) carbodiimide hydrochloride |
| EIS | Electrochemical Impedance Spectroscopy |
| ELISA | Enzyme-linked Immunosorbent Assay |
| GNP | Gold Nanoparticle |
| ITO | Indium tin oxide |
| MES | 2-(N-morpholino)ethanesulfonic acid |

| | |
|---|---|
| MWCNF | Multi-walled Carbon Nanofiber |
| MBA | 4- MercaptoBenzoic Acid |
| NOVs | Nanoovals |
| NE | Nanoelectrode |
| NEA | Nanoelectrode Array |
| NHS | *N*-hydroxysuccinimide |
| NP | Nanoparticle |
| PBS | Phosphate Buffered Saline |
| PEG | Polyethylene Glycol |
| PCR | Polymerase Chain Reaction |
| PECVD | Plasma Enhanced Chemical Vapor Deposition |
| RE | Reference Electrode |
| RIE | Reactive Ion Etching |
| SEM | Scanning Electron Microscopy |
| SERS | Surface Enhanced Raman Scattering |
| TEM | Transmission Electron Microscopy |
| VACNF | Vertically Aligned Carbon Nanofiber |
| WE | Working Electrode |

# Acknowledgements

Finishing a Ph.D. in Chemistry is truly a marathon event, and it would not have been possible to complete this long journey without the help of countless people that were around me in last five years.

First, I would like to thank my Professor Jun Li for giving me the opportunity to be his student. His positive and motivating attitude towards research guided me all the way through this long journey. I express my gratitude to my supervisory committee Dr. Christopher Culbertson, Dr. Daniel Fung, Dr. Stefan Bossmann, and Dr. T.G Nagaraja. I would also like to thank Professor Christopher Culbertson for giving me the freedom to use equipment in his lab. I am thankful to Professor Daniel Fung for his time and valuable input in my dissertation. I am grateful to Professor T.G Nagaraja for serving as external committee chair and for conducting the final defense exam. Additionally, I am thankful to Dr. Lateef Syed for teaching me basics of lithography. Special thanks go to all former and present Li group members: Dr. Yifen Li, Steven Klankowski, Luxi Zhang Swisher, Yichen Zheng, and Yiqun Yang. Thank you, Luxi for helping out with nanoelectrode fabrication process and support as a friend.

The Department of Biology played an essential part throughout my Ph.D. journey. I am thankful to Dr. Dan Boyle for training me in SEM and TEM and for providing me valuable input during my research. Professor Stefan Rothenberg and Sherry Basset played an important role by providing *Vaccinia* viruses for my third publication. I am thankful to Professor Daniel Marcus from Department of Veterinary Medicine for letting me use lock-in amplifier for the impedance project. I would like to thank Dr. Omer Farooq for his time and advice. Thanks to Vinnay Shivana for introducing me to the field of virology. Special thanks to Dr. Gaind Pandey and Yiqun Yang for providing their valuable inputs about my research.

Additionally I am thankful to several people at the Department of Chemistry Department, especially, Tobe Eggers, Ron Jackson, Jim Hodgson, Leila Maurmann, Mary Dooley, and Kim Ross.

I would like to acknowledge funding from US Department of Homeland Security Scientific Leadership Award grant # 2012-ST-062-000055 and Kansas Bioscience Authority through the Center of Excellence for Emerging and Zoonotic Animal Diseases (CEEZAD) at Kansas State University. I would like to thank the Chemistry Department for their teaching assistance fellowship. It was wonderful to work with Earline Dikeman and Michael Hinton during my teaching duties. Thank you, Sonali Pandey, Jared Schroeder, Omer Farooq, Cathryn Davis, and Marijoo Hawkinson. Thank you all for the wonderful time we spent together.

Finally, a big thanks Rasik Karsadas Katira, my parents, and family members especially my sister Kinjal Madiyar and brother-in-law Shuhanko Basu for their help. My research would not have been possible without the help and support of all the people aforementioned. Thank you all for your love and support!

# Dedication

“Mr. Rasik K. Katira, my parents and loved ones.”

# Preface

The dissertation comprises of the following major sections:

**Chapter 1** – The chapter includes the introduction to biohazards due to pathogens and the traditional and new methods employed for detection. It gives a brief introduction to biosensors, and two transducing mechanisms are discussed, namely, optical and electrochemical. Further, it discusses the concept of nanotechnology; advantages of using vertically aligned carbon nanofiber (VACNF) nanoelectrode array (NEA) and nanoparticles (NP) along with literature review on their applications.

**Chapter 2** – The chapter is a discussion of the principle of dielectrophoresis (DEP) and electric field acting on the bioparticles and the interaction of electric field on bacteria and viruses. It elaborates on the simulation of Clausius Mossotti factor and various forces acting on the particle under fluid flow and the literature review of applications of DEP.

**Chapter 3** – The chapter discusses the fabrication of the VACNF and assembly of the nano-DEP device. It includes the fabrication, characterization and applications of VACNF in pathogen detection. It elaborately discusses the setup under a fluorescence microscope and a confocal Raman microscope.

**Chapter 4** – An accepted paper, and highlighted as a cover image in *Electrophoresis (Special Issue of Dielectrophoresis, 2013)*. This study is about using NEA for electronic manipulation of *Bacteriophage* T4r. A new phenomenon of *Lichtenberg Figures* has been discovered with viral particles on VACNF NEA and comparison of capture profiles of bacteria and viruses on VACNF.

**Chapter 5** – An accepted paper, published in *Nanoscale*. This paper describes the integration of nano-DEP device with surface enhanced Raman scattering (SERS) for detection of *Escherichia*

.*coli.* This chapter summarizes the importance of SERS in detecting pathogens using direct detection scheme. The nanoovals attached to QSY21 (Raman Tag) is attached with *E.coli*. The detection limit found with the portable DEP-SERS technique was about 210 bacteria /mL.

**Chapter 6** – The chapter focuses on pathogen detection using impedance technique. We have used *Vaccinia* virus as a prototype for human viruses. This work explores the real-time impedance measurement of *Vaccinia* virus in a 'point-and-lid' dielectrophoretic setup for sensitive impedimetric detection of viruses.

Finally, **Chapter 7** summarizes the main conclusions of this work and explains the future directions. Appendix includes the supporting information for the discussed sections of the journal publications and preliminary results obtained during the course of study.

# Chapter 1 - Introduction

## 1.1 Importance of Rapid Pathogen Detection

Waterborne, foodborne, airborne pathogens can be divided into three broad categories: viruses, bacteria, and parasites, the latter of which are comprised of protozoa and helminths.[1] These pathogens are transported through the environment, often in low concentrations.[2, 3] However, while these low levels prove challenging for detection, they still may present a considerable public health risk.[4] According to the Center for Disease Control and Prevention (CDC) surveillance reports in 2013, 818 foodborne disease outbreaks were reported, resulting in 13,360 illnesses, 1,062 hospitalizations, 16 deaths, and 14 food recalls from pathogens such as *Escherichia coli*, *Salmonella*, *Listeria*, and noroviruses.[5,6] The USDA food safety department has recalled several millions of dollars worth of meat, poultry, vegetables and other agricultural products because of the presence of harmful bacteria.[7,*] Despite the strict regulations governing consumables, food and water contamination outbreaks continue to increase and pose a serious risk for health management. Clearly, it is essential to monitor the foodborne pathogens throughout the food processing system from production, through distribution to the point-of - sale.[7] A concentration as low as 10 to 100 colony forming units per milliliter (CFU/mL) of four major foodborne pathogens (*E. coli* O157:H7*, Listeria monocytogenes, Salmonella, Campylobacter jejuni*) can result in illness if consumed.[8, 9] This concentration is beyond the detection limit of most assays, so more sensitive tests with better detection limits need to be developed.[10]

[*] The complete details of the recent (2015) recalled products can be viewed at http://www.foodsafety.gov/recalls/recent

## 1.2 Traditional Detection Techniques: Merits and Limitations

The traditional method of culturing and colony-counting remains the '*gold standard*' for detection of pathogens. This method is laborious and time-consuming. The detection of *E. coli* typically takes 24 hours and it may take up to 7 days for detecting *L. monocytogenes*. The long detection time poses the difficulty for quality control and quality assurance in testing of perishable foods.[11] These procedures also tend to underestimate the actual number of bacteria.

Immunology-based methods that involve antigen-antibody reaction (using polyclonal, monoclonal or recombinant antibodies) have been useful to detect foodborne pathogens such as *E. coli, Salmonella, L. monocytogenes, and Campylobacter species*. Examples of standard immunological assays are enzyme linked immunosorbent assays (ELISA),[12] enzyme linked fluorescent assay (ELFA)[13] and bioluminescent enzyme immunoassays (BEIA).[14] In the overall detection scheme, there are two significant deficiencies: one is the specificity of the antibody, and the second the inability to track the pathogens in real-time (minutes). A variation in the above methods can be accomplished by a combination of immunological methods coupled with nanoparticles and magnetic beads. One of the most sensitive methods in biology for pathogen detection is the polymerase chain reaction (PCR)[15-17] that can amplify specific segments of DNA and is used to detect and identify bacterial genes responsible for causing diseases.[18] The advantages of PCR is that it can selectively detect small number of target nucleic acid sequences in the sample[19] such as target cell lysates.[20] It is vital to include appropriate controls for the application of this method. Protocols have been well established for the detection *of S. aureus, L. monocytogenes, Bacillus cereus, C. jejuni* using PCR. Alternatives for this technique such as real-time PCR has been developed[21], but despite all the advantages for detection of microbes, it

is very expensive, complicated and requires skilled workers to carry out the tests. In addition, it is not suitable for rapid field applications.[22]

Since all the traditional methods to detect food and water-borne pathogens fall short of the goal, there is a need for simple, rapid, reliable, specific and sensitive technology. Additionally, it is important to make the system cheap, portable and integrated with real-time analysis. In this dissertation, the research is aimed at successfully integrating nanoelectrode arrays in microfluidic devices for separation of bioparticles from the solution using a physical phenomenon called dielectrophoresis. Miniaturized biosensor based on nanoelectrode array is then used for identification of pathogens in solution.

The current chapter focuses on the concepts of biosensors and the potential of nanomaterials with three primary targets for transducers: fluorescence, Raman, and impedance measurement. This will lead us to the introduction of nanoelectrode array (NEA) and nanoparticle (NP) based biosensing strategies.

## 1.3 Principles and Significance of Biosensors

The biosensor is an analytical device that incorporates the biological recognition element that responds to the target (a chemical or biological)which gives a change in signal that is converted into a readable format by the transducer.

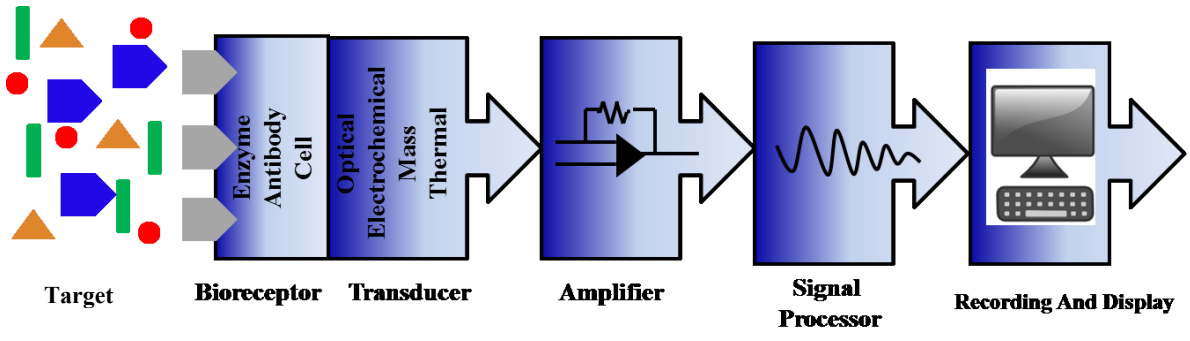

**Figure 1.1: Schematic diagram of biosensor with its components**

The biosensor is made up of five elements shown in Figure 1.1 namely: bioreceptor, transducer, amplifier, signal processor and recording and display devices.[22] Among these components, researchers are interested in the recognition element and the transducer optimization to detect pathogens.

Biorecognition elements such as antibody/antigen[23], enzymes, nucleic acids,[24] and bacteriophages interact specifically with particular target molecules.[25] Multiplex detection can be done by employing different recognition elements on the biosensors. Following the biorecognition step, various transducers are used to convert the physicochemical interactions between the probe and the analyte into measurable signals in optical, electrical, or magnetic domains, which provide the information of the quantity of the captured molecules that links to the original analyte concentration in the sample.[26] Among the various metrics used to compare different biosensors, selectivity and limit of detection (LOD) are the most important. LOD defines the lowest detectable analyte concentration that is significantly different from the blank solution. The minium detectable signal

$$y_{dl} = y_{blank} + 3s \quad \text{.....(1.1)}$$

where, $y_{bkank}$ is signal from the blank solution and $s$ is the standerd deviation. To detemine the detection limit, the slope of the calibration curve ($m$) is taken into consideration and given by,

$$Detection\ Limit = \frac{3s}{m} \quad \text{.....(1.2)}$$

Selectivity gives a measure of the ability of the system to detect the analyte in the presence of other interfering molecules.[27] Herein, we focus on fluorescence and surface plasmon

enabled spectroscopies as optical transducers and impedance technique as an electrochemical transducer.

Optical detection method frequently requires labeling the analyte with a molecule that has specific optical signal. For example, fluorescent dye molecules can be intercalated into double stranded nucleic acids or chemically attached to analyte molecules.[28] The label is excited by the incident light and returns to its minimum energy state by emitting light at a different wavelength. This method is preferred for pathogen detection applications because it provides low detection limits, is insensitive to electromagnetic noise and provides multiplexing potential.[29, 30]

Spectroscopic techniques such as infrared spectroscopy,[31-33] Raman spectroscopy,[34-37] and surface enhanced Raman spectroscopy[38] are utilized for pathogen detection. These methods are frequently reported as fingerprint methods and non-destructive techniques. Fourier transform infrared spectroscopy (FTIR) was developed by C. Yu et al.[39] (2004) and M. Lin et al.[40] (2005) to differentiate eight microorganisms in apple juice and quantitate of their detection limits. The strong absorption by water in the biological samples poses a difficulty in FTIR. Therefore Raman spectroscopy is generally preferred because there is no interference from water.

Raman spectroscopy (RS) is a vibrational spectroscopic method that provides highly specific information about material properties. It can be applied to label-free analyte detection revealing molecular fingerprints.[41, 42] The light scattering from the low-concentration suspensions of bacteria such as *Erwinia carotovora pv. carotovora* (ECC) and *Clavibacter michiganense* (CBM) were detected with a 785 nm laser by Z. Schmilovitch et al. (2005).[43] However, conventional Raman Spectroscopy characterization of microorganisms has poor LOD's because only one in a million photons is inelastically scattered to give a Raman signal. Moreover, the intrinsic Raman signals from microorganisms are very weak.[37, 44] A similar

detection technique to fingerprint identification is surface enhanced Raman spectroscopy (SERS), where target molecules are kept in the vicinity of the nano-sized metal particles and Raman signal from the molecules are enhanced. Several studies of pathogen detection in dry, as well as in moist environments were carried out with this fingerprinting technique. More about this technique will be discussed in Chapter 5 (page 72).

Electrochemical detection transducers which are used in pathogen detection rely on measuring the change in electrical properties (current or potential) of the pathogen particles when attached to/or associated with electrodes.[45] The traditional impedance technique usually includes an antigen-antibody complex and application of a small voltage of 5.0 to 10.0 mV, through the biosensors depending on the process.[46] A label-free impedance technique utilizes a redox molecule in conjunction with target molecules to measure the change. Advantages of impedimetric methods include the capability to monitor large numbers of samples simultaneously in a relatively short detection span. Despite the development of impedance techniques, more efforts are required to make a portable reagentless system that allows rapid detection of foodborne pathogens.[46-49]

## 1.4 Nanomaterials for Pathogen Detection: Advantages and Disadvantages

To detect concentrations of pathogens typically found in treated and untreated drinking water, the biosensor must be selective to recognize the pathogens. The nanomaterials for pathogen detection can be advantageous in following ways;

(1) They have a large surface area that can be modified with functional groups to aid in binding of biomolecules (such as proteins, antibodies, epitope and nucleic acids). This an serve as a

platform by allowing interaction with target molecules (bacteria and viruses) with high probability.

(2) They possess high electronic and optical properties that can enhance limit of detection of a target in a complicated background matrix. All these reasons can eventually help the integration of nanomaterials with biomolecules.[50-52]

The signal transduction mechanisms typically direct the choice of the nanomaterials in a biosensor. Herein, I will focus on nanoparticles and carbon nanomaterials, mainly vertically aligned carbon nanofibers (VACNFs), elaborated in Chapter 3 (page 39).

### *1.4.1 Nanoparticles for Pathogen Detection based on SERS*

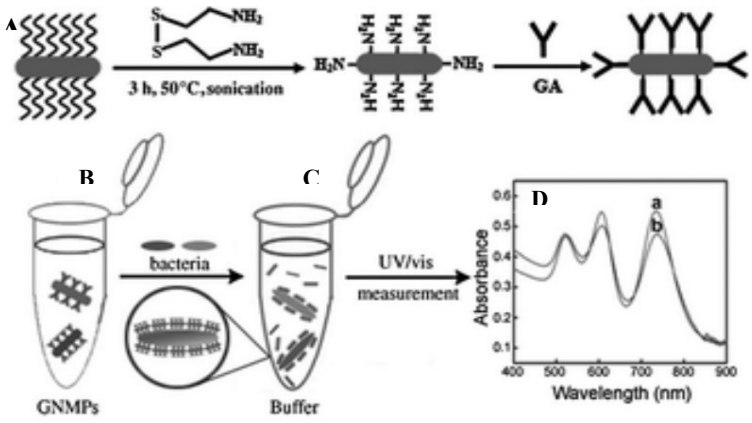


**Figure 1.2: Schematic representation of the bioconjugation of the nanoparticles with amine groups.**

**This modification is useful for attaching antibodies to nanoparticles and bacteria, which is observed by the change in the absorption peak. (Reprinted with permission from C. Wang, J. Irudayaraj, *Small* 2008, 4, 2204-2208.)**

In the case of noble metals, when the particle size is reduced to the nanometer scale, which is comparable to the wavelength of light the collective oscillation of the electrons in the particle generates a strong absorption at a specific wavelength known as the localised surface

plasmon resonance (LSPR).[53] This generates a high electric field at the surface which leads to surface enhanced Raman scattering (SERS).

SERS obtained with gold nanoparticles of different sizes and shapes (such as gold nanorods[54] core–shell gold nanoparticles[55], popcorn shaped gold nanoparticles[56] and star shaped nanoparticles[57]) are employed for pathogen detection. The size and shaped of the nanoparticles can be tuned according to the wavelength for highest surface plasmon frequency to increase the local resonance electromagnetic field over several orders of magnitude.

SERS was discovered in 1974 as Fleischman et al.[58, 59] observed a large signal enhancement by measuring pyridine adsorbed on electrochemically roughened silver. The phenomenon of SERS is explained by a combination of an electromagnetic and a chemical mechanism related to charge transfer between the substrate and the analyte molecules. SERS enables enhancement of weak Raman scattering signals by $10^8$–$10^{14}$ fold to obtain a fingerprint spectra of different analytes down to the single molecule level.[60] The amplification of the electromagnetic field is highest at places called "hot spots."[61]

The vibrational bands obtained by SERS are much narrower due to the enormous surface plasmon resonance. The absorption cross-section of gold nanoparticles is 5–7 orders of magnitude higher than that of ordinary dye molecules. Additionally, there has been tremendous progress in characterizing and identifying unique fingerprints for ultrasensitive pathogen sensing. As a result, one can consider each metal nanoparticle as an optical probe equivalent to several million dye molecules, which will help to increase the detection limits tremendously.[62]

In Figure 1.2 C. Wang and J. Irudayaraj (2008)[54] reported amine-modified gold nanorods with different aspect ratios, for simultaneous detection of *E. coli* and *S. typhimurium*, at concentrations less than $10^4$ CFU/mL. The gold nanorods surface is modified with cysteine

hydrochloride and antibodies specific to pathogens. The modification to the surface of nanorods, changes the longitudinal plasmon (LP) band absorption (~750 nm), which is measured by UV-visible spectroscopy. The procedure is illustrated in Figure 1.2A. The peak maximum ($\lambda_{max}$) in UV-vis is noted when the nanoparticle is attached to antibodies and bacteria (Figure 1.2D). Their reported method is simple and useful for multiple detections of pathogens in less than 30 min based on changes in LSPR bands.[63]

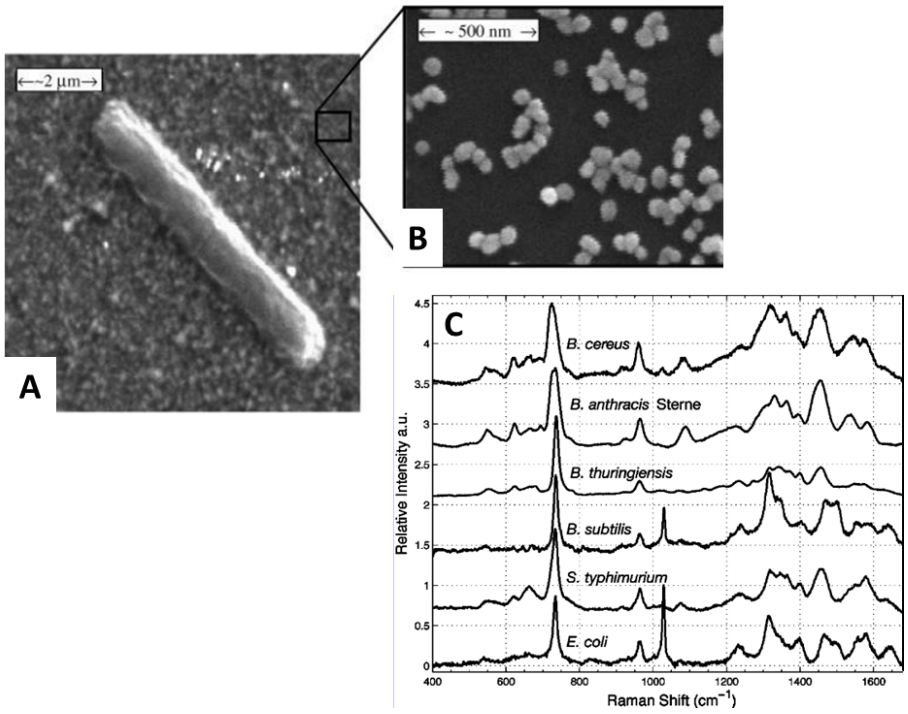


**Figure 1.3: Fingerprint identification of different bacterial species.**

**(A) Scanning electron microscope image of one bacterium on the metal nanoparticle surface. (B) TEM of gold metal nanoparticles (C) Fingerprint Raman spectrum of the different bacterial species (Reprinted with permission from W. R. Premasiri, D. T. Moir, M. S. Klempner, N. Krieger, G. Jones, L. D. Ziegler, *J. Phys. Chem. B,* 2005, *109*, 312-320.)**

W. R. Premasiri et al.[64] (2005) reported a simple yet beneficial method of detecting microorganisms on gold nanoparticle aggregate-covered glass chips through Raman spectra analysis. They observed that enhancement of intensity factors could be greater than $10^4$ per bacterium. As shown in their results, in Figure 1.3, the relative intensity of a band at 1050 $cm^{-1}$ and the relative intensity pattern in the 1200–1700 $cm^{-1}$ region are essential to discriminate between closely related bacteria species using SERS spectra. However, the drawback of this design is the complex principle component analysis and other statistical methods used to carry out the data analysis. Moreover, Jarvis et al.(2003)[65] explained that the Raman spectra between the same species can be different depending on the position of the nanomaterial attached to the bacteria and the environmental conditions used for the experiment.

The important step in using the nanoparticles in biosensors for pathogen detection is bioconjugation of the nanomaterials of different sizes and shapes to microorganisms and compatibility of nanomaterial to pathogens. To assign selectivity to these nanomaterials, they are modified with various recognition elements such as an antibody to aid the attachment of nanoparticles to bacteria. This idea was utilized in attaching *E.coli* to nanoovals by making them biocompatible with polyethylene glycol (PEGs) and selective by attaching antibody to pathogen. The procedure will be discussed in Chapter 6 (page 77).

### *1.4.2 Nano-DEP*

Dielectrophoresis (DEP) has been used extensively to position, concentrate, sort and transport of polarizable particles such as bacteria, viruses, mammalian cells, etc. The cell positioning is used either to create long-term (more than several hours) patterns of cells on a substrate or for short-term (minutes) observation of cells in a particular location.

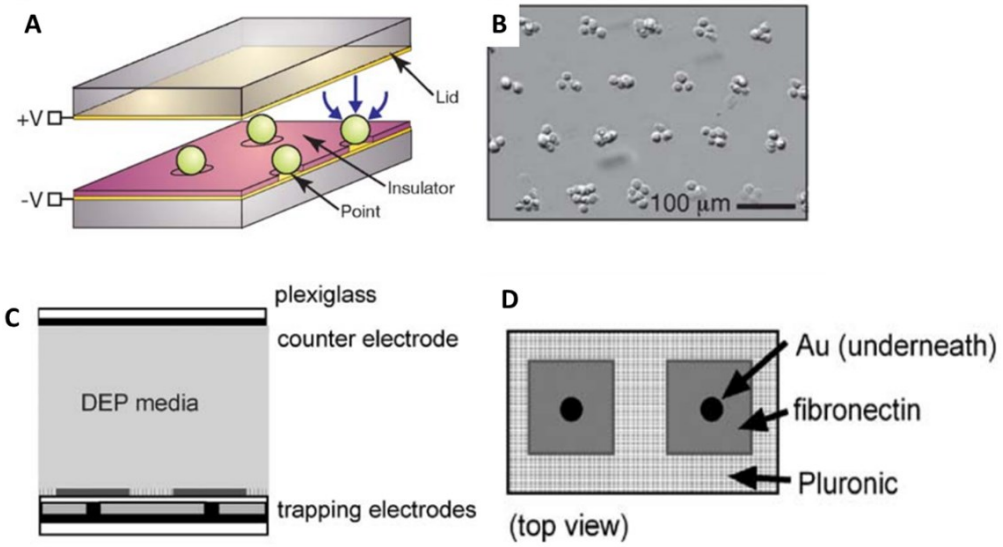


**Figure 1.4: Point-and-lid geometries used in dielectrophoresis.**

**(A) The voltage is applied to the circular gold electrode (point electrode), and indium tin oxide coated glass (lid electrode). (B) The cells are positioned on the gold electrode at specific distances. (C) The gold electrode embedded in a polymer (point electrode) and plexiglass coated with gold (lid electrode). (D) The top of the design where electrodes are covered in biocompatible reagents like fibronectin. (Reprinted with permission D. S. Gray, J. L. Tan, J. Voldman, C. S. Chen, *Biosens. Bioelectron.*, 2004, 19, 1765-1774).**

Different geometric configurations such as interdigitated electrodes (IDE),[66] quadrupole electrode,[67, 68] octupole electrode,[69, 70] ring-dot electrodes,[71] point-and-lid geometry[72] and nDEP microwells[73] are used in dielectrophoresis for various purposes. We will focus our attention on 'point-and-lid geometry' to study particle-to-particle interactions (shown in Figure 1.4). Voldman et al.[71, 72, 74] have fabricated micrometer sized point-and-lid geometry for manipulating and positioning cells. To incorporate this idea, vertically aligned carbon nanofibers (VACNFs) are used in current studies. The miniaturization of the electrode provides a highly focused

electrical field that act as potential trap for small bioparticles against large hydrodynamic forces, eventually leading to a dense concentration of particles.[72]

This technology promises new capabilities to perform novel experiments for sorting and concentrating bioparticles at the nanoscale. We anticipate that the bottom-up approach of such nano-DEP devices will allow the integration of millions of nanoelectrodes in lab-on-a-chip devices and will be useful for manipulating submicron particles.

Integration of DEP devices in the microfluidic channel along with Raman measurements were carried out by K. Kalantarzadeh, et al. (2011) (Figure 1.5A).[75] They employed curved microelectrodes (Figure 1.5C) patterned on a quartz substrate and integrated with a microfluidic channel imprinted in polydimethylsiloxane (PDMS). They investigated tungsten trioxide ($WO_3$) and polystyrene nanoparticles suspended in water with surfactants for the direct mapping of their spatial concentrations in the device (Figure 1.5B).

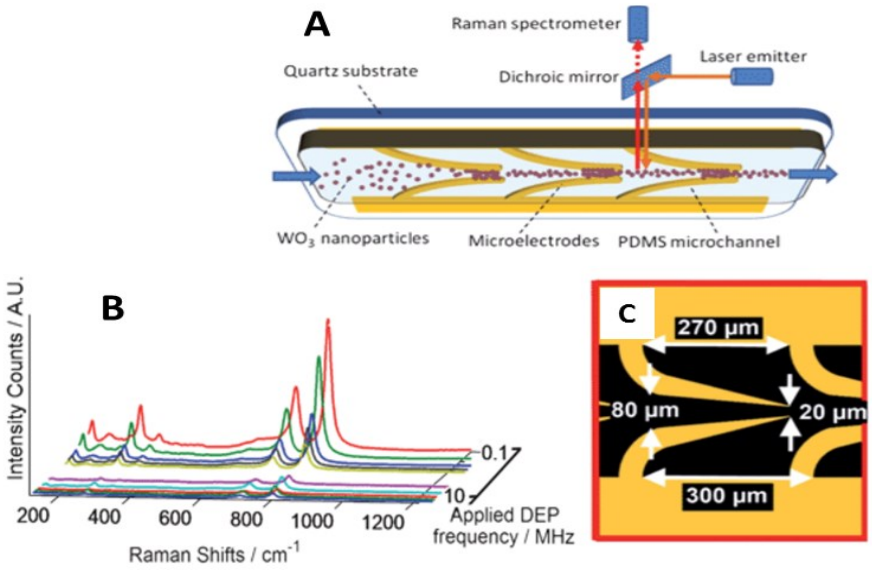


**Figure 1.5: Integration of Raman detection with microfluidics**

**(A) Schematic of DEP-Raman system layout. (B) The plot of $WO_3$ nanoparticle Raman spectra at different DEP frequencies, decreasing in frequency along the z-axis. (C) Curved**

**DEP electrode design and layout. (Reprinted with permission from K. Khoshmanesh, S. Nahavandi, S. Baratchi, A. Mitchell, K. Kalantar-zadeh, *Biosens. Bioelectron.*, 2011, 26 (5), 1800-1814)**

F. L. Yang et al. (2013)[76] reported an interesting study of integrating DEP and Raman measurement. In this experiment (Figure 1.6), the separation of the red blood cells and bacteria took place on a chip with interdigitated circular electrodes. This device uses a hybrid electrokinetic mechanism, where the bacteria can be effectively gathered at the stagnation area (center) due to positive DEP on the SERS-active roughened electrode at a frequency of 800 Hz. While at the same frequency, blood cells experienced negative DEP and were excluded away from the center. More details on DEP are discussed in Chapter 2 (page 23).

This reports both fast pDEP and nDEP mechanisms with the detection limit $5 \times 10^3$ CFU /mL in 3 min. and identification of the bacteria occurs by the fingerprint method as described previously. These studies show promise for integrating the nano-DEP device with Raman and SERS measurement to detect bacteria and viruses.

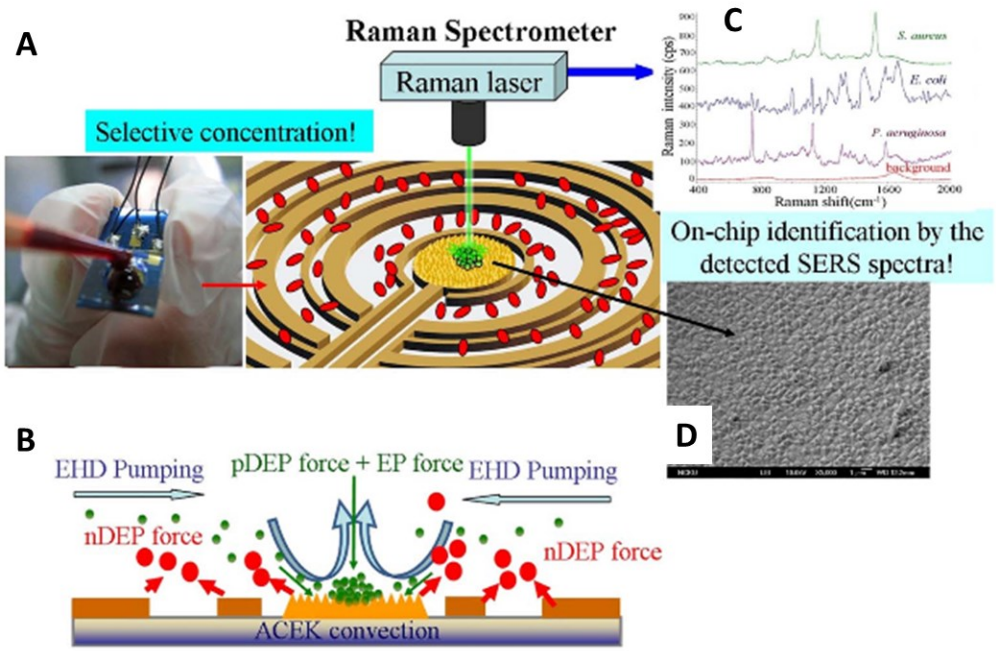


**Figure 1.6: Separation and identification of pathogens using dielectrophoresis with Raman scattering.**

**(A) Experimental setup of the DEP-Raman chip. (B) The schematic figure showing the operation of the chip. An alternating current (AC) electric field induced dielectrophoresis to concentrate bacteria rapidly on the gold surface with the aid of electrohydrodynamic drag (EHD) force and positive DEP (pDEP) force. SERS fingerprint of the concentrated bacteria is obtained when an optimum laser source is directed on the gold surface. (C) Illustration of the fingerprint spectrum from bacteria (D) Scanning electron microscope image shows the roughened gold surface at the center electrode. (Reprinted by permission from I. Fang Cheng, H-C. Chang, T-Y. Chen, C. Hu and F.-L. Yang, *Sci. Rep.*, 2013, 3.)**

### *1.4.3 Raman Microscopy in Microfluidics*

The integration of Raman spectroscopy with microfluidics manifests challenges (described below) in small volume detection, yet it is essential in optimizing the spectral collection efficiency. Herein I will discuss the main four parameters critical to obtain a reliable Raman spectrum.[77]

1. **Focal length:** A microfluidic device is either made of PDMS, glass or quartz surfaces that are several millimeters thick. The focal length must be long enough to penetrate into the fluid sample. The objective determines the focal length. Lower magnification lenses will have longer focal distances, but the area of view will be larger. Therefore, the Raman intensity per unit area will be diminished. For higher objective lenses, a long distance objective will be beneficial as it will provide high Raman intensity per unit area.
2. **Detection volume:** The depth of focus (also known as the confocal parameter) is estimated as twice the Rayleigh range. In order to achieve a small depth of focus, the microscope must be operated in confocal mode, where the size of the spectrometer entrance slit is reduced to the smallest value compatible with the required signal output.
3. **Excitation wavelength:** The intensity of Raman scattering is inversely proportional to the fourth power of the wavelength, so it is preferable to use shorter excitation wavelengths. However, these produce significant interference and shot noise from the fluorescence signal. A 785 nm laser is beneficial because of its low absorption from biological elements and reduced noise.
4. **Optical power:** High power at a small confocal spot will cause significant damage to the thermally liable biological samples. In addition to this, heat can cause turbulence or random

movement in the small sample solution. To avoid any artifacts in the detection and signal recording it is necessary to use an optimum power so that the sample is not damaged.[77]

### *1.4.4 Effective Impedance Measurement using Nanomaterials*

Electrical biosensors are based on the measurements of change in currents and/or voltages to detect binding on the electrodes. They are divided on the basis of electrical measurements either by voltammetric, amperometric, or impedance sensors.[46] We will focus our attention on impedance measurement. The impedance measurement consists of the application of a small amplitude alternating current (AC) signal superimposed on a constant direct current (DC) bias to the electrode. The resulting impedance of the system then provides information related to interfacial and bulk phenomena.[47]

Impedance biosensors are employed in the measurement because of their low cost, miniaturization, speed of analysis, freedom from unnessesary labeling, point-of-care diagnosis, and to not be influenced by the background color and surrounding lights compared to optical methods.[46] These sensors have been used for bio-warfare agent detection, consumer test kits, bioprocesses monitoring, and water quality testing. One crucial question that arises while considering impedance biosensors is whether they have sufficient selectivity for use in real world applications because actual samples may contain uncontrolled but significant amounts of non-target molecules.[46]

The electrochemical cell is a complex system and represented as an equivalent circuit for modeling the components of the electrode-electrolyte interface. The conventional model called a Randles circuit is comprised of the resistance of the electrolyte ($R_s$) in series with the capacitance of the dielectric layer ($C_{dl}$), the charge transfer resistance ($R_{CT}$) and the Warburg impedance ($Z_w$) as shown in Figure 1.7A

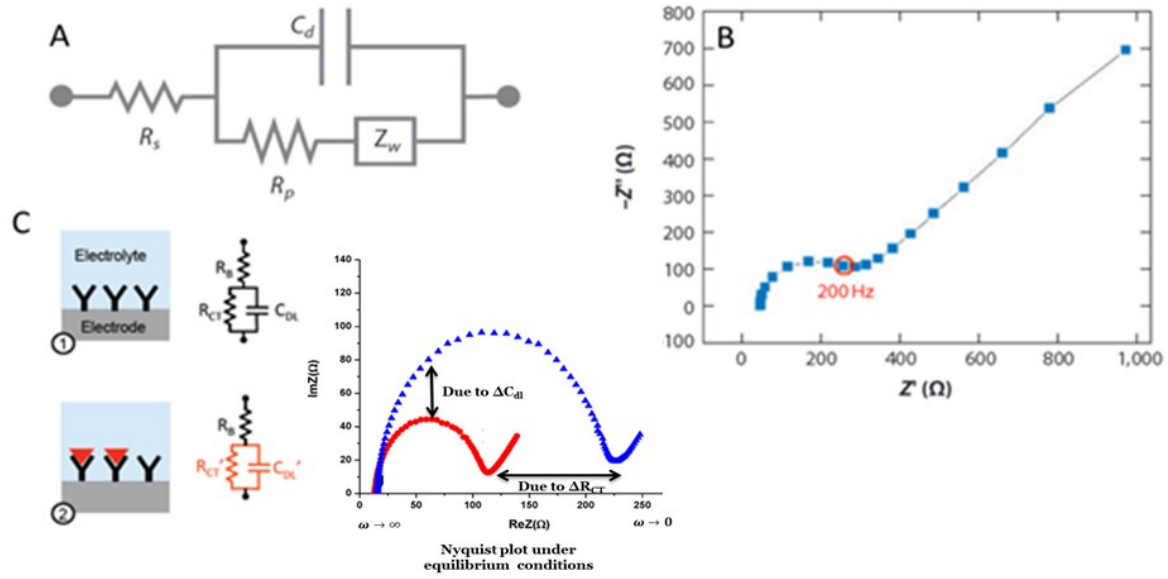


**Figure 1.7: Conventional Randle circuit and principle of impedance biosensor**

**(A) The Randle equivalent circuit, (B) The typical Nyquist diagram for the AC impedance measurements. (C) $R_{CT}$ changes significantly with multiple levels of antibody attachment. (Reprinted by permission from A. Manickam, The University of Texas at Austin 2012.)**

Figure 1.7B shows a typical Nyquist plot. The plot consists of two parts: a linear portion observed at the low-frequency range implying a mass-transfer limited process and a semicircle portion observed at the high-frequency range indicating a charge-transfer limited process. From the Nyquist plot, the values of $R_s$ and $R_{ct}$ can be easily determined. The semicircle diameter equals to electron transfer resistance $R_{CT}$. Impedance due to the diffusion of ions to the interface from the bulk of the electrolyte is often referred to as Warburg impedance, $Z_w$. The intercept of the semicircle with the $Z_{re}$ axis at high frequencies is equal to the solution resistance, $R_s$. Extrapolation of the circle to the lower frequencies yields an intercept corresponding to ($R_s$ + $R_{CT}$). The charge-transfer resistance $R_{CT}$ and the double layer capacitance $C_{dl}$ are the most

important electrical parameters in analyzing the impedance signal change for detection of bacteria.[78]

Impedance biosensors operate by two mechanisms that will be studied in detail in Chapter 6 (page 103). Firstly, impedance biosensors focus on the biorecognition element in the biosensor flow chart.[79] An increase in the interfacial impedance is observed when biorecognition elements and target attach to the electrode, effectively reducing both the electrode area and the current reaching the electrode, leading to an increase in $C_{dl}$ as shown in Figure 1.7C[80-85]

Secondly, in addition to using a bio-recognition element, the redox couple $[Fe(SCN)_6]^{3-/4-}$ is commonly used in impedance biosensors as shown in Figure 1.8A. L. Yang and Y. Li et al (2004)[85] have demonstrated an immunosensor for detection of *E. coli* O157:H7 cells using faradaic impedance spectroscopy with an IDA microelectrode. Upon attachment of the bacterial cells to the electrode, the interfacial increase in the electron-transfer resistance is observed due to the antibody immobilization and binding of *E. coli* cells. The reaction rate is decreased because the charge transfer from the redox couple $[Fe(SCN)6]^{3-/4}$ is hindered due to the presence of antibody and bacteria (Figure1.8 A, panel 3). It is reported that the membranes of natural biological cells (thickness −10 nm) show a capacitance of 0.5−1.3 μF/cm$^2$ and a resistance of 102−105 Ω·cm$^2$.[86] The Nyquist plot ($Z_{im}$ vs. $Z_{re}$) is the best way to visualize and determine the charge transfer resistance change shown in Figure 1.8B.[85, 87-89]

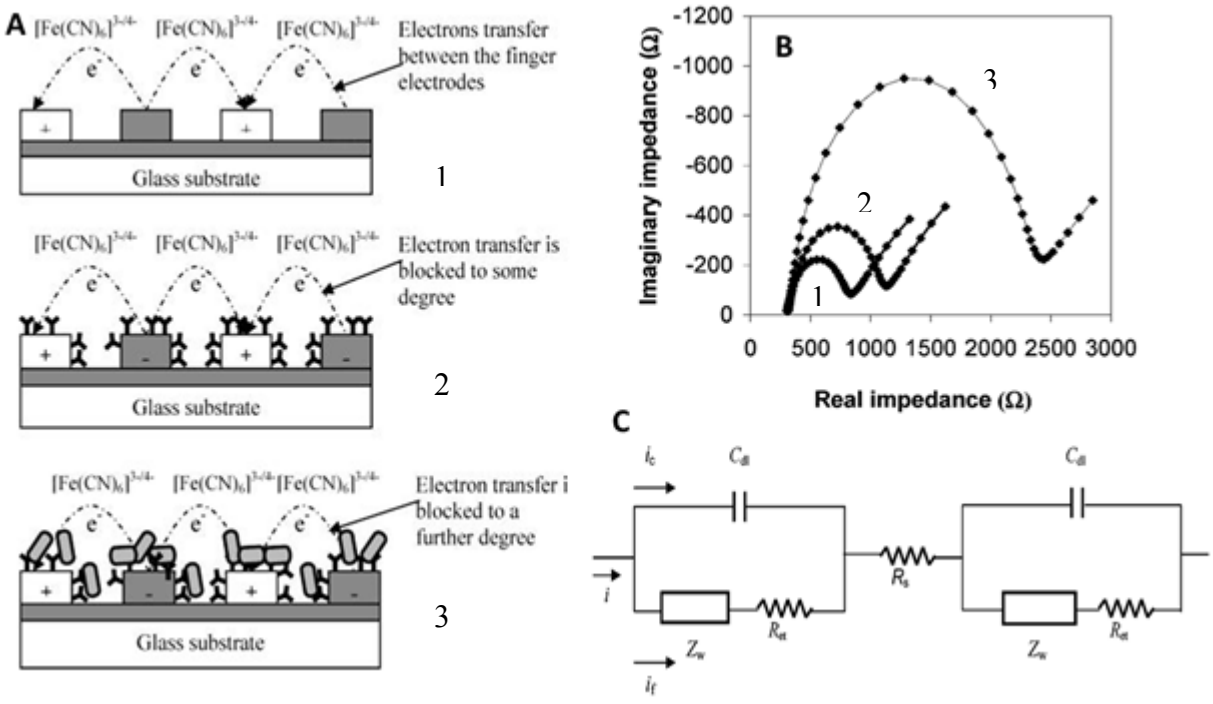


**Figure 1.8: Principle of the impedance immunosensor**

**(A) Constructed by interdigitated array microelectrode: (1) bare electrode; (2) with antibody immobilization; (3) with cell binding. Gray oval, *E. coli* O157:H7 cell;** Y**, anti-*E. coli* antibody. (B) Nyquist diagram of electrochemical impedance spectra of the bare interdigitated ITO electrode were electrons freely transfer between electrodes (1), after antibody immobilization causing some blocking to electrone transfer (2), and after *E. coli* cells binding causing further blocking to electrone transfer (3) in the frequency range from 1 Hz to 100 kHz. Data points from left to right correspond to decreasing frequency. Amplitude voltage, 5 mV; electrolyte, 10 mM $[Fe(CN)_6]^{3-/4-}$ (1:1) in 0.01 M PBS, pH7.4; *E. coli* O157:H7, 2.6 × $10^7$cells. (C) Equivalent circuit of electrochemical impedance measurement system with the interdigitated array microelectrode (Reprint with permission from L. Yang, et al., *Anal. Chem.* 2004, 76 (4), 1107-1113.)**

Figure 1.8C, illustrates the electronic equivalent model. The parameters are same as described above. Each branch circuit represents the behavior of each set of array electrodes and the total current through the electrode surface is the sum of faradaic current ($i_f$) and double layer current ($i_c$), in the branch circuit, the warburg impedance is considered to be in series with the electron-transfer resistance and both of them are connected in parallel with the double layer capacitance.

The researchers have utilized either $C_{dl}$ or $R_{CT}$ to measure the impedance from pathogens, such as bacteria and yeasts, which were mentioned earlier. Interdigitated array microelectrodes (IDAM) have been primarily used in the previously reported impedance studies. An ITO IDAM chip coated with anti-*E. coli* antibodies that captured *E. coli* O157: H7 cells had a detection range of $4.36 \times 10^5$ to $4.36 \times 10^8$ CFU/mL as reported by L. Yang et al. (2004)[85] E. C. Alocilja et al.(2004)[90] reported the detection of $10^5$ to $10^4$ CFU/mL with an open gold IDAM chip immobilized with antibodies by salinizing the sensor surface using 3-mercaptomethyldimethylethoxysilane and a hetero-bifunctional cross-linker, N-(g-Maleimidobutyryloxy) succinimide ester. M. Varshney and Y. Li (2009)[81] developed a label-free impedance biosensor based on gold IDAM for the detection of *E. coli* O157: H7 in food samples. Cells were separated and concentrated with the help of magnetic nanoparticle-antibody conjugates. The impedance sensor detected a minimum of $7.4 \times 10^4$ and $8.0 \times 10^5$ CFU/mL of *E. coli* O157: H7 in pure culture and ground beef samples respectively. The same group tried a flow cell to detect bacterial cells in a detection volume of 60 nanoliter and were able to detect as little as $1.6 \times 10^2$ and $1.2 \times 10^3$ cells of *E. coli* O157: H7 cells present in pure culture and ground beef samples.[91]

### *1.4.4.1 Integration of DEP with Impedance and Pearl Chaining*

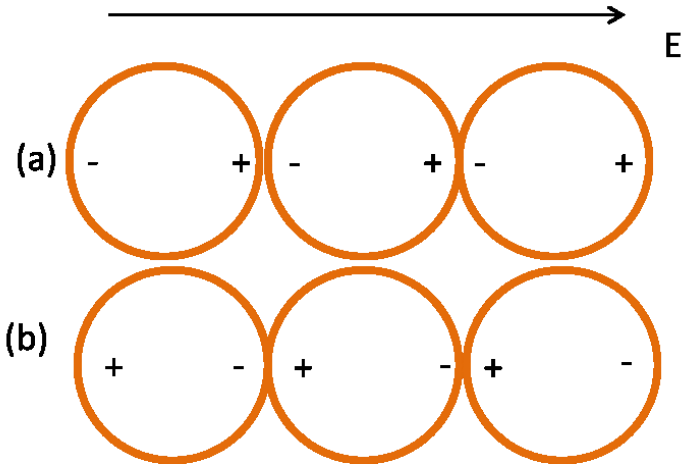


**Figure 1.9: Explanation of formation of pearl chains.**

**The formation of particle chains occurs independently of whether the particles are experiencing (A) positive or (B) negative dielectrophoresis; in both cases, the dipoles align in the same direction to each other.**

The combination of impedance with dielectrophoresis is referred to as dielectrophoretic impedance measurement (DEPIM). Using IDAM for biosensors probe, there are two mechanisms that can be followed. First, is the direct capture of the pathogen on the electrode which was reported by R. Gomez-Sjöberg et al. (2005)[92] combined dielectrophoresis (DEP) with impedance microbiology for the design of an on-site incubation microfluidic biochip device embedded with platinum IDAM for the detection of *Listeria*. DEP was successfully used for the concentration of bacterial cells by a factor of $10^4$ to $10^5$, in a detection chamber of 400 picoliter. This method causes the formation of 'pearl chain' between the electrodes followed by an impedance measurement.

The pearl chaining is referred to as mutual dielectrophoresis, in which a chain formed by dipole-dipole attraction due to the polarization of the particles in a high magnitude of the electric field. The interaction force between two similar particles is based on their polarizabilities (Figure 1.9). This phenomenon was reported by J. Suehiro et al.[93] using IDAM to detect *E.coli* cells . The detection limit reported was $10^5$ CFU/mL in 10 min. This phenomenon is observed in the current study at high flow rate with virus particles and is discussed in section 4.3.6 (page 63).

The second way DEP can be used for pathogen detection is by adding specificity to the system by immobilizing bio-recognizing elements on IDAM surface. DEP acts as a driving force to attach bacteria to the electrode. This method was reported by Suehiro et al.(1999)[94, 95] L.Yang et al. (2006)[96] developed an IDAM based multifunctional microfluidic system for the concentration and accurate capture of *L. monocytogenes* by employing DEP and immobilizing anti-*Listeria* antibodies.

The present work is the integration of nanomaterials into a microfluidic device for pathogen detections using fluorescence, surface enhanced Raman spectroscopy and impedance measurements that were described above.

# Chapter 2 - Principle of Dielectrophoresis

## 2.1 Electrostatic Interaction with Particles

In order to understand the interactions between particles on the nanometer scale, it is worthwhile to examine the underlying processes. The Coulomb's Law[93] states that oppositely charged particles attract and like charged particles repel each other. The magnitude of this force is proportional to the product of the magnitudes of the two charges and is inversely proportional to the square of the distance between them. The direction of the force is along the line joining the two charges (as illustrated in Figure 2.1).

$$\vec{F} = \frac{Q_1 Q_2}{4\pi\varepsilon_0 d^2}\hat{r} \quad \text{..... (2.1)}$$

$Q_1$ and $Q_2$ are the two charges, $d$ is the distance between them, $\hat{r}$ is the unit vector directed from $Q_1$ to $Q_2$, and $\varepsilon_o$ is the *permittivity* of the space between the charges. This is the quantity that describes the way in which charges relate to one another through space. The *permittivity of free space,* $\varepsilon_o$, is $8.8 \times 10^{-12}$ Farads per meter (F/m).

If we consider the contribution of $Q_1$ regardless of other charges present, then $Q_1$ produces a *force field* that can be plotted in space. An electric field is defined as the electric force per unit charge, and Equation 2.1 reduces to [94]

$$\vec{F} = Q_2 \vec{E} \quad \text{……..…… (2.2)}$$

## 2.2 Electric Field Acting on the Particles

A uniform electric field is generated when a voltage is applied between two parallel large electrodes. On the other hand, a non-uniform electric field can be produced if one of the

electrodes is very small in physical dimension as compared to the other.

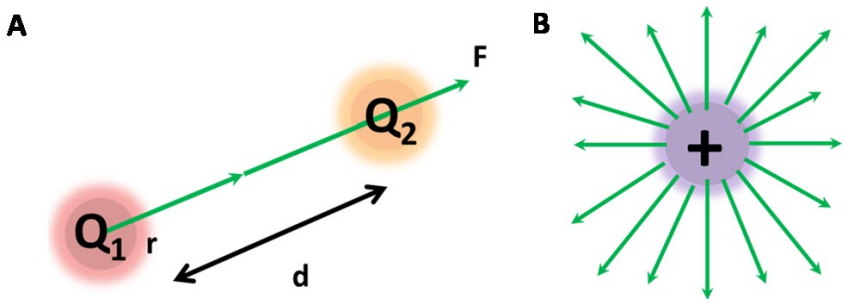


**Figure 2.1: Different charges between particles**

**(A) Two charges, a distance *d* apart along vector *r*, will experience a force in accordance with Coulomb's law. This force acts along vector *r* and is repulsive when the charges have the same polarity (as in the example here) or attractive when the charges have different polarity. (B) A point charge will generate an electric field from which force field lines are produced. (Reprinted with permission from M. P. Hughes, Nanoelectromechanics in Engineering and Biology, CRC Press 2002).**

Consider a polarizable particle exposed to an electric field. The applied electric field causes the formation of a dipole within the material and an accumulation of charges at the surface.[95] If the electric field is uniform, then Coulomb forces on the charges on both sides of the particle are equal and opposite, therefore, they cancel out and there is no net force on the particle (illustrated in Figure 2.2C).[96]

However, if the field is non-uniform (that is, varying in magnitude across the region occupied by the particle), then Coulomb forces on the opposite sides will be unequal, and there will be a net force acting on the particle (illustrated in Figure 2.2A, B).

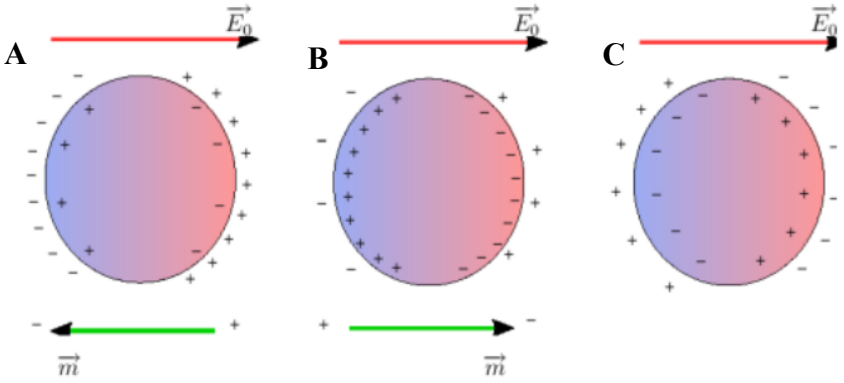


**Figure 2.2: Formation of dipoles in the particles**

**(A) The particle is barely polarizable as the surrounding environment so resulting dipole is colinear but with an opposite direction to $\vec{E}_0$ (B) the particle is very polarizable as compared to the surrounding environment, the resulting dipole is in direction of $\vec{E}_0$ (C) the particle is equally polarizable as the surrounding environment, hence no net dipole acts on the particle. (Adapted from MEMS World – Electrostatics, Part II: Dielectric sphere in a surrounding electrical field)**

This is called the *dielectrophoretic force* ($F_{DEP}$) and movement of the particle under this force is called *dielectrophoresis* (illustrated in Figure 2.3A).[97-99] However, the particle is neutral (containing no excess charge), and there is a uniform electric field *inside* it. The DEP force ($F_{DEP}$) acting on the spherical particles by the non-uniform electric field is given by:

$$F_{DEP} = 2\pi\varepsilon_m r^3 Re[K(\omega)]\nabla E^2 \quad (2.3)$$

where $r$ is the radius of the particle, $\varepsilon_m$ is the permittivity of the suspending medium, $\nabla E^2$ is the gradient of the square of the applied electric field, and Re[$K(\omega)$] is the real component of the complex Clausius-Mossotti (CM) factor. The importance of the CM factor will be explained in more detail in Section 2.4.

The Clausius–Mossotti factor, *K(ω)* is given as,

$$K(\omega) = \left( \frac{\varepsilon_p^* - \varepsilon_m^*}{\varepsilon_p^* + 2\varepsilon_m^*} \right) \quad \text{..... (2.4)}$$

which is dependent on the applied frequency (due to the frequency dependence of the complex permittivities), which can take values between +1 (when $\varepsilon_p^* \gg \varepsilon_m^*$ ) to -0.5 (when $\varepsilon_p^* \ll \varepsilon_m^*$ )[97,100]

The complex permittivity is given as

$$\varepsilon^* = \varepsilon - j\frac{\sigma}{2\pi f} \quad \text{.....(2.5)}$$

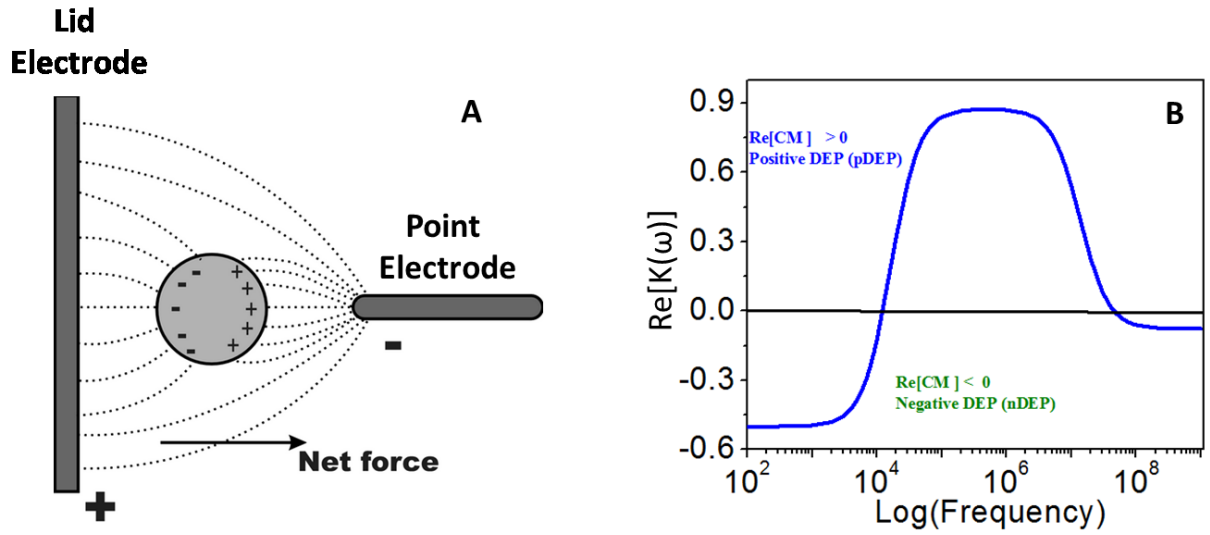


**Figure 2.3: Principle of Dielectrophoresis.**

**The figure consists of two electrodes configuration consisting of a small size electrode (point electrode) and the large electrode (lid electrode) electric field lines. A polarizable particle is place in the middle of the two electrodes. (B) The plot of real part of the Clausius Mossotti (CM) factor (Re[K(ω)]) and log of frequency (Hz) to show the positive dielectrophoresis (pDEP) region (above 0) and negative dielectrophoresis (nDEP) region**

**(below 0). (Reprinted with permission M.P. Hughes, H. Morgan, F. J. Rixon, *Eur Biophys J,* 2001, 30 (4), 268-72.)**

Since $(F_{DEP})$ is a vector, the direction of the force will change with the change in sign (illustrated in Figure 2.3B). If $Re[K(\omega)]$ is positive, then the force acts in the direction of the high field and is referred to as the positive dielectrophoresis (pDEP). However, if the value of $Re[K(\omega)]$ is negative, then the value of the force is negative, and the particle is repelled from regions of a high electric field. In such case, it is referred to as negative dielectrophoresis (nDEP).

## 2.3 Dielectric Manipulation of Bioparticles

DEP has been widely used to manipulate biological particles such as bacteria,[101] viruses,[102,103] spores,[104] yeasts,[105,106] , protozoas[97] and other eukaryotic cells[107] types, as well as proteins,[108] nucleic acids,[98] and other biomolecules. These bioparticles have a complicated internal structure and an inhomogeneous composition as compared to that of a solid homogeneous spherical particle. To account for their heterogeneous structure they are modeled by using a smeared-out multishell model to predict the DEP behavior of bioparticles, in particular, *E. coli,* and *Vaccina* virus. This kind of estimation will be very helpful when one wants to separate or manipulate a single bioparticle from a heterogeneous mixture.

### *2.3.1 Anatomy of Bacteria*

All bacterial cells contain a cell wall, cell membrane, cytoplasm, ribosomes and the chromosome. The average bacterium is 2 μm long and 0.5 μm in diameter, with a cell volume of 0.6 – 0.7 $\mu m^3$. The cell envelope is composed of the plasma membrane and cell wall. The

bacterial cell wall has peptidoglycan that is located immediately outside of the cytoplasmic membrane.

Peptidoglycan is made up of a polysaccharide backbone consisting of alternating N-acetylmuramic acid (NAM) and N-acetylglucosamine (NAG) residues in equal amounts. Peptidoglycan is responsible for the rigidity of the bacterial cell wall and the determination of cell shape. It is relatively porous and is not considered a barrier for small substrates.

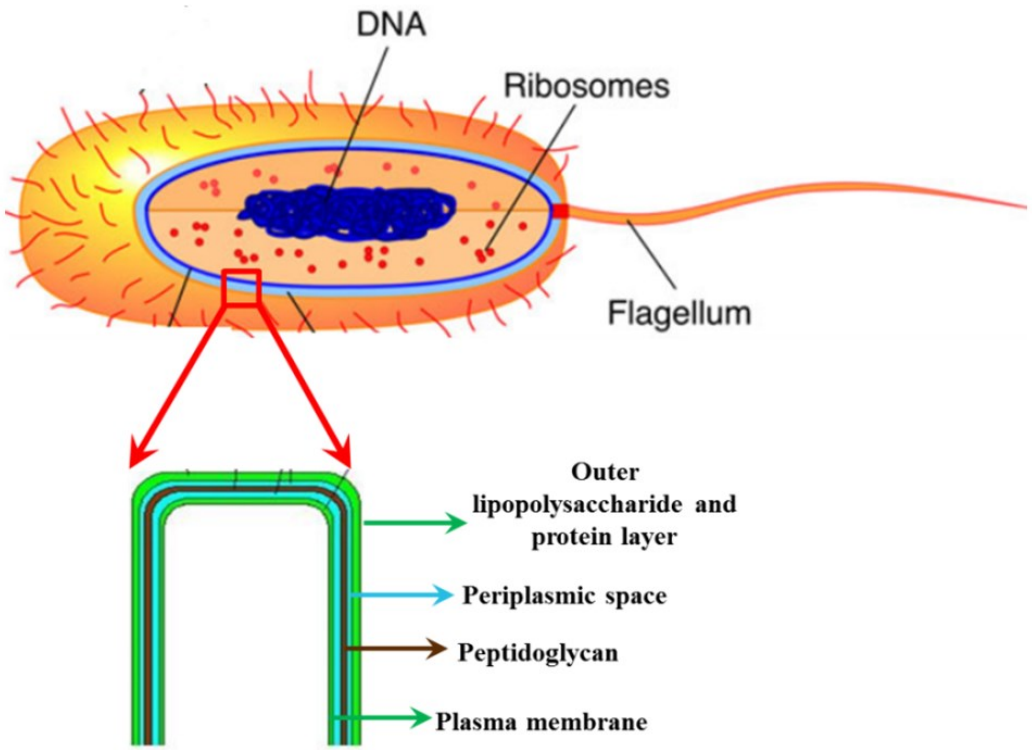


**Figure 2.4: Schematic diagram of bacterium**

**It consists of main characteristics of DNA, flagella and cell wall that further consists of four layers of outer lipopolysaccharide and protein layer, periplasmic space, peptidoglycan, and plasma membrane. (A part of the image is reprinted with permission from Clipart.com)**

The plasma membrane is composed of a phospholipid bilayer and thus has all of the general functions of a cell membrane such as acting as a permeability barrier for most molecules

and serving as the location for the transport of molecules into the cell. The bacterial DNA is not enclosed inside of a membrane-bound nucleus but instead resides in the bacterial cytoplasm (Figure 2.4).[110] This is important to note because the Clausius–Mossotti factor, K(ω) depends on the structure of the bacteria.[100,111]

### *2.3.2 Anatomy of Virus*

Viruses hold a unique classification in the world of microbiology. They are organisms that are not based on a cellular structure.[112] The anatomy of a virus is very different from that of cellular organisms (Figure 2.5).

Viruses are incapable of replicating independently. They are also not able to produce their own energy, nor can they make proteins. Most viruses are too small to be seen using standard light microscopes. Viruses are typically between 20 and 300 nm in diameter.[112] Viruses are often described as having different shapes, such as brick-shaped, rod-shaped, or spherical shaped, etc. The outer layer of the virus is made of a protein called capsid shown in Figure 2.5A.

Simplest of the viruses is *Bacteriophage*, which is a bacterial virus that infects the bacterial species *Escherichia coli.* The transmission electron microscope (TEM) image of *bacteriophage* resembles the schematic diagram (Figure 2.5B). The bacteriophage consists of a capsid that contains several subunits that are known as capsomeres. The geometrical arrangement of the capsomers gives a virus its physical structure and shape. The capsid proteins serve to protect the genetic material on the inside of the virus. They also serve to control the attachment of the virus to receptors on the cell that the virus will attempt to invade.

Some viruses have another structure surrounding the capsid. This structure is known as an envelope and is a lipoprotein membrane that is partially derived from the host cell that the virus is invading (Figure 2.5C). All viruses contain a core that is comprised of either DNA or

RNA, but never both. The central core of the genetic material is surrounded up by a protective protein coat.[112] During infection, the phage particle recognizes and binds to its host (*E. coli*) by the tail fibers causing DNA in the capsid of the phage to be injected through the tail into the cytoplasm of the bacterial cell. The new DNA from phage overtakes the function of the bacteria cell, DNA, and all different parts of the phages are produced within the bacterial cell.

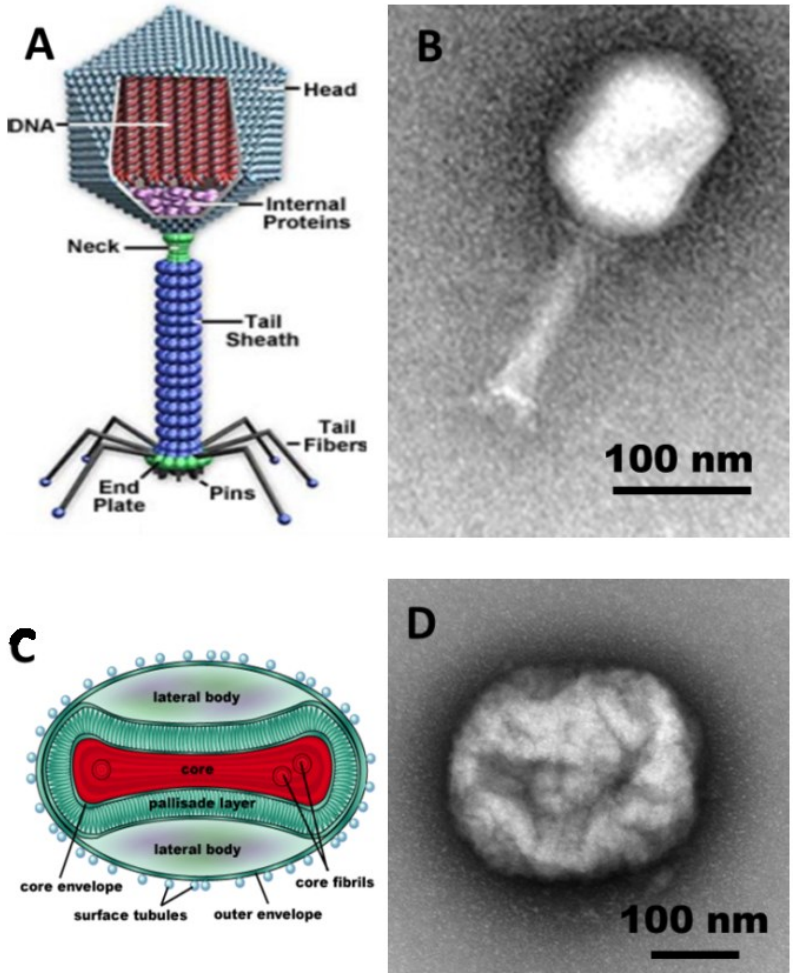


**Figure 2.5: Schematic and transmission electron microscope images of the viruses.**

**(A) Schematic image of the DNA bacterial virus (*bacteriophage*) consisting of a protein head with DNA and tail. (B) TEM image of bacteriophage showing similar characteristics. (C) Schematic diagram of a *Poxviridae* family having a rounded brick shaped consisting of**

**the envelope of endoplasmic reticulum, lipoprotein membrane envelope, and DNA. (D) TEM image of *Vaccinia* virus showing similar characteristics) (Reprinted with permission picture *Bacteriophage Life Cycle*, from the laboratory Planet blog, and *Introduction to Viruses that Infect Humans: The DNA Viruses* from Microbiowiki.com)**

This is followed by cell lysis, releasing the cell contents, including virions that have been assembled, into the environment. This is called as a *lytic cycle*.[113] The information on the production of the viruses in the laboratory is given in Appendix A.1 (page 163) and enumeration of the viruses with double layer agar technique is given in Appendix A.2 (page 165). The *Vaccinia* virus is a large, complex, enveloped virus belonging to the poxvirus family. The dimensions of the virion are roughly 360 × 270 × 250 nm (Figure 2.5D), containing double-stranded DNA genome. The DNA is encapsulated with a lateral body and palisade layer. The virus is enveloped with a lipid bilayer membrane consisting of lipoproteins.[114]

## 2.4 Predicting Clausius Mossotti factor using Homogeneous Sphere Model

To predict the DEP response of *E. coli* cells,[115] it is convenient to model it as a sphere covered with two shells (inner shell: cytoplasmic membrane, outer shell: cell wall) as shown in Figure 2.6. The shell model can be solved from the inside shell (shell 4) to the outside shell (shell 3 and shell 2) given by Equation 2.6, 2.7, and 2.8. Different scenarios of the dependence of CM factor based on the conductivity of the medium can be inferred using the Equation 2.8 and the values presented in Table 2-1.

The parameters used for the calculation of $\varepsilon_{eff}^{*}$ for *virus* cells can be found from previous reports,[116-120] that are listed below in Table 2-2.

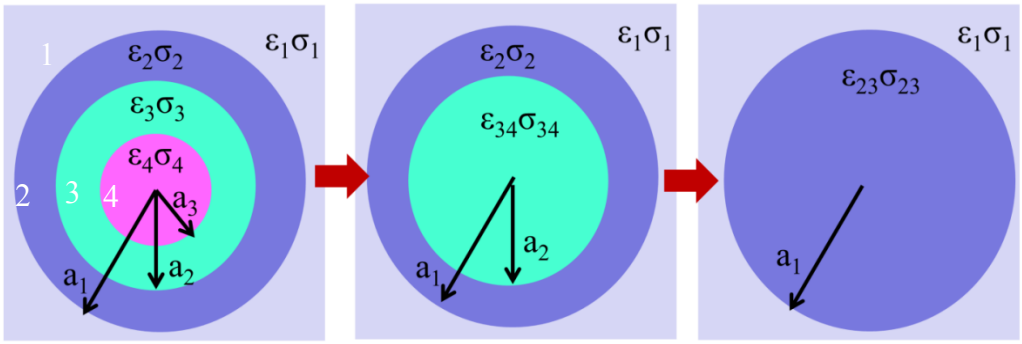


**Figure 2.6: Two shell sphere model for bacteria**

***E.coli*** **with radius of 1 µm with cell wall conductivity 0.5 S/m, permittivity 60, and thickness 20 nm, cell membrane conductivity 5 × $10^{-8}$ S/m, permittivity 10, and thickness 5 nm, and cytoplasm conductivity 0.1 S/m, permittivity 60.**

Solving for the shell 4 (cytoplasm) and shell 3 (cell membrane) using Clausius – Mossotti factor Equation 2.4 and the values of permittivities of cytoplasm and cell membrane along with their thickness is obtained from Table 2.1. The following equation was used to obtain complex permittivity of $\varepsilon_{34}$,

$$\bar{\varepsilon}_{34} = \bar{\varepsilon}_3 \frac{\left(\frac{a_2}{a_3}\right)^3 + 2\left(\frac{\bar{\varepsilon}_4 - \bar{\varepsilon}_3}{\bar{\varepsilon}_4 + 2\bar{\varepsilon}_3}\right)}{\left(\frac{a_2}{a_3}\right)^3 - \left(\frac{\bar{\varepsilon}_4 - \bar{\varepsilon}_3}{\bar{\varepsilon}_4 + 2\bar{\varepsilon}_3}\right)} \quad \text{..... (2.6)}$$

Solving for shell 34 (from Equation 2.6) and shell 2 (cell wall), to obtain $\varepsilon_{234}$

$$\varepsilon_{234} = \varepsilon_2 \frac{\left(\frac{a_1}{a_2}\right)^3 + 2\left(\frac{\bar{\varepsilon}_{34} - \bar{\varepsilon}_2}{\bar{\varepsilon}_{34} + 2\bar{\varepsilon}_2}\right)}{\left(\frac{a_1}{a_2}\right)^3 - \left(\frac{\bar{\varepsilon}_{34} - \bar{\varepsilon}_2}{\bar{\varepsilon}_{34} + 2\bar{\varepsilon}_2}\right)} \quad \text{..... (2.7)}$$

Finally, combining the 3 shells, (i.e. shell 4 (cytoplasm), shell 3 (cell membrane) and shell 2 (cell wall) with medium to obtain the final equation for Clausius Mossotti factor,

$$f_{CM234} = \frac{\bar{\varepsilon}_{234} - \bar{\varepsilon}_1}{\bar{\varepsilon}_{234} + 2\bar{\varepsilon}_1} \quad \text{..... (2.8)}$$

**Table 2-1: *E.coli* parameters for calculating Re[K(ω)][115]**

| ***Shell No.*** | ***E.coli* Parts** | **Parameters** | **Values** |
|---|---|---|---|
| 4 | Cytoplasm | Conductivity<br>Relative permittivity | $\sigma_4 = 0.1$ S/m<br>$\varepsilon_4 = 60$ |
| 3 | Cell membrane | Conductivity<br>Relative permittivity | $\sigma_3 = 5 \times 10^{-8}$ S/m<br>$\varepsilon_3 = 10$<br>Thickness ($a_2$) = 5 nm |
| 2 | Cell Wall | Conductivity<br>Relative permittivity | $\sigma_2 = 0.5$ S/m<br>$\varepsilon_2 = 60$<br>Thickness ($a_1$) = 20 nm |
| 1 | Suspension<br>(Water) | Conductivity<br>Relative permittivity | $\sigma_1 = 2 \times 10^{-4}$ S/m<br>$\varepsilon_1 = 80$ |
| | Simulated shape of *E.coli* | Sphere | Radius = 1 μm |

The only parameter that can be varied is the conductivity of the suspending medium and in most of the DEP experiments, water or buffer is preferred as the suspending medium.

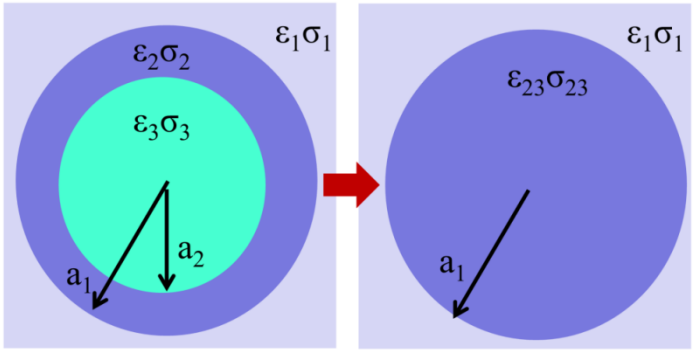


**Figure 2.7: Schematic of two shell- model approach for calculating effective permittivity ($\varepsilon_{eff}^{*}$) of *Vaccina* virus.**

Similar kinds of predictions about the CM factor can also be performed for smaller bioparticles like *Vaccinia* virus. In the case of viruses, the model is simpler due to the absence of a cell wall and cell membrane, as shown in Figure 2.7. The parameters for the *Vaccinia* virus are tabulated in Table 2.2. CM factor vs. different frequencies of the AC voltage at various suspending medium conductivities of the *E. coli* cells and *Vaccinia* virus are shown in Figure 2.8 Suspending medium conductivities of 0.1, 0.01, and 0.001 S/m were selected, in this case.

## 2.5 Other Forces Acting on the Bioparticles Fluidic Flow

### *2.5.1 Viscous Drag and Sedimentation Force*

The viscous drag is responsible for retarding the motion of any particle moving through anything other than a vacuum.[121] The velocity at which the particles move is directly related to

the magnitude of the force propelling them through the medium and inversely related to the viscosity of the medium.

**Table 2-2: Parameter values used for theoretical predictions of Re[CM(ω)] for 300 nm V*accina virus*[116]**

| Shell No. | Component | Parameter | Value |
|---|---|---|---|
| 3 | Bulk | Relative permittivity($\varepsilon_3$) | 65 |
| | | Conductivity ($\sigma_3$) | $1.6 \times 10^{-1}$ S/m |
| 2 | Membrane | Relative permittivity ($\varepsilon_3$) | 10.3 |
| | | Conductivity ($\sigma_2$) | $0.19 \times 10^{-9}$ S/m |
| | | Thickness | 20 nm |
| 1 | Suspension medium (DI water) | Conductivity ($\sigma_1$) | Variable S/m |
| | | Relative permittivity ($\varepsilon 1$) | 80 |

For a spherical particle of radius *r*, the Stokes's law describes the terminal velocity (*v*) of a particle through a medium by

$$v = \frac{F}{6\pi\eta r} \quad \text{..... (2.9)}$$

Small bio-particles (<200 nm) will not precipitate because of the Brownian motion making them float in the medium.[122] The larger bioparticles such as 250 nm diameter such as *Herpes* viruses and *Vaccinia* viruses, which are somewhat denser than water, can sink over time.[100] The magnitude of sedimentation force is given by Equation 2.10, where $\rho_p$ and $\rho_m$ are the densities of the particle and medium, respectively, $v$ is the particle volume, and $g$ is the gravity.[123]

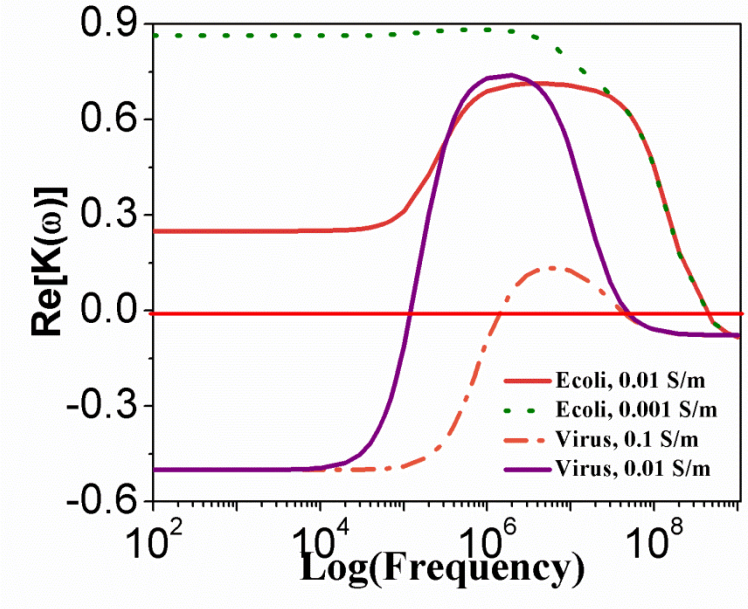


**Figure 2.8: The plot of the real part of Clausius Mossotti factor Re[K(ω)] and log frequency (Hz) for viable *E.coli* and *Vaccinia* virus at different medium conductivities.**

**The plot helps in estimation of the frequencies that are useful in the separation of one of the bioparticle from a heterogeneous mixture of bacteria and virus.**

$$F_{sediment} = v(\rho_m - \rho_p)g \quad \text{..... (2.10)}$$

The sedimentation force on the small colloidal particles is minimal compared with other forces and can be neglected.[100]

### *2.5.2 Brownian Motion and Diffusion*

As the particle size is reduced, the effects of the Brownian motion become increasingly significant. Brownian motion is the random motion of the particle. To move an isolated particle in a specific direction, the forces like electrohydrodynamic force and dielectrophoretic force (DEP) must be high. The magnitude of the Brownian motion will be highest when the other forces are not acting on the isolated particle. The particle displacement due to Brownian motion follows a Gaussian distribution profile and is calculated by the root mean square of the particle displacement, $X_{rms}$, is given by[124]

$$X_{rms} = \sqrt{2DT} \quad \text{..... (2.9)}$$

where $D$ is the diffusion coefficient and $T$ is the temperature. The diffusion coefficient is given by the Stokes-Einstein Equation where $d_p$ is the diameter of the particle, μ is the viscosity of the medium, and $k_B$ is Boltzmann constant.[125]

$$D = \frac{k_B T}{6\pi\mu d_p} \quad \text{..... (2.10)}$$

The diffusion force is used to describe the behavior of the particles in solution moving from a high to low concentration region.

The above equations imply that the resulting particle movement depends on the size and density of the particle, viscosity of the medium, and temperature, which affect Brownian, sedimentation, and diffusion forces. The relative strengths of these forces are overcome by the high electrohydrodynamic drag force in the direction of flow and dielectrophoretic force, which will be considered extensively in future studies.

# Chapter 3 - Fabrication and Characterization of Vertically Aligned Carbon Nanofiber (VACNF) Nanoelectrode Array (NEA)

## 3.1 Introduction

The electrodes that have one of the critical dimensions smaller than 25 μm are called ultramicroelectrodes and are used for development of fast electron transfer reaction electronics.[127] Nanoelectrode array (NEA) scheme is attractive because of increased temporal and spatial resolution, high sensitivity, and less background noise. However, reliable methods to fabricate these electrodes are still lacking. Carbon nanofibers (CNFs) NEA are explored in this research.

CNFs are cylindrical or conical structures that have diameters varying from tens to hundreds of nanometers and lengths ranging from less than a micron to millimeters. A nanofiber consists of stacked curved graphite layers that form cones or cups stacked on each other often referred to as herringbone or fishbone structures (Figure 3.1).[128,129] The primary characteristics distinguishing the nanofibers from the nanotubes is the stacking of graphene sheets of varying shapes, causing differences in the mechanical strength and the electric properties.[99] The difference in the angle (α) between the fiber's axis and the graphene sheet at the sidewall, with the CNF is $\alpha > 0$.[130-132] The whole surface area at the sidewall of CNFs can be activated due to the free edge sites.[100]

The fiber's diameter can be varied anywhere from 50 nm to 300 nm and even wider, through variation of several parameters. The nanofibers oriented perpendicular to the substrate are commonly called vertically aligned carbon nanofibers (VACNFs).133 Due to the well-defined graphitic structures, VACNF present similar chemical properties as conventional carbon electrodes with a flexible surface chemistry, excellent biocompatibility, and wider potential window. The fabrication of NEA using VACNFs described by J.Li., et al.[101-107] is used in this

research.

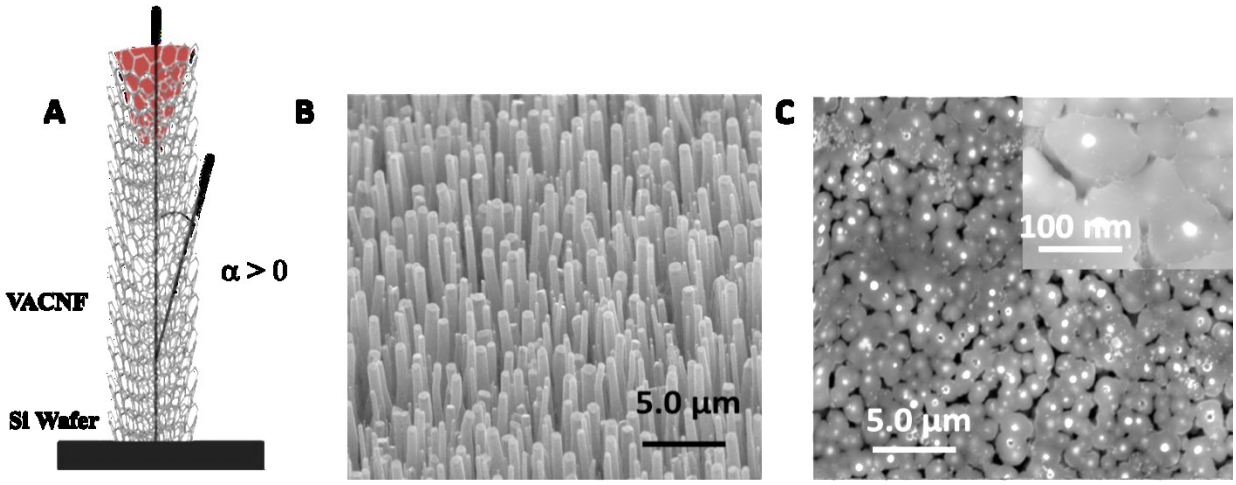


**Figure 3.1 Carbon nanofiber nanoelectrode array**

**(A) Schematic of VACNF internal structure depicting the stacked graphene cups and α the angle between the fiber axis and the graphene sheets (B) SEM image of VACNF random array (C) Embedded CNF tips exposed on a silicon chip.**

## 3.2 Fabrication of Carbon Nanofiber NEA

The fabrication of the CNF NEA involves four major steps is given as (1) Contact metal (chromium, Cr) and catalyst (nickel, Ni) deposition on a silicon (Si) (100) substrate, (2) plasma enhanced chemical vapor deposition (PECVD) of vertically aligned CNFs, (3) $SiO_2$ encapsulation, (4) chemical mechanical polishing (CMP) and reactive ion etching (RIE) to expose the tips of embedded CNFs. The sequences of steps involved in the fabrication process are shown in Figure 3.2. The experimental details of each step are discussed below.[102, 108]

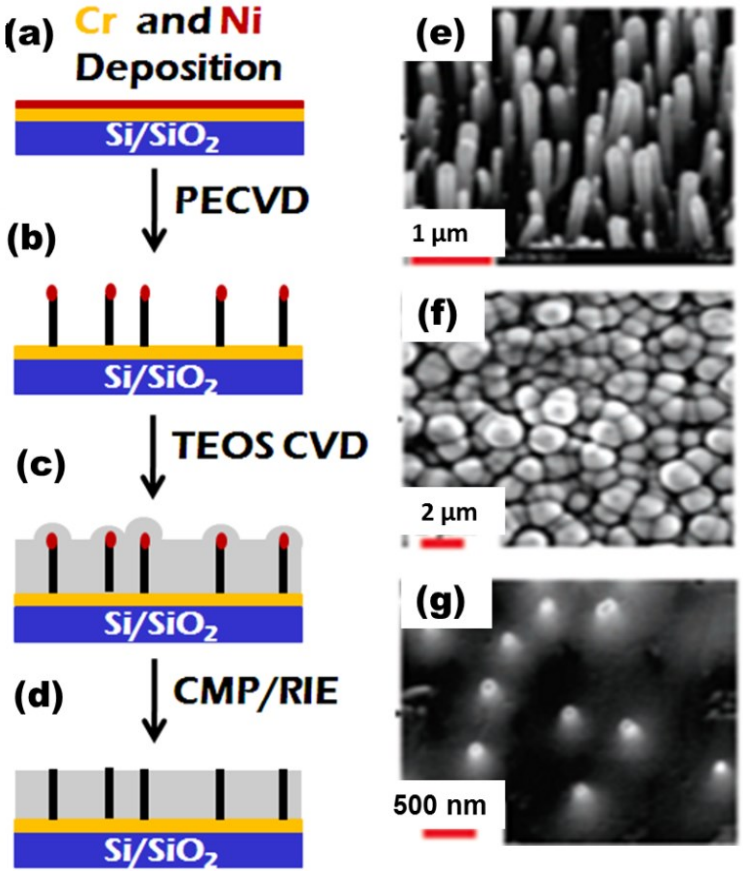


**Figure 3.2: Schematic diagram of the steps involved in the fabrication process of VACNF NEA.**

**(A) Ion beam sputtering of Chromium (100 nm) and Nickel (22.5 nm). (B) Plasma Enhanced Chemical Vapor Deposition (PECVD) using $C_2H_2$ and $NH_3$ gases at 775ºC. (C) Encapsulation of VACNFs with $SiO_2$ using TEOS-CVD. (D) Chemical mechanical polishing of the VACNF chip using 0.05 µm of alumina slurry and exposure to reactive ion etching to expose the CNF tips. (E) SEM image of freestanding "as-grown" vertically aligned CNFs (45°view) after PECVD. (F) SEM image (perpendicular) of CNFs after being encapsulated by $SiO_2$ using TEOS-CVD. (G) SEM image of an embedded CNF NEA after reactive ion etching and mechanical polishing. (Reprinted with permission from J. Li,**

**Q. Ye, A. Cassell, H. T. Ng, R. Stevens, J. Han, M. Meyyappan, *Appl. Phys. Lett.*, 2003, 82, 2491-2493.)**

### *3.2.1 Contact Metal and Catalyst Deposition*

The first step in the fabrication process is the sputter coating a 1 cm × 2 cm Si substrate with Cr and Ni as shown in Figure 3.2A. A Gatan ion beam sputter coater was used to perform this step. Si substrates were sonicated in ethanol 100% for 10 min and dried at 100º C and coated with 100 nm of Cr and 22.5 - 20 nm of Ni using an ion beam sputter with energy of 10.0 keV. During the deposition, the sample was rotated at 30 rpm, tilted at 5º and rocked at a rate of 12º/s. The coating rate was adjusted to 1.0 Å/s for Cr and 0.6 Å/s for Ni, so as to prevent overheating of the metal source. The purpose of coating Cr, Ti (10 nm, Merkulov, I. V., et al.[103]) layer is that it acts as an adhesion layer and contact layer that connects millions of nanoelectrodes (NEs) and also prevents the formation of Ni silicide. Ni acts as a catalyst for the growth of carbon nanofibers (CNFs).

### *3.2.2 Plasma Enhanced Chemical Vapor Deposition (PECVD) for VACNF growth*

After the metal layers were deposited, a random array of VACNFs can be grown on the coated silicon wafer using an Aixtron Black Magic PECVD system as shown in Figure 3.1 and Figure 3.2B. The main purpose of using plasma enhancement was to reduce the activation energy for a deposition process. The gas showerhead was used to produce a uniform gas flow distribution over the entire substrate surface. First, coated Si chips were loaded in the chamber that goes through two cleaning cycles using Nitrogen (999 sccm) as a cleaning gas. The Ni catalyst on Si chips coated in the previous step was annealed at 500º C for 60 s in vacuum with a base pressure of ~0.11 mbar. Then, the wafer was exposed to acetylene ($C_2H_2$) that acts as a source of carbon and ammonia ($NH_3$) serves as an etching and reducing gas with flow rates of

63-70 and 250 sccm, respectively and with the processing pressure of 5.48 - 5.61 mbar. The sample was then heated to 775 º C while the DC plasma (520 V and 40 W drive) was applied. At this temperature, plasma conditions, and 20 min deposition yields a VACNF array with fiber diameters of 50-100 nm and the length of ~5 μm, as verified by the SEM as shown in Figure 3.1B. Each CNF was vertically aligned and freestanding on the surface of the Si substrate.

Some detailed experiments were done by Merkulov, et al.[103] and they concluded that the morphology of well-separated VACNFs had a strong dependence on the gas mixture used in PECVD a function of the $C_2H_2/NH_3$ ratio. With relatively small acetylene content, isolated VACNFs with kinks and significantly damaged walls were produced, and with higher acetylene content, the VACNF were straighter with significantly less damage to the walls. The tip-type carbon nanofiber growth mode was observed, where a catalyst is detached from the substrate and remains at the tip of the growing nanostructure.[109] The nucleation and growth of graphene layers were found to be assisted by a dynamic, repetitive formation and restructuring of monoatomic step edges at the nickel surface. The initial diameter of the nanoparticles, $d$, is roughly determined from mass conservation of the catalyst, that is, $d = (3/2tD^2)^{1/3}$, where $D$ is the diameter of the catalyst dot and $t$ is its thickness.[109, 110] However, as the Ni is coated with a film the diameter of the catalyst during the procedure is not determined, in this case. This becomes crucial during the fabrication of patterned VACNF where Ni catalyst is deposited in a particular area using e-beam lithography.[111] The parameters that constitute this multidimensional space include 1. total pressure, 2. total gas flow, 3. carbon source to etchant gas flow ratio, e.g.,$C_2H_2/NH_3$, 4. substrate temperature, 5. plasma power.

### *3.2.3 Silicon Dioxide ($SiO_2$) Encapsulation*

The as-grown CNF substrate was coated with silicon dioxide ($SiO_2$) using chemical vapor deposition (CVD) system in order to insulate the bottom Cr layer, provide robustness to VACNF, and stability of the hydrophilic environment. As shown in Figure 3.2C. CVD involves the adsorption, desorption, evolution, and incorporation of vapor species at the surface of a growing film. Since the heat is the primary energy source for reactions to occur, the CVD process is also often referred to as thermal CVD.[112] The home built tube furnace from Thermo Electron Corporation was used at the base pressure of <100 mTorr, the chamber (with as-grown CNF chip) was heated to 720°C.[106] Tetraethyl orthosilicate (TEOS, a precursor for $SiO_2$) was deposited at a vapor pressure of ~250 mTorr or 6 hrs and ~350 mTorr for 6 hrs. $SiO_2$ forms a conformal film, filling the free space between the individual fibers, as well as the substrate. To ensure complete coverage of the carbon nanofibers (CNFs), the CVD process was continued for 12 hr as shown in Figure 3.2F.

### *3.2.4 Mechanical Polishing and Reactive Ion Etching (RIE)*

The excess $SiO_2$ and part of the CNFs were removed by the combination of mechanical polishing to planarize the substrate using a slurry of abrasive material in an alkaline or acidic solution and reactive ion etching (RIE) techniques. Polishing was performed manually using 0.05 μm Alpha micropolish alumina (Buehler, Lake Bluff, IL) for 2.5 hrs smooth wafer surface with a high degree of flatness. The final wafer surface was a black shiny mirror-like finish. RIE (Nano-Master, NRE3000) was then used to etch away $SiO_2$ from the top and expose the tips of CNFs as shown in Figure 3.1D. Oxygen (10 sccm) and $CHF_3$ (2 sccm) gasses at 200 W and 250 mTorr were used to etch the dielectric surface. The density of the exposed CNF tips can be easily controlled by the etching time. Electrical resistance at the surface of the nanoelectrode array

(NEA) chip was measured using two-point probes of a handheld multimeter to monitor the progress of the etching and the number of exposed CNFs. Routine practice is to repeat the polishing/etching procedure with the NEA chip until the resistance measured using a multimeter was between 500-1000 Ω. The SEM image of exposed VACNF tips as shown in Figure 3.1C.

## 3.3 Electrochemical Measurements

### *3.3.1 Electrochemical Set-up*

To characterize the carbon nanofiber nanoelectrode array (CNF NEA), a direct current (DC) cyclic voltammetry (CV) were performed using CHI440A (CH Instruments) in a standard 3-electrode set-up.

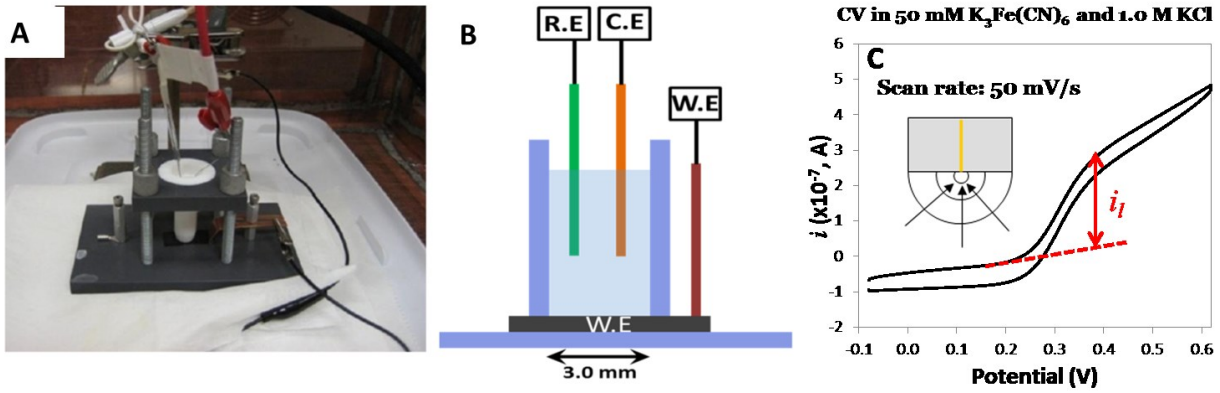


**Figure 3.3: Characterization of the VACNF**

**(A) Shows 3-electrode set-up using a Teflon cell with the working electrode at the bottom. (B) Cross-sectional schematic of the same cell (C) Representative cyclic voltammetry curve of VACNF tips exposed.**

A typical electrochemical experimental set- up is shown in Figure 3.3A. A Teflon cell with a 3 mm inside diameter O-ring that makes a seal with a NEA chip and serves as a working

electrode (W.E), Pt wire as a counter electrode (C.E) and Ag/AgCl (sat'd KCl) as the reference electrode (R.E). Figure 3.3C is the typical CV plot obtained with a scan rate of 50 mV/s and peak height $i_l$.

## 3.4 Carbon Nanofiber Applications

Nanoelectrodes are mainly used because of the advantage of high signal to background ratio. The background current mainly from the capacitive charging/discharging current at the electrode/electrolyte interface and thus proportional to the surface area ($A$) of the inlaid electrode, i.e., where $C_d$ is the specific capacitance at the interface.[113]

$$i_b \alpha C_d^0 A \quad \text{..... (3.1)}$$

In most common voltammetry measurements, the magnitude of the peak current of the redox signal is the sum of two terms: a linear diffusion as described in the Cottrell Equation and a nonlinear radial diffusion

$$i_{peak} = nFAC_0 \times \sqrt{\frac{D_0}{\pi t}} + nFAC_0 \times \left(\frac{D_0}{r}\right) \quad \text{..... (3.2)}$$

where n is the number of electrons involved in the reaction with one electroactive species, $i_{peak}$ is the peak current, $F$ is the Faraday constant, $C_0$ is the concentration of electroactive species, $D_0$ is the diffusion coefficient, $t$ is time, and $r$ is the electrode radius. As the radius is decreased below 25 μm, the second term increases and dominates the signal, which is typically observed in ultramicroelectrodes (UME).[113]

$$\frac{i_{peak}}{i_b} \alpha \frac{nFC_0 D_0}{r} \quad \text{..... (3.3)}$$

The signal-to-background ratio will be improved by 1000 times when going from 200 μm to 200 nm when electrode size is decreased. At the same time, the electrode also responds 1000

times faster giving high temporal and spatial resolution that scales inversely with the electrode radius. Therefore, the sensitivity can be dramatically improved by reducing the size of the electrodes to the nanoscale. For practical applications, hundreds of nanoelectrodes are desired to be attached to each microelectrode as a local nanoelectrode array in order to increase the statistical reliability.[114, 115]

### *3.4.1 Nanoelectrode Array for Pathogen Sensing*

The two-dimensional (2D) finite element modeling of positive dielectrophoresis was employed to simulate the high dielectrophoretic force at the tips of VACNF by Arumugam, P. U. et al.[116] The simulation was performed using a linear array of 12 CNF NEs at 26 $V_{pp,}$ and a flow velocity of 10 mm/s is shown in Figure 3.4.

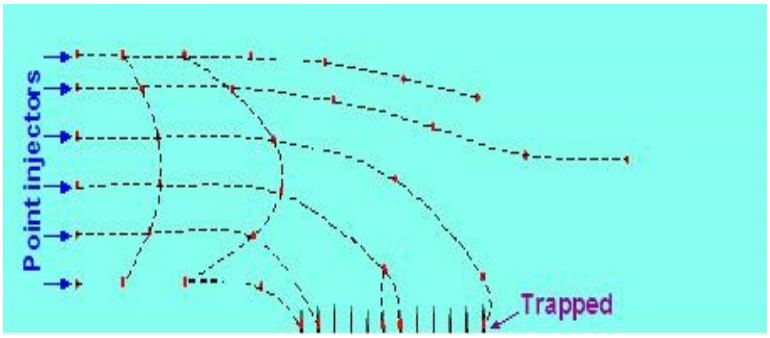


**Figure 3.4: Modeling of pDEP trapping on CNF NE array.**

**The dashed lines show the trajectories of 1 μm diameter particles under the influence of Stokes drag force of a 10 mm/s flow and dielectrophoretic forces by a 10 MHz AC voltage of 26 $V_{pp}$. (Reprinted from P. U. Arumugam, H. Chen, A. M. Cassell, J. Li, *J. Phys. Chem. A*, 2007, 111, 12772-12777.)**

The particles of 1.0 μm in diameter were injected at various heights simulating *E. coli*. The trajectories show that all particles injected below 12 μm height were trapped while others

(including those near the 20 μm high ceiling) were deflected downwards in the presence of the high electric field. The efficiency of trapping with this design was significantly greater due to the high electric field generated at the tip of CNF. The electric field calculated around a nanoelectrode (NE) tip shows a maximum of ~1.2 × $10^{14}$ $V^2$ /$m^2$ that is 200 times higher than that of the micro- "points-and-lid" device. At the flow velocity of 10 mm/s that is extremely high than used in micro- "points-and-lid" device (0.1-0.5 mm/s) and interdigitated device (0.04-2 mm/s), resulted in capture reflecting the higher trapping efficiency.[110, 116]

## 3.5 DEP device Fabrication

Fabrication of device involves five major steps:[106, 117]

**(1)** Embedded VACNF NEAs were made by the method described earlier (see section 3.2).

**(2)** SU-8-2002, a negative tone photoresist (Microchem, Newton, MA) of ~2.0 μm in thickness was used to develop patterns on the planarized nanoelectrode array (NEA). The substrate was cleaned by rinsing with acetone several times, blow-dried in the air and dehydrated at 150º C for 20 min in an oven (Fisher Scientific). SU-8 2002 was spin coated on the NEA chip at 2800 rpm speed for 40 sec using a spin coater. It was soft-baked at 95ºC for 75 sec on a hot plate, exposed to UV light (22.8 mW/$cm^2$) for 4.64 sec through a Mylar mask in soft contact mode to define a 200 μm × 200 μm active area, post baked for 90 sec on a hot plate at 95º C, developed in SU-8 developer, and washed with isopropyl alcohol (IPA) and dried using a stream of Nitrogen gas.

**(3)** SU-8-2010, a negative tone photoresist (Microchem, Newton, MA), for thicker coating of ~18 μm in thickness was deposited on a 2 cm × 4 cm ITO-coated glass electrode by spin coating SU-8 2010 at 1350 rpm speed for 40 sec. It was then soft baked at 95ºC for 4 min on a hot plate, exposed to UV light (28.4 mW/$cm^2$) for 8.83 sec through the second Mylar mask to

define the microchannel and circular chamber, post baked for 4 min at 95ºC on a hot plate. The remaining steps were the same as explained for NEAs. Finally, two holes were drilled from glass side using a 0.75 mm diameter diamond drill bit at the two ends of the microchannel and then a section (1 cm x 2 cm) of ITO-glass electrode containing the microchannel was diced to eliminate edge-beads, which may interfere with the bonding process.

**(4)** SU-8 patterned NEA and ITO-glass electrodes were cleaned with isopropyl alcohol (IPA) to remove dust particles. Alignment markers on both the substrates were used to align them under a regular tabletop microscope with a 4X objective lens and then a mechanical force was applied to hold the substrates together. Subsequently, the substrates were placed in a vacuum oven (Curtin Matheson Scientific, Inc) which was preheated to 175 ºC. It was evacuated and held at 25 Torr for ~40 min for the substrates to bond with each other.

**(5)** Electrical connections to the electrical pads on the NEA and ITO-glass were made using conductive silver epoxy (MG Chemicals, Ontario) and thirty gauge wire. Microbore tubing was connected to a 1 ml glass syringe to the DEP device using sleeves, ferrules and fittings (Upchurch Scientific Inc, WA). A syringe pump (NE-1000, New Era Pump Systems, Inc) was used to control the flow rate during the experiment.

### *3.5.1 DEP Device Set-up*

To observe the fluorescence signal, the device was placed under a Carl Zeiss microscope, using the 4X objective to visualize the active region. The Hamilton syringe 1 ml was connected with the device using microbore tubing and a constant velocity of the solution allowed to flow into the device using a syringe pump. To avoid biofouling within the device, it was necessary to flow 5% BSA solution at a very low speed (~ 0.10 µl/min) and then washed with water at (~5.0

µl/min). To avoid any bubbles in the system, the microbore tube was filled with the fluid under use and then connected to the device.

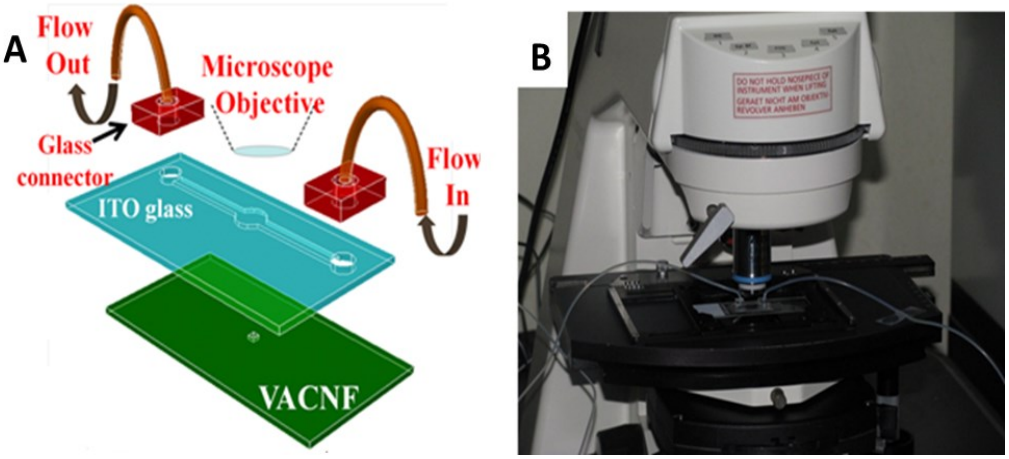


**Figure 3.5: Set-up of microfluidic chip under microscope**

**(A) Shows the schematic image of the microfluidic chip consisting of CNF chip and ITO glass surface along with the glass connectors and microbore tubing. The microfluidic chip can be set under a microscope where the objective of the microscope is focused on the 200 µm × 200 µm area. (B) Actual set-up of the device connected with tubing settled under 50 X objective of Carl Zeiss FS 2 plus microscope. (Reprinted with permission from F. R. Madiyar, L. U. Syed, C. T. Culbertson, J. Li, *Electrophoresis,* 2013, 34, 1123-1130.)**

# Chapter 4 - Manipulation of Bacteriophages by Dielectrophoresis on Carbon Nanoelectrode Array[†]

## 4.1 Introduction

Rapid detection of pathogens like bacteria and viruses is of great importance for monitoring water and food quality, the early detection and diagnosis of diseases, countering bioterrorism attacks and other applications. Successful detection requires the manipulation and capture pathogenic particles for further analysis. Optical tweezers,[118] acoustic forces,[119] and surface interactions have been used to manipulate bioparticles physically. Another attractive approach is the use of electrical force such as electrophoresis (EP) and dielectrophoresis (DEP) to manipulate cells.[116, 120-122] DEP is of particular interest for capturing pathogenic particles stably in isolated locations of a device. Pohl described the fundamental principles of DEP in 1970s.[123] It deals with the motion of a dielectric particle due to polarization effects in a nonuniform electric field. DEP discriminates particles based on their intrinsic dielectric property that, to some extent, adds selectivity in the manipulation of one type of bioparticle from a heterogeneous mixture. DEP has been extensively used as a nondestructive and noninvasive technique to detect and separate bacteria, discriminate between live or dead bacteria depending on the conductivities and permittivities of the cell membrane and medium[124], identify isogenic mutants of *E. coli* differing exclusively in one mutant allele,[125] and capture and lyse smaller particles like viruses.[126]

Conventionally DEP has been performed using patterned interdigitated electrodes (IDE)

---

[†] Reproduced in part by permission of the John Wiley and Sons, F. R. Madiyar, L. U. Syed, C. T. Culbertson, J. Li, Manipulation of bacteriophages with dielectrophoresis on carbon nanofiber nanoelectrode arrays, *Electrophoresis*, 2013, 34, 1123-1130. DOI: 10.1002/elps.201200486.

and the collection of bacteria mainly takes place at the edges of the electrode.[127, 128] However, in many applications one needs to manipulate single cells and preferably capture those cells isolated spots instead of allowing them to aggregate. Another problem associated with the IDE is that the electrodes are laid at the bottom of the fluidic channel, and the $\nabla E^2$ decreases rapidly further away from the channel bottom. To deal with these problems, reversible dielectrophoretic capture and release of a single *E. coli* employing NEA in "points-and-lid" geometry was developed.[116] Fabrication of well-controlled NEAs using VACNFs embedded in insulating materials on Si substrates has been reported earlier. The exposed tips of VACNFs serve as a point's array electrode and a large transparent indium-tin-oxide (ITO) electrode at the top acts as the lid. Recently, it has been reported that precise e-beam lithographically patterned VACNFs can be fabricated as embedded NEAs on individually addressed micropads on the 4" wafer scale.[111] This extends the use of embedded VACNF NEAs for either single or multiplex detection.

This chapter discusses the fabrication of microfluidic device utilizing exposed tips of embedded VACNFs as active nanoelectrodes in a selected area to capture virus *Bacteriophage* T4r.[117] The active area is defined by a 2-μm thick SU-8 photoresist to minimize the distance between the nanoelectrodes (NEs) and the *virus* cells flowing through the channel. It has been reported that the electric field can be enhanced with a non-planar structure with high aspect ratios (~100) as offered by fiber-like NEs.[129, 130] The enhanced E-field at NEs in solution was also observed.[106, 116, 131] We demonstrate here that the attractive nanoscale "point-and-lid" design and the increased enhancement in the electric field gradient lead to effective capture of *virus* at a high flow velocity up to 1.6 mm/sec.[117]

## 4.2 Experimental Details

### *4.2.1 Materials and Reagents*

To make the assembly for bacteriophage culture, conical flasks (50 mL, Pyrex®), rubber stopper with holes (O.D= 3.15mm) with tubes (O.D= 3.12mm) was obtained from Fisher Scientific. *Bacteriophage* T4r and *E.coli* B stock solutions were obtained from Carolina Biological Supply Company (121150) and *Bacteriophage* T1 was obtained from ATCC (11303-B1), Amicon® Ultra 0.5 centrifugal filter devices (UFC510096) were obtained from Millipore, SYBR® Green I Nucleic Acid Gel Stain was obtained from Lonza (50513), D-mannitol (Fisher BP686500) and 0.2 μm sterilized filter units from Corning.

### *4.2.2 Bacteriophage Culture and Labeling*

The bacteriophage culture was carried out in an assembly consisting of two conical flasks (50ml, Pyrex®) connected with rubber stoppers and glass tubes (O.D. = 3.12 mm). The first flask was used for culturing and the second one for trapping any overflow of the media and allowing passage of outgoing air. The flasks and tubes were wet-sterilized at 121˚C for 20 min., and rubber stoppers were dry-heat sterilized at 160˚C for 4 hr. After cooling, 30 ml of the sterilized nutrient peptone broth was added into the flask, incubated at 37˚C for 12 hr. The broth remained clear to confirm the sterility. The stock solutions (~ 3 ml) of *Bacteriophage* T4r and host bacterium *E. coli* B on a Tryptone Agar slant was obtained from Carolina Biological Supply Company (Burlington, NC). *Bacteriophage* T1 were obtained as pellets from ATCC (Manassas, VA) with the same *E. coli* B as host bacterium. About 15 ml of nutrient peptone broth medium (Fisher, Pittsburg, PA) was added to the bacterial agar slant and incubated at 37˚ C for 12 hr. The concentration of the bacteria was measured with a counting chamber (Hausser Scientific Partnership, Horsham, PA) and found to be ~$2.25 \times 10^9$ CFU/ml. Next, 0.1 ml of cultured *E.*

*coli* was used to inoculate 30 ml of sterile medium in the first flask and incubated for ~2 hr. at 37˚C for bacteria to reach mid logarithmic phase. 1 ml of high titer solution of *Bacteriophage* (phage) at a concentration of $1 \times 10^9$ pfu/mL was added into the host bacteria solution. The virus-host culture was periodically examined by checking the turbidity of the solution. Lysis of the bacteria in the medium began after an hour of incubation, as indicated by frothing in the solution. Turbidity of the solution decreased as the lysis progressed and eventually turned clear after 3 hr. The solution was filtered with a 0.2 μm filter from Fisher (Pittsburg, PA) to remove live bacteria or bacterial debris. The phage culture was stored in the refrigerator at 4˚C with chloroform to kill and to ensure that no live bacteria were in the solution, as suggested by the vendor.

The cultured bacteriophages were characterized with both microbiological and microscopic methods. Double layer agar (DLA) method was used to determine the titer of the phages (see Supporting Information Fig. S1). All culture broths and agar were sterilized at 121˚C for 20 min. Transmission electron microscope (TEM) images were taken with FEI CM 100 (Philips, Eindhoven, Holland) with an AMT digital capturing system to illustrate the size and shape of *Bacteriophage* T4r and *Bacteriophage* T1 (see Supporting Information Fig. S2). In TEM sample preparation, 5 μl of phage suspension and 5 μl of 2% uranyl acetate onto a 400-mesh copper grid coated with a carbon film. The droplet was partially dried after 45 secs and the grid was air-dried before measurements.

Washing and labeling were carried out by centrifugation using Amicon® Ultra 0.5 centrifugal filter devices (Millipore, Billerica, MA). Phage suspensions were also centrifuged and re-dispensed into lower volumes to make up the lost phages during removal of the medium and the following washing procedures. In general, 400 μl of phage solution was added in the filter device consisting of a detachable inner filter tube and a larger outer tube and the set was

placed in the centrifuge (Minispin® plus, Eppendorf, Hauppauge, NY) at 14,000 rpm for 5 min. The device was then separated, and the solution in the outer tube was discarded. The inner filter tube was flipped upside down and placed in a new outer tube. The set was centrifuged at 14,000 rpm for 10 min to spin down the concentrated phage solutions into the outer tube. 400 µl of Tris-EDTA (TE) buffer was then added to dilute the phage solution. The washing steps were repeated three times to remove the remains of the nutrient peptone media.

The phages were labeled with SYBR® Green I nucleic acid gel stain (Lonza, Rockland, ME). A commercial stock solution of 10,000X concentration in dimethylsulfoxide (DMSO) was thawed in dark at room temperature. A 500X working solution was prepared by diluting with TE buffer. For the optimal staining, 1 ml of the phage solution and 500 µl of the SYGR® green-I working solution were mixed at 80˚ C in dark conditions for 10 min. After which, the samples were allowed to cool down for 5 min. The excess dye was removed and washed three times with TE buffer using the above described centrifugal filter device. The labeled phages were dispensed in double deionized water (Barnstead Easypure II, Thermo Scientific Asheville, Pittsburg, PA) containing 280 mM D-mannitol (Fisher, Pittsburg, PA). The addition of mannitol was found necessary to enhance the efficiency of pDEP capture of virus particles [132, 133]. The final concentration of the phages for the normal DEP experiments was ~$5 \times 10^9$ pfu/mL except in some concentration-dependent experiments. All the solutions were filtered with 0.2µm filtration membrane and sterilized at 121˚C for 20 min.

Transmission electron microscope images of the *Bacteriophage* T4r and *Bacteriophage* T1 were taken by dropping 5 µl of phage suspension was added onto a 400-mesh copper grid together with 5 µl of 2% uranyl acetate for staining The droplet partially wicked off after 45 s

and the grid was air-dried. The grids were examined by TEM (FEI CM 100 Transmission electron microscope with AMT digital capturing system). (see Appendix Figure A.3, page 167)

For fluorescence labeling, phages were centrifuged to concentrate to make up for the lost phages during washing and removing the medium, using Amicon® Ultra 0.5 centrifugal filter devices (UFC510096). 400 µl of phage solution was added in the filter device and placed in the centrifuge (Minispin® plus, Eppendorf) at 14000 rpm for 5 min. The device was separated and the solution obtained in the tube was discarded. To obtain a concentrated solution of phage, the filter unit was replaced in the tube upside down and was centrifuged at 14000 rpm for 10 min. The solution was collected and washed three times in the similar way using Tris-EDTA (TE) buffer to remove all the remains of the nutrient peptone media. Labeling of phages was carried out using SYBR® Green I Nucleic Acid Gel Stain obtained from Lonza (50513). The commercial stock solution of 100X in DMSO was thawed in dark at the room temperature. A working solution of 500X was prepared by diluting with TE buffer. For optimal labeling, 1 mL of the phage solution and 500 µl of the SYGR® green-I working solution was mixed and heated at 80˚ C in the water bath in dark for 10 minutes. The samples were then allowed to cool for 5 min. To remove the excess dye, the solution was centrifuged with centrifugal filter devices and washed three times with TE buffer. The labeled phages were dispersed in an aqueous solution containing 280 mM D-mannitol (Fisher BP686500). The final concentration of the phages for the experiment was about ~$5 \times 10^9$ pfu/mL. All the solutions were with filtered with 0.2µm filters and sterilized at 121˚C for 20 min.

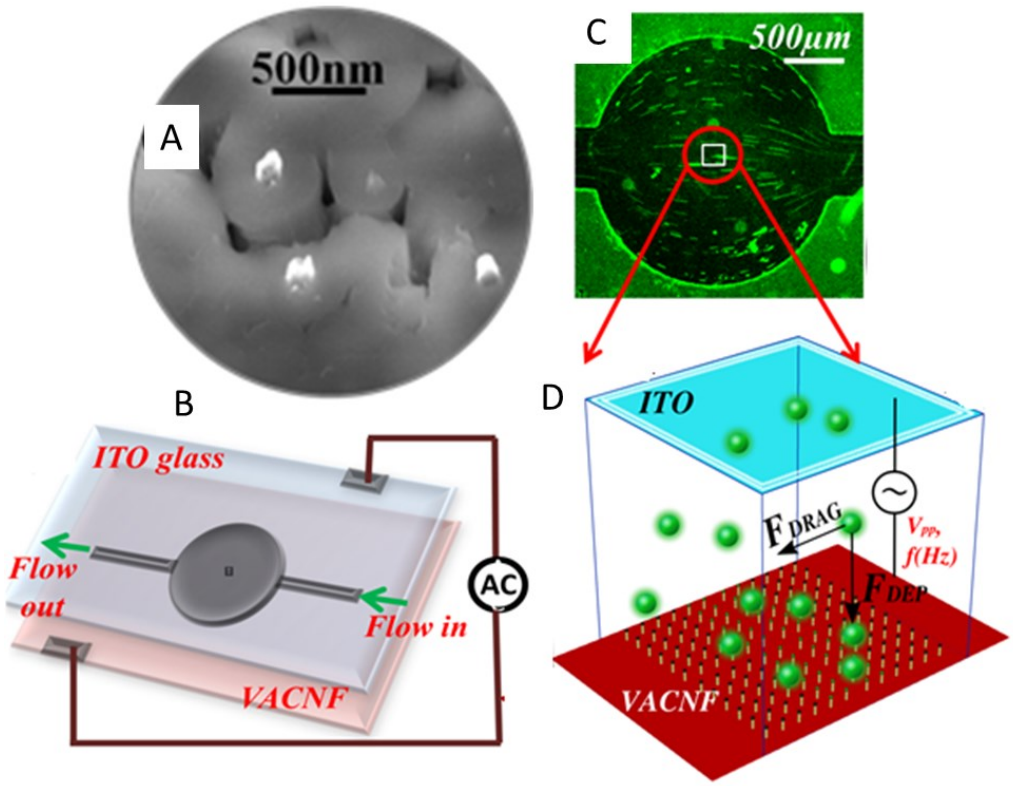


**Figure 4.1: Schematic representation of the device**

**(A) Scanning electron microscope image of the exposed tips CNF from the silicon dioxide bed. (B) Electrical connections made on the device that is connected to an AC function generator. (C) Optical microscope image was taken under 4X magnification showing that the channel is filled with labeled bacteriophage solution. (D) Schematic diagram of the active area of interest of 200 μm × 200 μm, showing the hydrodynamic drag force ($F_{DRAG}$) along the particle flow direction and the dielectrophoretic force ($F_{DEP}$) perpendicular to the flow direction solution captures facilitates in particle when the voltage is turned on. (Reprinted with permission from F. R. Madiyar, L. U. Syed, C. T. Culbertson, J. Li, *Electrophoresis,* 2013, 34, 1123-1130.)**

## 4.3 Experimental Considerations

### *4.3.1 Fluorescence Experiment Set-up*

The setup used for DEP-facilitated virus collection was similar to the earlier study on DEP capture of bacteria by Syed et al.[106] Briefly, the 200 μm × 200 μm active area on the microfluidic chip was focused 50X on an upright fluorescence optical microscope (Axioskop 2 FS plus; Carl Zeiss) shown in Figure 4.1. This microscope was equipped with Axio Cam MRm digital camera and filter set with the excitation wavelength of 485 - 520 nm and an emission wavelength of 515-565 nm (filter set 17, Carl Zeiss). The fluorescence videos were recorded at an exposure time of 0.5 s using multi-dimensional acquisition mode in the Axio-vision 4.7.1 release software (Carl Zeiss MicroImaging, Inc) for 95 sec. During this period, no voltage ($V_{off}$) was applied in the initial ~10 sec, fixed AC voltage at different frequencies was applied ($V_{on}$) for the next ~75 sec, and no voltage was applied ($V_{off}$) in the last ~10 sec. The movement of *Bacteriophage* T4r cells was visually monitored using a microscope at different frequencies (*f*) of the sinusoidal AC voltage, and at different flow velocities and concentrations of bacteriophage. The linear flow velocity within the focal depth from the NEA surface in the 200 μm × 200 μm area was calculated using the videos. Videos were analyzed using interactive measurement module in Axio Vision 4.7.1 release software (Carl Zeiss) to quantify the increase in intensity in the active region before and after capture.

### *4.3.2 Frequency Optimization*

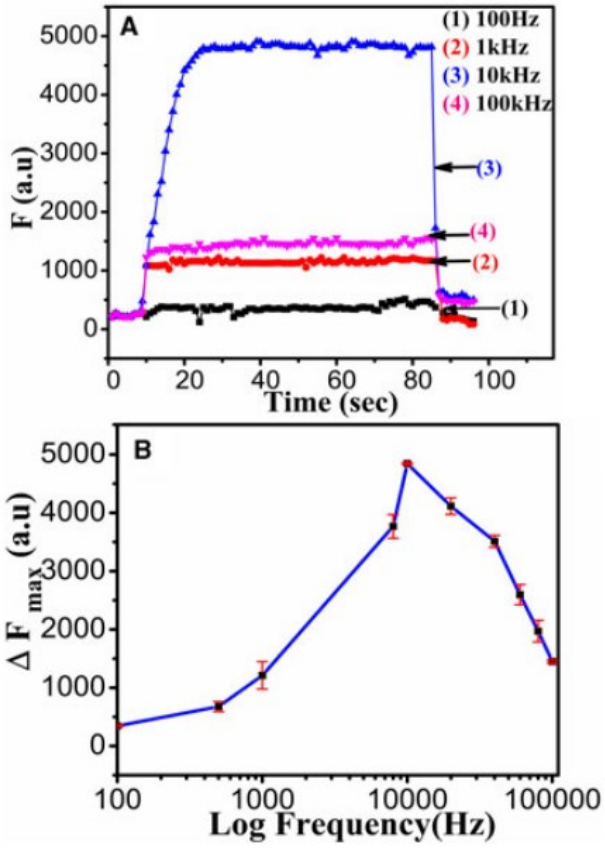


**Figure 4.2: Frequency-dependent capture of the bacteriophages.**

**(A) Kinetic study at different frequencies showing the variation in capture intensity with the frequency. (B) Maximum capture efficiency was observed at a frequency of 10 kHz, at the voltage of 100 $V_{pp}$ and a flow velocity of 0.73 mm/sec. (Reprinted with permission from F. R. Madiyar, L. U. Syed, C. T. Culbertson, J. Li, *Electrophoresis,* 2013, 34, 1123-1130.)**

The trapping of the *Bacteriophage* T4r was achieved using NEA in a microfluidic chip. It was not possible to observe a single bacteriophage at ~5 × $10^9$ pfu/mL, but the capture of the virus was fast indicated by rapidly increasing light haze on the NEA. Occasionally phages collected on top of each other causing the continual increase in the brightness as more viruses are

trapped with time. Hence, the fluorescence intensity, before and after capture used for the data analysis. Pseudo color is used to represent the fluorescence emission. The length of the DEP time was set to reach the saturation of the captured phages on the nanoelectrode. The positive DEP was observed in the frequency range from 1 kHz to 100 kHz at applied bias $V_{pp}$ of 10V shown in Figure 4.2 The highest capture was seen at 10 kHz and capture fluorescence intensity decreased as the frequency was increased further.

### *4.3.3 Voltage Optimization*

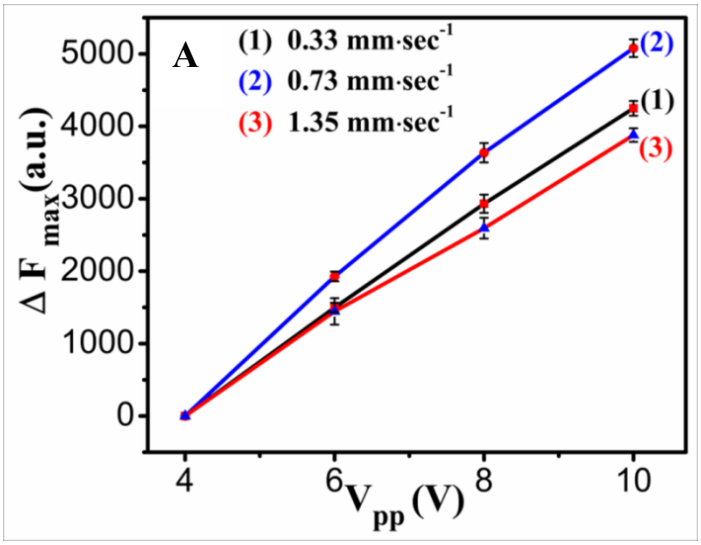


**Figure 4.3: Plot of ΔF and voltage**

**It shows that the linear increase in the capture of the bacteriophages with an increase in voltage. (Reprinted with permission from F. R. Madiyar, L. U. Syed, C. T. Culbertson, J. Li, *Electrophoresis,* 2013, 34, 1123-1130.)**

The high capture of the phage particles was seen at Vpp of 10V when the voltage was linearly increased from 2V to 10 V shown in Figure 4.3

### *4.3.3 Particle Velocity Optimization*

The flow velocity was gradually increased from 0.05 mm/sec to 3.0 mm/sec, the high capture of the phages was seen at 0.5mm/sec shown in Figure 4.4

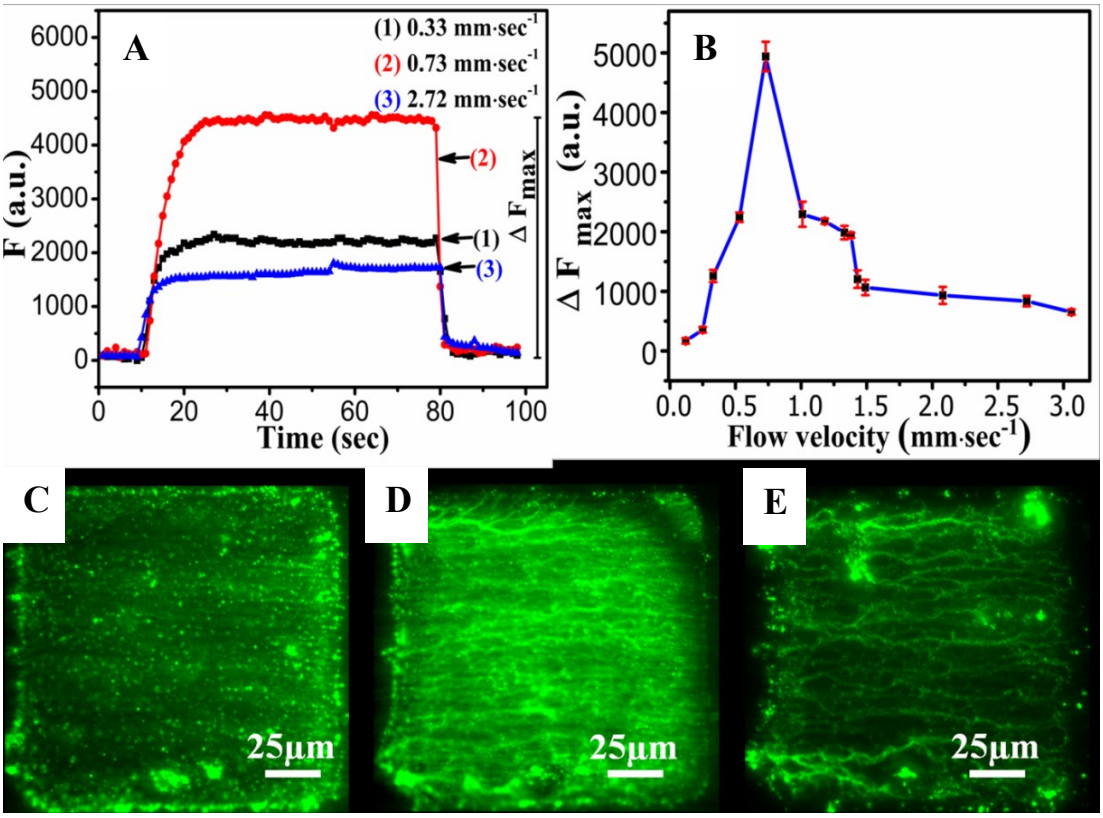


**Figure 4.4: Variation in the capture was seen at different flow velocities at frequency 10 kHz and voltage 10$V_{pp}$ AC bias.**

**(A) Kinetic study of different flow velocity. Fluorescence intensity is plotted versus the time showing the variation in capture intensity with flow rate. (B) The plot of difference in the fluorescence intensity at the lowest point versus the flow velocity, showing that the capture depends on the flow rate, and gradually decreases as the flow rate is increased. (C)-(E) are the snapshots at the highest capture at a flow velocity of 0.33, 0.73 and 2.72 mm/sec. (Reprinted with permission from F. R. Madiyar, L. U. Syed, C. T. Culbertson, J. Li, *Electrophoresis,* 2013, 34, 1123-1130.)**

### *4.3.5 Concentration Dependence of the Capture*

To determine the lowest concentration that can be captured at the optimum flow rate of

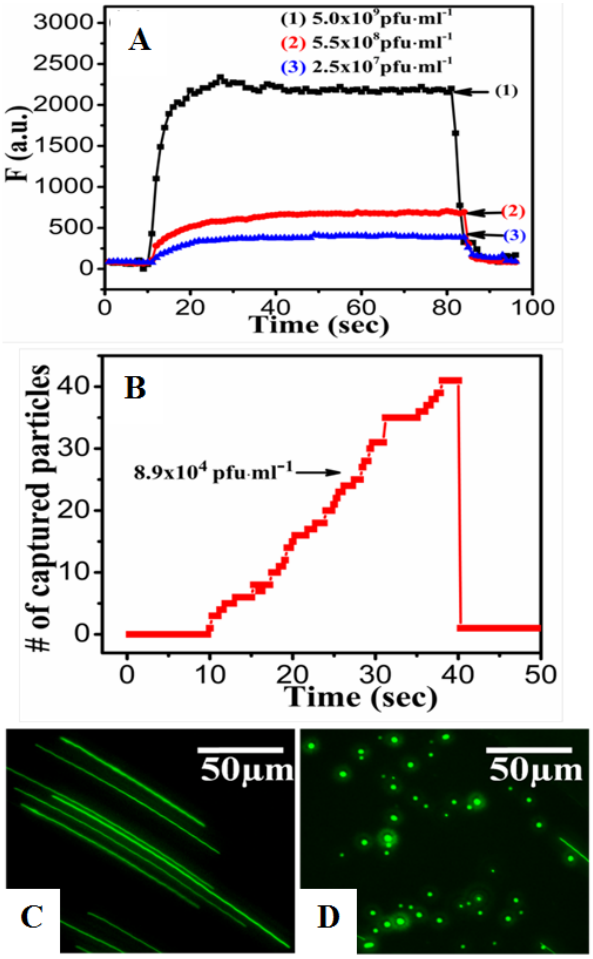


**Figure 4.5: Study of the kinetics of capture at different concentration keeping the frequency of 10 kHz and AC bias of 10 $V_{pp}$.**

**A plot is showing that the capture of the *Bacteriophage* T4r drops monotonically as the concentration was decreased. (B) Kinetic study of *Bacteriophage* T1 at the lowest concentration of 1 × $10^4$ pfu/mL showing isolated virus particles being captured at the exposed CNF. (Reprinted with permission from F. R. Madiyar, L. U. Syed, C. T. Culbertson, J. Li, Electrophoresis, 2013, 34, 1123-1130.)**

0.73 mm/s with frequency of 10 kHz and bias of 10V, the concentration of the virus was serially diluted with aqueous 280 mM D-mannitol solution shown in Figure 4.5

### *4.3.6 Capture pattern of Virus and Bacteria*

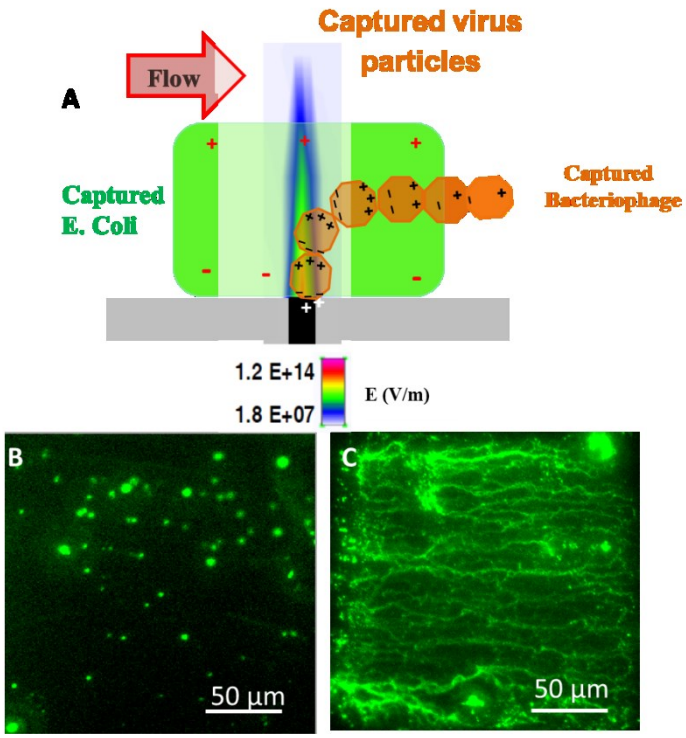


**Figure 4.6: Capture pattern of pathogens on VACNF**

**(A) Schematic diagram of the differences in the capture of the pathogens on VACNF where virus forms *Lichtenberg Figures* and bacteria. (Reprinted with permission from F. R. Madiyar, L. U. Syed, P. U. Arumugam and J. Li, in *Advances in Applied Nanotechnology for Agriculture*, eds. B. Park and M. Appell, American Chemical Society, Washington DC, 2013, vol. 1143, ch. 6, pp. 109-124)**

Different capture patterns between bacteria and bacteriophage virus were observed on VACNF shown Figure 4.6. From the modeling, simulation, and experimental studies, it is clear that there are differences between the DEP effects on bacteria and virus particles. The size of the

particle relative to the spatial distribution of the electrical field strength at the nanoelectrode tip is the main reason for different capture profiles.

It is noted that, in FEM simulation, the particles were assumed small compared to the scale of field non-uniformity and the inter-particle interaction was neglected. However, the electric field drops rapidly at the nanoelectrode (see Figure 4.6A), the particles cannot be treated as points and the electric field variation across the particle has to be taken into account. The strong polarization to smaller-sized virus particles is expected to greatly increase the inter-particle interaction. As a result, the captured virus particles may behave as extended nanoelectrode tips to capture other particles, forming chain-like lighting patterns shown in Figure 4.6C. In contrast, a relatively large bacterial cell screened the electric field at the NE tip, and limited capturing only one cell per NE site (see Figure 4.6B). These factors may also account for the discrepancies in the optimum AC frequencies for pDEP between calculated CM factors and experimental results. Refined FEM simulation and CM model is needed to develop precise understanding of the DEP processes at nanoscale.[134]

## 4.4 Discussion

The capture of the sub-micrometer particles have been already demonstrated on the planar electrodes which provide the electric field of $\nabla E^2=10^{17}V^2m^{-3}$ [135] to capture TMV virus,[136] herpes simplex virus.[137, 138] It has previously demonstrated by Syed. et al.[106] the capture of bacteria *E. coli* Dhα5 (~2 μm) by the positive DEP force on bacteria at a frequency of 100 kHz and applied $V_{pp}$ of 10 V on NEA microfluidic chip. This work is further taken forward by decreasing the particle size and demonstrating that NEA provides a sufficient electric field to capture the nanoscale particles using bacteriophages (200 nm). DEP force on the particle depends

on the radius of the particle ($\sim r^3$), which is decreased by 100 times if the particle size is decreased to the nanometer range. From Equation 2.3, DEP force also depends on the gradient of the square of the electric field, hence increase field will help to increase the DEP force on the particle and capture lead to the higher efficiency of capture.

The flow of the labeled *Bacteriophage* T4r was first examined at low magnification (with a 10X objective lens) as shown in Figure 4.1C. The streaks represent the movement of individual bacteriophage particles carried by the hydrodynamic flow of the media during the exposure time. The figure gives a good indication of the distribution of the particles as they enter the narrow straight channel (500 μm in width) into the larger circular microchamber (2 mm in diameter) and back into the narrow channel at the other side. Only a fraction of the bacteriophage particles passes above the active NEA area. It should be noted that the VACNF NEA in this study consists of randomly distributed CNF tips with an average spacing of >1 μm (as shown in Figure 4.1A), though such arrays can be fabricated into regular patterns using more expensive e-beam lithography processes.[139] Fluorescence videos of the labeled virus over the 200 μm × 200 μm active NEA area were recorded at higher magnification (with a 50X objective lens). At high capture density, it was difficult to distinguish individual bacteriophages. Thus the capture efficiency was first quantified using the increase in the integrated fluorescence intensity ($\Delta F$) over the 200 μm × 200 μm active NEA area during the kinetic DEP process after the AC voltage was applied.

Key factors affecting DEP capture include flow velocity, frequency, voltage, and concentration. As shown in Figure 4.4 A, the integrated fluorescence intensity rose to a saturation level ($\Delta F_{max}$) in less than 10 secs as a 10 $V_{pp}$ AC voltage was applied on the DEP device while a $5 \times 10^9$ pfu/mL *Bacteriophage* T4r solution was flowing through the channel at a

velocity (υ) varying from 0.085 to 3.06 mm/sec. Interestingly, a plot of the captured amount vs. the flow velocity showed a maximum at 0.73 mm/sec (see Fig. 4.3B). At $\upsilon \leq 0.73$ mm/sec, the maximum captured bacteriophage particles (as represented by $\Delta F_{max}$) approximately increased within a linear fashion, indicating that the capture process was limited by the mass transport. However, at $\upsilon \geq 0.73$ mm/sec, the captured amount decreased vs. υ, clearly due to a different mechanism.

When a virus particle is flowing in the microfluidic channel, the lateral hydrodynamic drag force, $F_{Drag}$ acting on the particle linearly increases with υ as shown in Equation 2.9. This drag force competes with the DEP force ($F_{DEP}$) to determine whether a virus particle will be captured at the NE point or continue flowing downstream. It is not surprising that fewer virus particles are retained at the active area of the NEA at the highest flow rates. It is noteworthy that the relative direction of $F_{DEP}$ vs. $F_{Drag}$ changes with the particle's position at the NEA, defined by the nonuniform distribution of $\nabla E^2$. As we described in the finite element modeling (FEM) simulation in a previous work [116], the DEP force is dominated by the vertical component (caused by $\nabla E_z^2$) when the particle is more than 3 μm above the NEA. At such distances, the particles are nearly orthogonal to the lateral $F_{Drag,}$ and this facilitates the downward deflection of the particles even at high υ. Once they come down at the NE points, a larger lateral DEP force (caused by $\nabla E_x^2$) will dominate, which cancels the lateral $F_{Drag}$ and leads to the capture of the virus particle at the NEA surface. As υ is increased beyond a certain threshold value, fewer particles are brought sufficiently close to the NE points so that they can be captured.

Interestingly, the captured virus particles showed very different patterns as a function of flow rate in the captured frames of the fluorescence video. At $\upsilon < 0.73$ mm/sec, isolated bright spots were seen, likely corresponding to individual virus particles (Figure 4.4 C). At $\upsilon \geq 0.73$

mm/sec, however, the captured frames showed fractal-like lightning patterns (Figure 4.4 D & Figure 4.4 E). These patterns are called *Lichtenberg figures* and are commonly generated under conditions where a high electric field is produced between a point and planar electrode separated by a dielectric containing charged or polarizable materials as is the case here. More discussion of the topic is given in Section 4.3.6 (Page 63). The generation of such patterns requires a relatively high concentration of polarizable particles and so is seen only when the particle flux is sufficiently high. Even though similar "pearl-chain-like" patterns were observed by Suehiro et al. in DEP trapping of *E. coli* cells between interdigitated microelectrodes[140], our previous DEP studies showed that only isolated *E. coli* cells were captured at the NE sites [106, 116]. The larger size and higher internal conductivity of bacteria may have screened the high electric field at the NE tip and reduced the electrical interaction with additional cells.

From Equation 2.4, the DEP force depends on the frequency of the AC bias through the complex CM factor. This force is associated with each bioparticle's structure and molecular composition and may be used to capture particular bioparticles at specific frequencies and to separate them from other types of bioparticles. Figure 4.2 shows the frequency dependence of DEP capture of *Bacteriophage* T4r from 100 Hz to 1 MHz, measured with fixed AC voltage (at 10 $V_{pp}$) and flow velocity (at 0.73 mm/sec). Similar kinetic curves were obtained at all frequencies after application of $V_{pp}$. The capture action was observed over a wide frequency range from ~500 Hz to 100 kHz with the maximum capture efficiency at about 10 kHz. This optimum frequency is much lower than 100 kHz to 1 MHz observed in previous studies with *E. coli* bacteria. Considering that mannitol had to be added to adjust the permittivity and conductivity of the media (i.e. water) [132, 133], it is clear that the small virus particles

(*Bacteriophage* T4r, 80-200 nm in size) have very different CM factor from much larger bacterial cells (*E. coli*, ~1-2 μm in size).

The magnitude of $\nabla E^2$ is another critical factor that depends on both the DEP device design and the amplitude of the applied AC voltage (represented by $V_{pp}$). As shown in Figure 4.3, the amount of captured *Bacteriophage* T4r particles linearly increased with the applied $V_{pp}$ at all three flow velocities. However, the DEP capture became unreliable at $V_{pp} < 6$ V and no capture was observed for the 75 secs after $V_{pp}$ was dropped to 4 V. This may be attributed to the fact that the DEP force is smaller than the combination of drag force and Brownian motions at low electric field strengths. To ensure the efficient capture, all other DEP experiments in this study were carried out with 10 $V_{pp}$.

The ultimate goal of this study is to develop a rapid sample preparation method for further identification of specific virus particles that can be integrated with other methods on a microfluidic device. Ultimately, the capture and analysis of single virus particles is desired. To assess this potential, a study of the concentration dependence of DEP capture was carried out first by diluting the normal $5 \times 10^9$ pfu/mL *Bacteriophage* T4r solution to $5.5 \times 10^8$ pfu/mL and then to $2.5 \times 10^7$ pfu/mL, respectively. As shown in Figure 4.5 A, the magnitude of $\Delta F$ during DEP capture monotonically decreases as the virus solution was diluted. The kinetics of DEP capture also became slower with dilution and $\Delta F$ was not able to reach a saturated level after about 75 secs of DEP period.

More interestingly, the DEP kinetics dramatically changed when a very dilute solution of *Bacteriophage* T1 ($8.7 \times 10^4$ pfu/mL) was passed through the DEP device. At such low concentrations, the DEP capture was found to be fully limited by mass transport. The capture of individual virus particles onto the NEA was observed as random single events and the number of

captured virus particles linearly increased with time over the ~30 secs timeframe (as shown in Figure 4.5 B). Similar results were obtained at various flow velocities from 0.59 to 0.94 mm/sec. The representative snapshot in Fig. 5c displays the streaks over the active NEA area when the AC voltage was off, indicating the distance that the phage particles moved at 0.87 mm/sec flow velocity in the 0.2 s exposure time. The longest streak was used to calculate the accurate flow velocity of the particles within the focus depth (~0.6 μm [106]) from the NEA surface. In contrast, the snapshot in Figure 4.5 D, shows focused isolated spots corresponding to the captured virus particles at exposed tips of CNF after the voltage was turned on for ~30 secs. The captured virus particles were clearly separated from each other and can be precisely counted. The calculation indicates that up to 60% of virus particles flowing through the active NEA area were captured at 0.87 mm/sec flow velocity. It is noted that the DEP device design in this study was focused on understanding of fundamental phenomena rather than achieving optimum capture efficiency. The capture efficiency can be significantly enhanced by fabricating elongated active NEA area across the full width of a straight microfluidic channel so that all virus particles are forced to pass through the strong electric field. Nevertheless, the reported results clearly demonstrate that, with proper design, the NEA based DEP device can capture virus particles at concentrations potentially approaching 1-10 CFU/mL. By coupling with highly sensitive detection methods (such as surface enhanced Raman spectroscopy), it is very promising to develop an ultrasensitive portable microfluidic system for rapid viral pathogen detection.

Comparing the above virus capture results to the previous reports on the DEP capture of *E. coli* cells with similar NEA devices [106, 116], four novel observations were made: (1) the optimum AC frequency was found to be ~10 kHz for virus as compared to 100 kHz to 1 MHz for *E. coli*. (2) The DEP capture of virus particles was observed even at ~$8.9 \times 10^4$ pfu/mL, more

than 4 orders of magnitude is lower than the concentration (~$1 \times 10^9$ CFU/mL) used in previous *E. coli* studies. (3) The capture efficiency was quantitatively assessed to be 60% from the reliable data at a low virus concentration (~$8.9 \times 10^4$ pfu/mL). (4) The formation of Lichtenberg figures by the captured virus particles after being captured at high flow velocities (≥ 0.73 mm/sec) with high virus concentration. The general capture efficiency of virus particles was found to be much higher than that for *E. coli* cells. This was quite surprising since the ratio of DEP force to drag force was expected to drop significantly as *E. coli* cells were replaced with ~10 times smaller virus particles. However, the observed higher DEP capture efficiency for smaller virus particles can be well explained with the highly focused electric field at the CNF NEA tip whose size is closer to that of virus particles than bacteria. As shown by the FEM simulation in our previous study [116], the magnitude of $E^2$ is highly focused at the nanoelectrode tip with an elongated distribution in a vertical direction like a spear. The magnitude of $E^2$ dropped quickly from ~$1.2 \times 10^{14}$ $V^2m^{-2}$ at the center of a disk-shaped nanoelectrode to ~$1.8 \times 10^7$ $V^2$ $m^{-2}$ at ~600 nm above [116]. $E^2$ dropped by the same magnitude in lateral direction only ~50 nm from the outside the edge of the nanoelectrode [116]. Such highly focused electric fields provide the extremely large magnitude of $\nabla E^2$ which generates the desired DEP force to capture bioparticles. However, it is only available within hundreds of nanometers from the nanoelectrode tip. This length scale is comparable to the size of the virus particles but much smaller than that of *E. coli* cells. As a result, the large $\nabla E^2$ likely interacts with entire virus particles but only affects small portions of *E. coli* cells. The DEP force relative to the particle volume thus was higher in virus than in bacteria. Further study with FEM simulation by incorporating the localized $E^2$ at the nanoelectrode is necessary to quantitatively assess the size dependence. Mathematical models may be applied in the future to determine the contour of $\nabla E_z^2$and $\nabla E_x^2$ near the capture region to

better understand how the vertical and lateral components of the field effect the capture of virus particles. These simulations will also be used to define the transition from "trapping zone" for Lichtenberg patterns and "capture zone" for the isolated spots pattern.[141]

## 4.5 Conclusion

In summary, it can be concluded that the high electric field gradient at the CNF NEA tip can generate strong DEP force to capture virus particles. It is more effective to capture virus particles than larger bacterial cells due to the comparable sizes of virus and CNF tip. Single virus particles can be observed as they are captured at isolated spots at the 200 × 200 $\mu m^2$ active NEA surface as a low concentration ($8.9 \times 10^4$ pfu/mL) was flowing by. At this condition, up to 60% of the total virus particles can be captured. At high concentrations ($\sim 1 \times 10^9$ pfu/mL), the DEP capture shows two possible mechanisms depending on the flow velocity. Isolated virus particles were observed at low flow velocities (< 0.73 mm/sec) while virus particles form *Lichtenberg figures* in the flow direction at high flow velocities (≥ 0.73 mm/sec). The DEP method with NEA can be used as a rapid microfluidic sample preparation module for further specific analyzes.

# Chapter 5 - Integration of Nanostructured Dielectrophoretic Device and Surface-Enhanced Raman Probe for Highly Sensitive Rapid Bacteria Detection‡

## 5.1 Introduction

### *5.1.1 Approaches to SERS Pathogen Detection*

Nanotechnology has thus been extensively explored due to the potential of developing miniaturized nanosensors with enhanced detection speed and sensitivity. In this work, we integrate two nanotechnologies into a portable system, i.e. (1) a nanoelectrode array (NEA) embedded in a fluidic chip for highly localized dielectrophoretic (DEP) capture/concentration of bacteria, and (2) a surface enhanced Raman spectroscopy (SERS) probe for specific bacteria identification. We demonstrated this method could be potentially developed into a highly sensitive portable system for rapid in-field pathogen detection.

SERS employs considerably enhanced electromagnetic fields in the vicinity (<10 nm) of a nanostructured metal substrate surface to interact with molecules adsorbed on the substrate surface.[142, 143] The Raman scattering intensity may be enhanced up to 14 to 15 orders of magnitude at certain hot spots.[144] Various SERS methods have been developed for the powerful non-destructive spectroscopic investigation of molecular structures.[142, 143] In addition, SERS can identify specific vibrational frequencies of the chemical functionalities in complex aqueous

‡ Reproduced in part by permission of the Royle Society of Chemistry, F. R. Madiyar, S. Bhana, L. Z. Swisher, C. T. Culbertson, X. Huang, J. Li, 'Integration of a nanostructured dielectrophoretic device and a surface-enhanced Raman probe for highly sensitive rapid bacteria detection' *Nanoscale*, 2015,7, 3726-3736.

biological samples with convenient visible and near infrared laser probes. There is an active interest in developing portable SERS systems for pathogen detection.[145, 146] There are two general approaches for SERS based pathogen detection as discussed below.[145]

#### *5.1.1.1 Direct Detection*

The first is direct detection of the intrinsic vibrational fingerprint of a pathogen by bringing them in proximity to a metallic nanostructure (e.g. colloidal nanoparticles,[65] nano-clusters,[147] sandwich structures of gold film and nanoparticles[148] and controlled nanostructured substrates[149]). Using this approach, in 1989, Holt et al. published the first SERS analysis of bacteria. They collected SERS data from a photosynthetic bacterium cell wall.[150] Since then, the method has gained the attention of research groups worldwide. Both qualitative and quantitative information on bacteria strains, subspecies and even complex biofilms have been reported as well as in vitro and in situ SERS detection of bacteria. The detection of *E. coli* using SERS has been published extensively in the last decade.

The latest publications in this area are promising for future implementation of SERS detection of the real sample microorganism analysis. Zeiri et al. (2004) have shown that if silver colloids are produced in the present of bacteria, these particles enter the inner of the cell and fingerprint spectra can be observed. They additionally reported that fingerprint spectra from the same bacteria species (here *E. coli*) varied with different laser excitation wavelengths.[151] Kahraman et al. (2007) compared two bacterium species with SERS with the motivation of revealing the dependence of the fingerprint spectra on the on the laser wavelength and SERS media metal on the fingerprint spectra.[152, 153] Wigginton et al. (2010) reported a membrane filter for the concentration of pathogens for SERS detection.[154] Premasari, et at. (2005) proposed a

novel barcode Raman data processing procedure that can distinguish in the solution different species of the bacteria stained with gold nanoparticles.[155, 156]

However, the direct identification of pathogens requires a highly controlled SERS substrate in combination with reproducible spectral data, as pathogen identification is accomplished by processing data using statistical algorithms that analyze minute differences in the Raman spectra. This turns out to be very challenging due to two factors: (1) the high dependence of SERS signal on the surface structure, size/shape of the nanostructured substrate, the excitation laser wavelength, and the configurations of pathogen binding on the nanostructure surface;[157, 158] and (2) the fast exponential decay of the electromagnetic field away from the nanostructure surface.[159] All these variables lead to a lack of consistency and poor reproducibility of the SERS measurements.

#### *5.1.1.2 Detection using Nanotags*

The second approach is an indirect detection method using a SERS nanotag as a quantitative reporter.[146] The SERS nanotag is a complex structure consisting of a nanoscale metallic substrate attached to a molecule with a strong, unique Raman fingerprint. The pre-fabricated nanotag complex ensures that the reporter molecules are in close contact with metal nano-substrates to give a high surface enhancement. In addition, the nanotags are co-functionalized with biorecognition molecules (such as antibodies, aptamers, etc.) which specifically bind to the pathogens. As a result, the high SERS signal is only obtained from the particular pathogen and not from other microorganisms. The precise identification of a pathogen can thus be achieved without relying on multivariate analysis. Several previous reports have demonstrated the use of 4-mercaptobenzoic acid[160], [5,5′-dithiobis(succinimidyl-2-nitrobenzoate)] (DSNB),[146, 161] tetramethylrhodamine isothiocyanate (TRITC) and QSY21 dye[162]

as effective Raman markers. Walter et al. (2011) published the detection of *E. coli* in a SERS flow-system.[163] They showed the qualitative evaluation of different subspecies by chemometrics. A database of multiple spectra was generated, and the results were gathered without the use of labeling molecules. Temur et al.[164] (2010) carried out a quantification of *E. coli* in the range of $10^1$ CFU/mL - $10^5$ CFU/mL by using gold nanoparticles coated with the label 5,5'-dithiobis-2-nitrobenzoic acid (DTNB) on a sandwich immunoassay.

#### *5.1.1.3 Detection of Microorganisms in Microfluidic Flow Environment*

The implementation of flow cells to SERS analysis became increasingly important in the past decade as the high sensitivity of the method matches the small volumes involved in the microfluidic analysis. It is known that a higher reproducibility can be achieved in flow systems than under static conditions due to the higher precision of the analyte dosage and better heat dissipation of flow systems. Berthod et al. (1987) reported one of the first experiments making use of flow-injection for SERS analysis for the determination of pigments in microorganisms.[165] Following the same idea, Strehle et al.[166] (2007) have developed a flow cell for the online SERS measurement of crystal violet. They were able to analyze separate sample volumes down to 60 nanoliter, underlining the potential of this approach in case of limited size. SERS detection of *Saccharomyces cerevisiae, Escherichia coli F-amp and Bacillus subtilis* for was obtained in a spectroscopic-microfluidic flow cell using silver nanoparticles as SERS media.[167] Considering all these works, it becomes obvious that the combination of SERS and microfluidic with immunoassay techniques offers the possibility to capture specific antigens selectively on well-defined spots in the flow cell. Earlier this idea was proven by Guven et al. (2011) in an SERS-based sandwich immunoassay using antibody-coated magnetic nanoparticles for *E. coli* with a limit of detection (LOD) of 8 CFU/mL.[168]

In this study, we focus on the specific detection of *E. coli* strain Dhα5 using the SERS reporter QSY21 that is co-functionalized with polyclonal antibodies on anisotropic oval-shaped iron oxide-gold (IO-Au) core-shell nanoparticles. The irregular shape and thickness of the Au shell provides a significant enhancement factor for SERS.[169, 170] In order to further lower the detection limit and simplify the sample preparation, the *E. coli* are concentrated by dielectrophoresis (DEP) into a 200 μm × 200 μm area inside a fluidic channel where the Raman laser beam is aligned and focused on NEA made of vertically aligned carbon nanofibers (VACNFs)[111] at the bottom of this area versus a macroscopic indium tin oxide (ITO) transparent electrode at the top form the DEP device in a "point-and-lid" geometry[171]. As we demonstrated before, a moderate AC voltage applied to the NEA, and the ITO electrode can adequately capture bacteria[106, 116] or viral particles[117, 134] due to the significantly enhanced electric field at the exposed VACNF tips. In the integrated system, we demonstrated the use of this fast, active and reversible concentration technique to bring bacteria into the field of view of a fixed Raman probe. Highly sensitive SERS detection has been demonstrated with both of a confocal Raman microscope and a portable Raman system as a very dilute bacteria solution is passed through the fluidic chip.

## 5.2 Experimental Details

### *5.2.1 Materials and Reagents*

Indium Tin Oxide (ITO) glass was purchased from Delta Technologies (Loveland, CO), SU-8 2010 and SU-8 2002 photoresist was purchased from Microchem (Newton, MA), conductive silver epoxy from MG Chemicals (Ontario), and microfluidic fittings from Upchurch Scientific Inc. (Oak Harbor, WA). QSY21 was purchased from Life Technologies (Grand Island,

NY, USA). Carboxypoly (ethylene)-thiol (HOOC-PEG-SH, MW 5000) and methoxy-PEG-thiol (mPEG-SH, MW 5000) were purchased from Laysan Bio Inc. (Arab, AL, USA). *E. coli* DHα5 were purchased from Life Technologies (18265-017, Grand Island NY, USA). FITC conjugated rabbit anti-*E. coli* Rabbit primary antibody was purchased from AbD Serotech, (Raleigh, NC, USA), and Alexa 555 conjugated goat anti-rabbit secondary antibody was purchased from Invitrogen (Carlsbad, CA, USA).[172]

### *5.2.2 Iron Oxide Nanoparticle Preparation with PEGs*

QSY21 adsorbed IO-Au NOVs was stabilized with HOOC-PEG-SH and mPEG-SH following the previously reported methods.[169] For ligand conjugation with Alexa 555 conjugated goat anti-rabbit (secondary antibody), 100 µL IO-Au NOV SERS nanotags, 3 mg 1-Ethyl-3-(3-dimethylaminopropyl) carbodiimide (EDC) and 3 mg sulfo- N-hydroxysuccinimide (sulfo-NHS) were added to pH 5.5 MES buffer to make solution volume to 500 µL. The mixture was vortexed for 15 min and spun down at 10,000 rpm for 10 min. The pellet was re-dispersed in 200 µL of 1 X Phosphate Buffered Saline (PBS, pH 7.4), followed by the addition of 20 µL of 0.2 mg/mL of the secondary antibody. The solution was vortexed for 2 h at room temperature to complete the coupling reaction, and then stored at 4˚C. Prior to use, the solution was centrifuged and washed with 1X PBS buffer 3 times to remove non-conjugated antibodies.

### *5.2.3 Conjugated Sample Preparation of Bacteria and Iron Oxide Nanoovals*

Frozen *E. coli* DHα 5 stock was thawed and grown in Luria-Bertani (LB) medium in a sterile culture tube and incubated overnight at 37˚ C to reach a cell concentration of $2.5 \times 10^9$ CFU/mL. The cells were centrifuged at 5000 rpm for 5 min, the supernatant LB media was discarded, the pellet was resuspended and washed in 1.0 mL 1X PBS thrice to eliminate the remaining ingredients of the LB media. A bacteria solution of $2.5 \times 10^9$ CFU/mL was incubated

with 50 µl FITC conjugated rabbit anti- E. coli Ab (AbD Serotech, Raleigh NC, USA) at 330 µg/mL for 1 h at 4˚ C. The cells were then centrifuged, washed with deionized (DI) water and diluted to a final concentration of $9.5 \times 10^4$ CFU/mL. The bacteria and antibody-conjugated IO-Au NOV SERS nanotag solutions were mixed at a ratio of $1.05 \times 10^5$ the NOVs to one bacterium. The solution was vortexed for 3 min and incubated overnight at 4˚C. To ensure that only bacteria-conjugated NOVs are spun down, the spin speed was kept low around 2000 rpm for 10 min and this process was repeated three times and finally the bacteria were suspended in DI water.

The NOV surfaces were then coated with a mixture of carboxy-polyethylene glycol-thiol (HOOC-PEG-SH, MW 5000) and methoxy-polyethylene glycol-thiol (mPEG-SH, MW 5000) in order to make NOVs biocompatible, stabilize the QSY21 adsorption, and to introduce carboxylic acid groups at the surface for covalent attachment of a Alexa 555-labelled secondary antibodies through amide bond formation. The *E. coli*-specific primary antibody (labeled with FITC for fluorescence validation) was then bound to the secondary antibody on IO-Au SERS NOVs to form the completed SERS nanotag. Before each experiment, these SERS nanotags were mixed with the bacteria sample to allow for the attachment of the nanotag to *E. coli* bacteria through specific immunochemistry. The structure of QSY21 and its typical Raman spectrum is shown at the center of Figure 5.1 Raman bands at 1333, 1584 and 1641 $cm^{-1}$ are from the xanthene ring stretching vibrations of the molecule. The strongest characteristic band is seen at 1496 $cm^{-1}$. The signal from the QSY21 attached to the NOV nanotag for this band demonstrates an enhancement factor of $4.9 \times 10^4$ over a 0.1 mM solution of QSY21[162] and thus is used in this study for the quantitative measurement. Figure 5.1 B and C show TEM images of IO-Au SERS NOVs and those bound onto *E. coli*. On average, there are hundreds of NOVs bound to each *E. coli*, which

gives a Raman signal sufficient to be detected at the single cell level. The confocal fluorescence microscopy image of Alexa 555 dye-labeled secondary antibody from the *E. coli* cells clearly illustrates the uniform coating of NOVs on *E. coli* DHα5 through specific immunochemical binding.

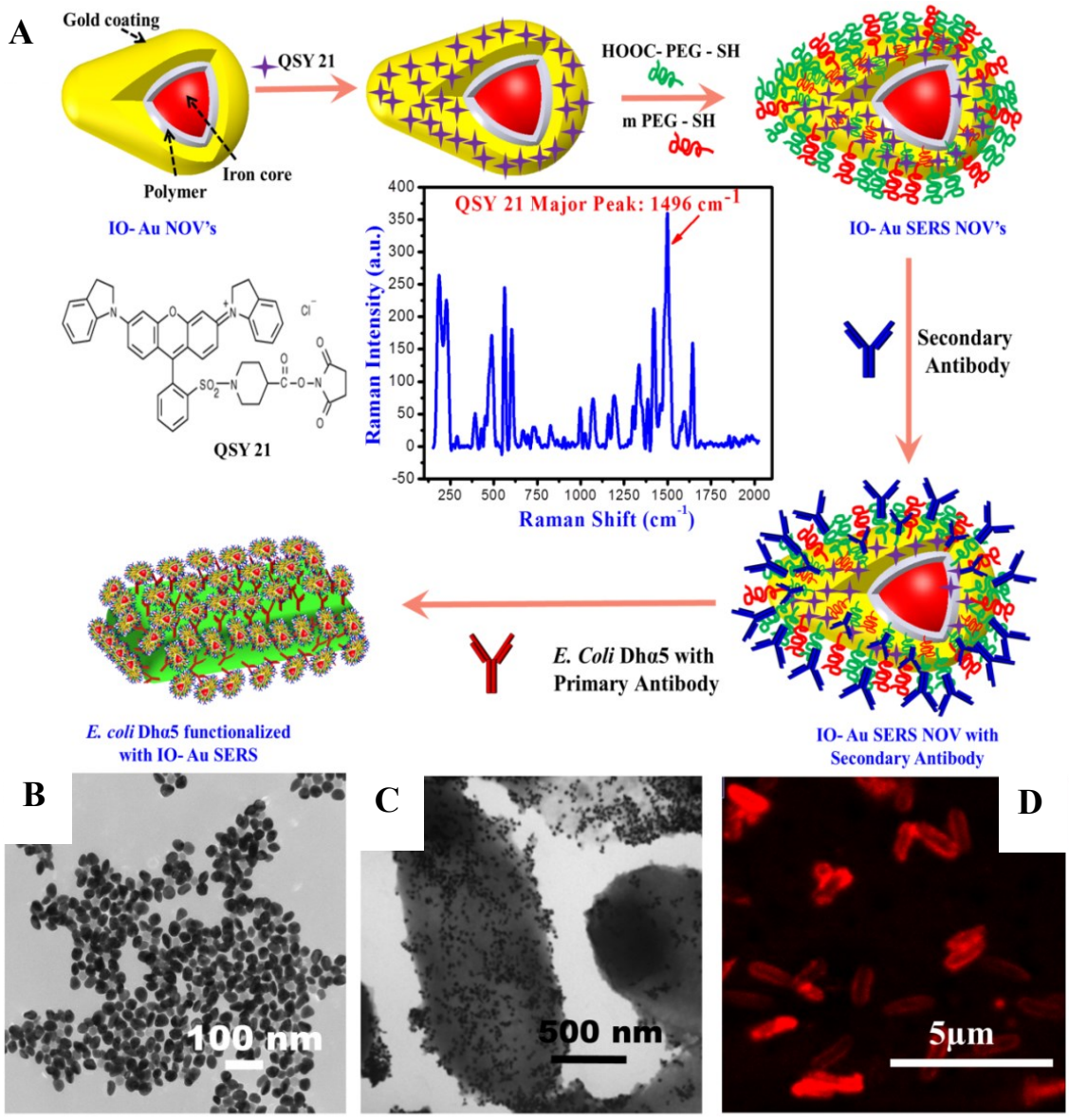


**Figure 5.1: Functionalisation procedure of nanoovals with QSY21 and antibodies**

**(A) Schematic procedures for preparation of QSY 21 derivatized iron oxide-gold core-shell nano-ovals (IO-Au NOVs) as nanotags for SERS measurements and their attachment to *E.***

***coli*** **bacterial cells through a FITC-labeled primary antibody and a Alexa 555 labeled secondary antibody. TEM images of (B) the starting IO-Au NOVs and (C) E. coli DHα5 bacterial cells attached with antibody-functionalized IO-Au NOVs. (D) Confocal fluorescence image of Alexa 555 in *E. coli* DHα5 bacterial cells attached with antibody-functionalized IO-Au NOVs. Alexa 555 was attached to the secondary antibody. (Reprinted with permission from F. R. Madiyar, S. Bhana, L. Z. Swisher, C. T. Culbertson, X. Huang, J. Li, *Nanoscale, 2015,* 7, 3726-3736.)**

### *5.2.4 TEM Characterization of Modified Nanoovals*

Transmission Electron Microscope (TEM) images of the NOVs and bacteria functionalized with the NOVs were taken by adding 5 μL of suspension to a 400-mesh copper grid and dried at room temperature overnight. The grids were examined by TEM (FEI CM 100 with AMT digital capturing system). Figure. 5.1 summarize the procedure to prepare the SERS nanotag nanoovals (NOVs) that bind to *E. coli* DHα 5. In brief, the NOVs were synthesized from spherical IO nanoparticle cores (~23 nm diameter) onto which an irregular-shaped Au shell was deposited, forming NOVs with the outer dimension of 35 to 50 nm to provide a large SERS enhancement factor.[169, 170]

## 5.3 Enhancement Factor Assessment

The SERS enhancement factor (SERS-EF) is one of the most important parameters that characterize the ability of a given substrate to enhance the Raman signal for SERS applications. The comparison of SERS intensities and SERS-EF values across different substrates is a common practice to unravel the performance of a given substrate.[173] The enhancement factors

from the different Raman Tag molecules are discussed in future works. Here, we consider the calculation of the Raman enhancement of QSY 21 only.

From Figure 5.2 we can see that the solution of 0.1 mM solution in water had no Raman signals but when attached to gold nanoparticles ( 60 nm diameter) or nanoovals evidently showed the increase in the fingerprint of Raman signal of QSY 21 is enhanced. We are interested in looking at 1496 cm $^{-1}$ peak because it is used for calculation of enhancement factor. We have assumed an average surface area of the sphere as compared to the surface area of the oval because the discrepancy in the shape of nanoovals. The enhancement factor we obtained from the nanoovals is denoted as > $3.51 \times 10^4$ because the bulk solution Raman intensity was as compared to the background is which about <8.361 cps.

**Table 5-1: Enhancement Factor Calculation of the QSY 21**

| Parameters | Explanation | Nano ovals (60nm) with QSY 21 |
|---|---|---|
| $Nbulk = Cbulk$ | # of molecules sampled in the bulk solution (0.1mM) | 0.1mM |
| $Nsers = DbCp4\pi r2$ | # of molecules sampled in Nano oval solution. $C_p$ =Particle concentration GNPs ($6 \times 10^{10}$/ml) $D_b$ is boding density 0.5 nmol /cm$^2$ | 3.39 $D_b$ is bonding density 0.5 n mol/cm$^2$ |
| I $_{Bulk}$ | Intensity of Bulk solution | <8.361 cps |
| I $_{SERS}$ | Intensity of Surface enhanced spectrum | 9956.10 cps |
| EF | Enhancement Factor | > $3.51 \times 10^4$ |

$$EF = \frac{9956.10}{8.361} \times \frac{0.01 \times 10^6 \left(\frac{nmol}{L}\right) \times \left(\frac{L}{1000mL}\right)}{0.5 \frac{nmol}{cm^2} \times 6 \times 10^{10} \frac{NPs}{mL} \times 4 \times 3.14 \times (4 \times 10^{-6})^2 cm^2}$$

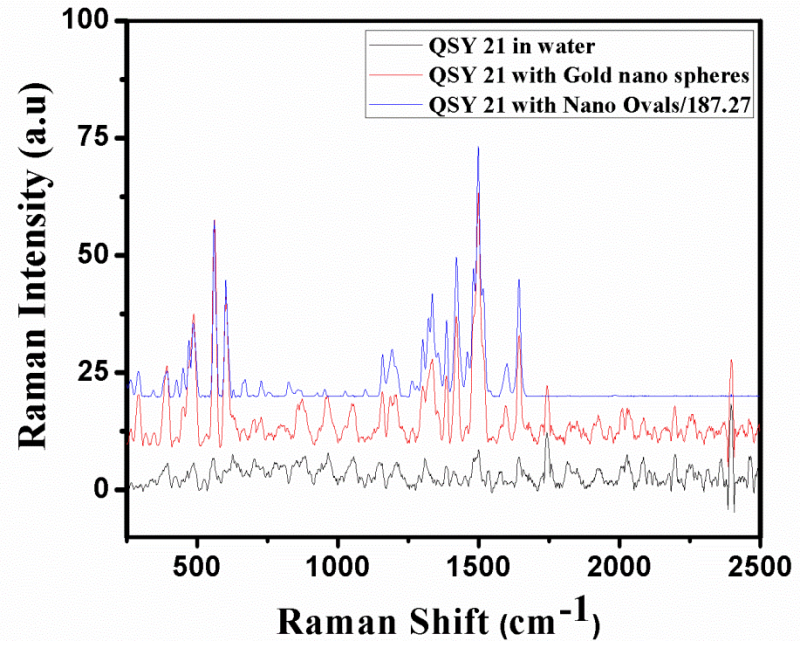


**Figure 5.2 Comparison of the Raman Intensities of QSY 21 in water (------ Black line), with 60 nm gold nanoparticles (---- Red line) and 60 nm nanoovals (---- Blue line).**

**(F. R Madiyar et al. unpublished work)**

## 5.4 Confocal Raman Spectrophotometer Experiments

### *5.4.1 Fluorescence- and Raman- DEP Experimental Set-up*

Fluorescence-DEP experiments were carried out on an upright fluorescence optical microscope (Axioskop 2 FS plus; Carl Zeiss) in reflection mode with 50 X objective focused at 200 µm × 200 µm active area. Labeled bacteria *E. coli* DHα5 conjugated to the NOVs suspended in D.I water was injected into the channel to carry out DEP experiments. A filter set for Alexa 555 with an excitation wavelength of 540-552 nm and emission wavelength of 567-647 nm (filter set 20HE, Carl Zeiss) was used in connection with an Axio Cam MRm digital camera to

record fluorescence videos at an exposure time of 0.7 s using a multi-dimensional acquisition mode in

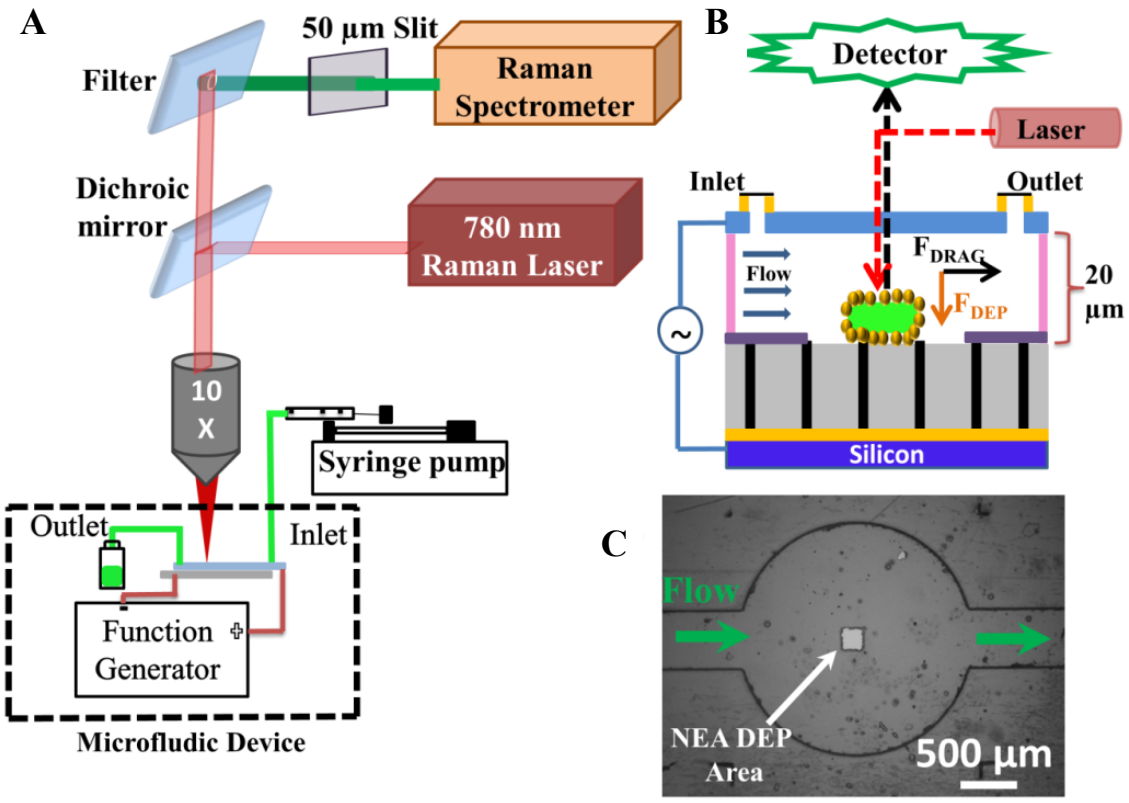


**Figure 5.3: Schematic of the microfluidic dielectrophoretic device under a Raman microscope for bacteria detection.**

**(A) The overall experimental setup of a confocal Raman microscope equipped with a 780 nm laser and a 10X objective lens. (B) Enlarged schematic view of DEP capture of the bacteria bind with oval-shaped SERS nanotags for the Raman detection with a portable Raman probe. (C) Optical microscope image was taken under 4X magnification showing the microfluidic channel and the active square at the center. (Reprinted with permission from F. R. Madiyar, S. Bhana, L. Z. Swisher, C. T. Culbertson, X. Huang, J. Li, *Nanoscale*, 2015, 7, 3726-3736.)**

The Axio-vision 4.7.1 release software (Carl Zeiss MicroImaging, Inc). An upright Thermo Scientific DXR™ confocal Raman microscope equipped with a 10 X objective (spot size of 3.1 μm) and 780 nm laser, with Omnic 8 software for data acquisition and analysis. The experiments required to tune the stage of the microscope for optimum focus. The VACNF in the microfluidc chip were taken as baseline to focus on the active area (shown in Appendix B.5, page 175). A full spectral range of 3500-50 $cm^{-1}$ with an accuracy of 5 $cm^{-1}$ was captured with a cooled CCD. Parameters were set at 5 mW laser power, 50 μm slit width, 1 s exposure time for all experiments.[172]

### *5.4.2 Frequency Optimization*

Each DEP experiment was performed in a span of 85 s during which no voltage ($V_{off}$) was applied in the initial ~10 s, followed with a fixed AC voltage at specific frequency in the next ~50 s ($V_{on}$), and then no voltage bias again ($V_{off}$) in the last ~25 s. Videos were recorded during each experiment. To perform the control experiments, the NOVs were conjugated with the secondary antibody (labelled with Alexa 555) and bacteria are conjugated with the primary antibody (labelled with FITC) were independently passed through the microfluidic channel. The results were monitored using the fluorescence microscope to determine the optimum frequency of the AC voltage. Fluorescence videos and Raman spectra were taken throughout the course of the experiment. Ten different spots from the active area were taken at each variable i.e. frequency, voltage, flow velocity, and concentration to ensure a proper statistical sampling. Background and the fluorescent light were subtracted using Omnic 8 software. In addition, the exact linear flow velocities within the focal depth of the microscope from NEA surface in the 200 μm × 200 μm active area were calculated from the recorded videos. To validate and

optimize the conditions, DEP capture was first monitored under a confocal Raman microscope at various frequencies.

### *5.4.3 Particle Velocity Optimization*

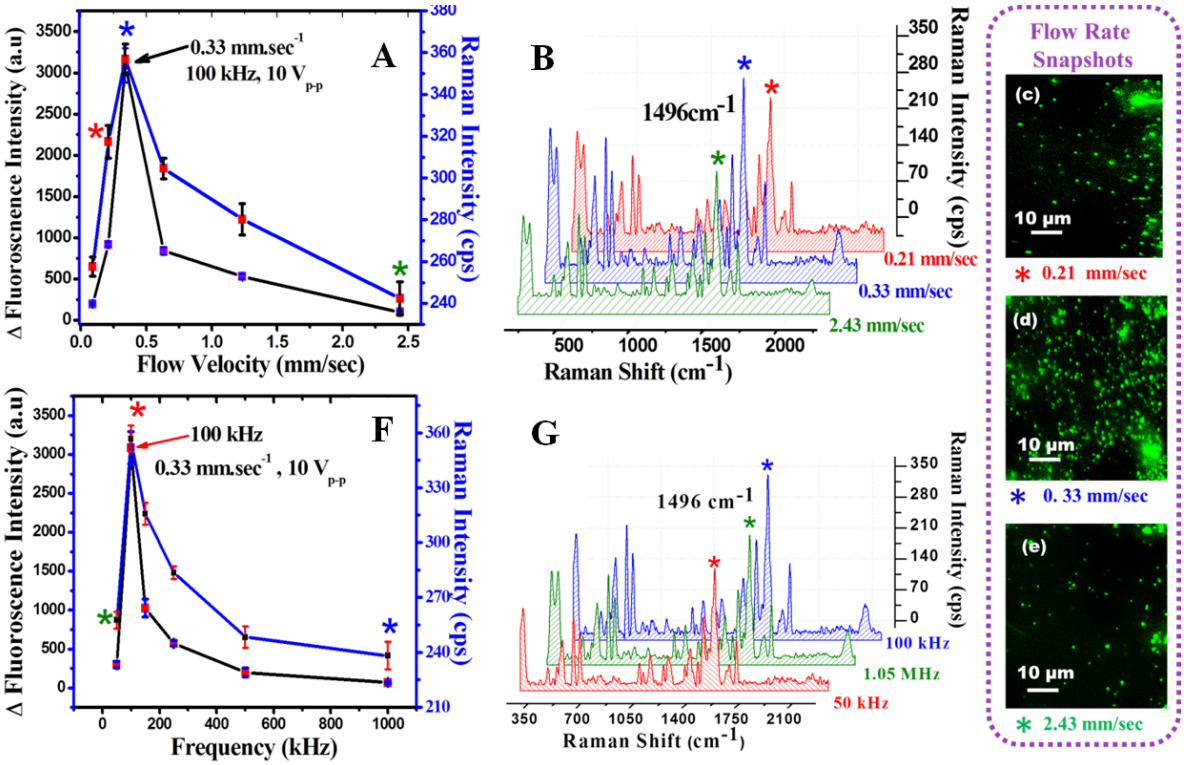


**Figure 5.4 Assessing DEP capture of 5.3 × $10^5$ CFU/mL *E. coli* cells with fluorescence and Raman measurements at various flow velocity and AC frequency.**

**(A) The study of flow velocity at fixed frequency (100 kHz) and voltage (10 $V_{pp}$). (B) Representative Raman spectra of QSY-21 and (C-E) corresponding snapshots from the fluorescence videos after 50 s of DEP capture of IO-Au NOV labeled *E. coli* cells at flow velocity of 0.21 mm/sec (red star), 0.33 mm/sec (blue star), and 2.43 mm/sec (green star). (F) The study of AC frequency at fixed flow velocity (0.33 mm/sec) and voltage (10 $V_{pp}$). (G) Representative Raman spectra of QSY-21 after 50 s of DEP capture of IO-Au NOV labeled *E. coli* cells at 50 kHz (green star), 100 kHz (red star), and 1,000 kHz (blue star).**

**(Reprinted with permission from F. R. Madiyar, S. Bhana, L. Z. Swisher, C. T. Culbertson, X. Huang, J. Li, *Nanoscale*, 2015, 7, 3726-3736.)**

The conditions were optimized for DEP capture under a confocal Raman microscope at various flow velocities. The pDEP capture experiments were carried out at flow velocities (ν) ranging from 0.11 to 2.43 mm/sec using a fixed AC voltage of 10 Vpp and frequency of 100 kHz. The number of captured bacteria initially increased with increasing flow rate until a maximum was reached at 0.33 mm/sec (corresponding to volume flow rate of 0.5 μl/s). Further increases in flow velocity resulted in a decrease in capture efficiency.[172]

### *5.4.4 Voltage Optimization and Real-Time Capture*

To determine the limit of detection by this system the concentration of the bacteria was changed from 10 to $1 \times 10^9$ CFU/mL and the kinetic curves of DEP capture at a low *E. coli* concentration of $5.4 \times 10^3$ CFU/mL were performed. Biological materials are very sensitive to the high electric field, and voltage study becomes necessary to determine the best condition for the capture of the bacteria without destroying the structure. In this study, the voltage was systematically changed from 3 V- 10 V.

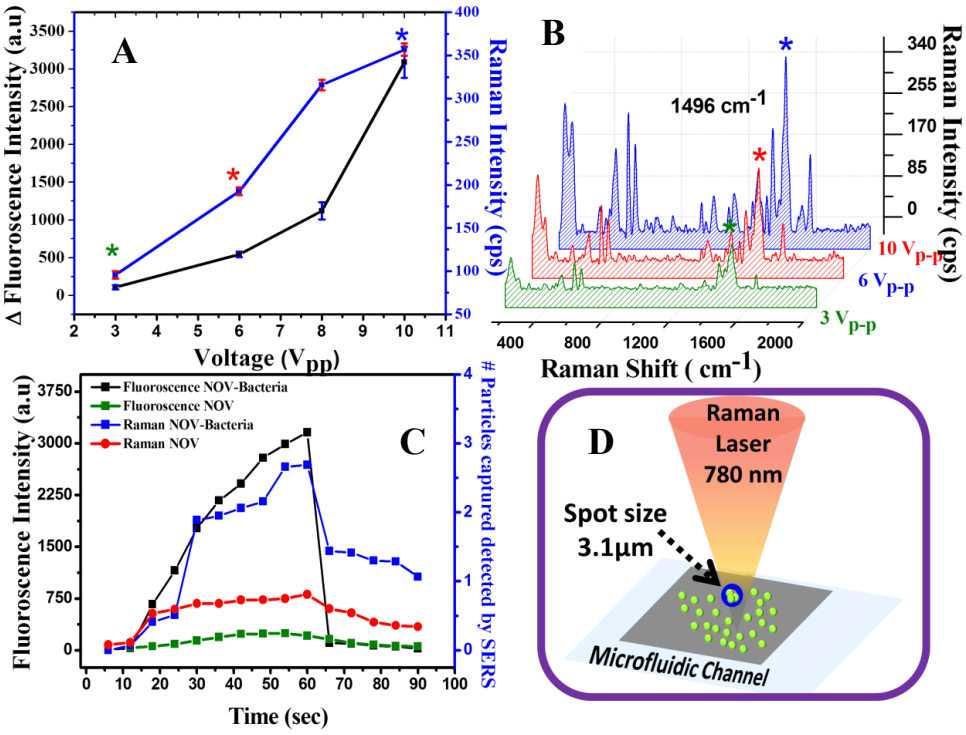


**Figure 5.5: Assessing DEP capture of 5.3 × $10^5$ CFU/mL *E. coli* cells with fluorescence and Raman measurements with varying voltage and time.**

**(A) The study of voltage at fixed flow velocity (0.33 mm/sec) and AC frequency (100 kHz). (B) Representative Raman spectra of QSY-21 after 50 s of DEP capture of IO-Au NOV labeled *E. coli* cells at 3 $V_{pp}$ (green star), 6 $V_{pp}$ (red star), and 10 $V_{pp}$ (blue star). (C) The kinetic curve during DEP capture of 4 × $10^3$ CFU/mL IO-Au NOV labeled *E. coli* cells. (D) Schematic diagram to illustrate the 3.1 μm laser focal spot size relative to the bacterial size). (Reprinted with permission from F. R. Madiyar, S. Bhana, L. Z. Swisher, C. T. Culbertson, X. Huang, J. Li, *Nanoscale*, 2015, 7, 3726-3736.)**

### *5.4.5 Assessment of DEP capture in Complex Matrix Samples*

Chicken broth, soil solution, and apple juice were used to test the viability of detecting bacteria in complex samples. Kroger chicken chunks in broth (141g, Cincinnati, OH) was

purchased from the local grocery store and the ingredient label indicated the presence of chicken chunks, water, less than 2 % of salt, modified corn starch and sodium phosphate. The soil sample was obtained from the lawn near Chemistry Department on Kansas State University campus and was soaked 50 mL of DI water overnight. About 2 g chicken chunks and 5 g solid soil were washed by DI water and vortexed for 2 min for four times and finally resuspended in 50 mL DI water. Mott's 100 % Apple juice (8 oz. Plano, TX) was obtained from the local grocery store, and the ingredients include water, concentrated apple juice, and ascorbic acid. 5 mL of apple juice (as purchased) was diluted to 10 mL with DI water to make the stock solution. Before spiking the solutions with *E.coli* cells, the solutions were centrifuged at 14,000 rpm for 10 min and the supernatant was passed through 0.22 μm sterile syringe filters (EMD Millipore, Billerica, MA). After processing, the solutions were cloudy indicating that the samples were not completely cleared from the matrix and used for pH and conductivity measurements. *E.coli* DHα5 was added to these solutions to a concentration of $5 \times 10^5$ CFU/mL. The conductivity of the solutions before and after addition of the bacteria was noted.[172]

## 5.5 Portable Raman- DEP Experiments

### *5.5.1 Portable Raman- DEP Experimental Set-up*

The second system was a portable Raman system (Pro Raman L, Enwave Optronics. Inc.) with a CCD detector cooled to -60ºC with spectral range from 3,300 $cm^{-1}$ to 100 $cm^{-1}$ shown in Figure 5.7 Parameters including 325 mW laser power, 1 s exposure time and 100 μm probe diameter at focus were fixed for all experiments. A function generator (Model 33120A, Hewlett-Packard, Palo Alto, CA, USA) was used to generate different frequencies (f) of the sinusoidal

AC voltage. A syringe pump (NE-1000) from New Era Pump Systems (Farmingdale, NY, USA) was used to produce various flow velocities.

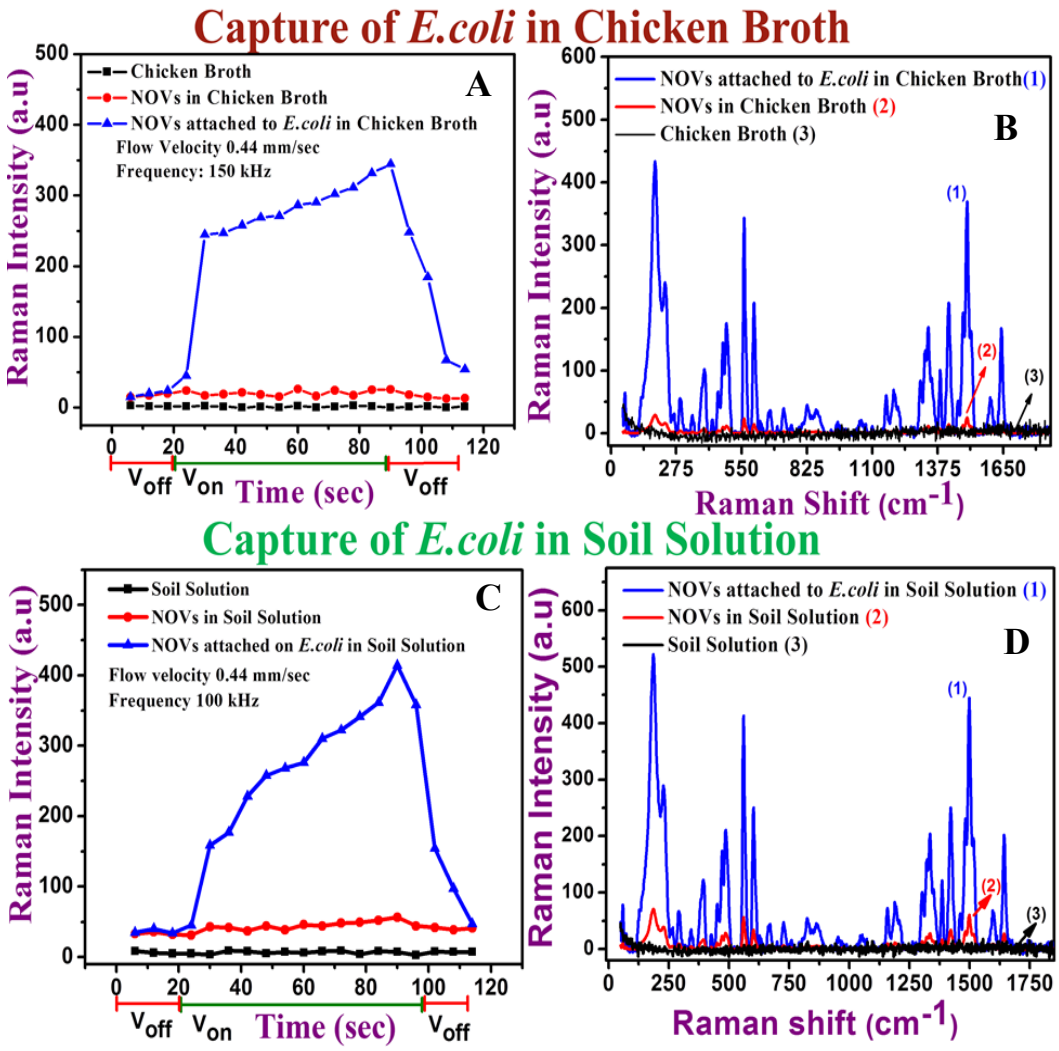


**Figure 5.6: Assessing DEP capture of *E. coli* cells with fluorescence and Raman measurements in different complex matrices.**

**(A) The kinetic curve of DEP capture of *E. coli* cells in a chicken broth at 10 Vpp, 0.44 mm/sec flow velocity, and 150 kHz AC frequency. (B) Representative Raman spectra of QSY-21 in the chicken broth after 50 s of DEP capture of IO-Au NOV labeled *E. coli* cells. (C) The kinetic curve of DEP capture of *E. coli* cells in a soil solution at 10 Vpp, 0.44**

**mm/sec flow velocity, and 150 kHz AC frequency. (D) Representative Raman spectra of QSY-21 in soil solution after 50 s of DEP capture of IO-Au NOV labeled *E. coli* cells. The measurements from a blank matrix, NOV spiked matrix ($1.4 \times 10^{10}$ NOVs/ mL), and NOV-bacteria spiked matrix ($5 \times 10^5$ CFU/mL) were presented in each panel. (Reprinted with permission from F. R. Madiyar, S. Bhana, L. Z. Swisher, C. T. Culbertson, X. Huang, J. Li, *Nanoscale*, 2015, 7, 3726-3736.)**

### *5.5.2 Frequency and Flow Velocity Optimization*

To demonstrate the potential capability of this method for use in a portable system, similar studies including flow velocity and frequency optimization were carried out with a portable Raman instrument (ProRaman L, Enwave Optronics. Inc.) in a manner analogous to the earlier studies using the confocal Raman microscope.

The results between these two Raman systems were very consistent, with the maximum flow velocity at 0.4 mm/sec (0.55 μl/s) and the maximum frequency of 100 kHz (see Figure. Appendix B.2 A and B, for confocal Raman microscope results, page 172). However, the probe diameter at the focal point in the portable Raman system is about 100 μm (Figure Appendix B.3, A and B is the portable Raman microscope results and Appendix B.3: figure C is a schematic of the 100 μm probe focused on DEP capture area, page 173), which is much larger than the 3.1 μm size in the confocal Raman microscope (Figure 5.5D). This allows signals to be collected from many more bacteria and yields better statistics, but the laser intensity is lower as it is spread over a larger area. These two factors need to be balanced for the optimum performance. DEP capture kinetic curves over longer time (~250 s) at higher concentration ($5 \times 10^6$ CFU/mL) show a

similar nearly linear increase in fluorescence and Raman signals over DEP time (see Figure Appendix B.4, page 174).

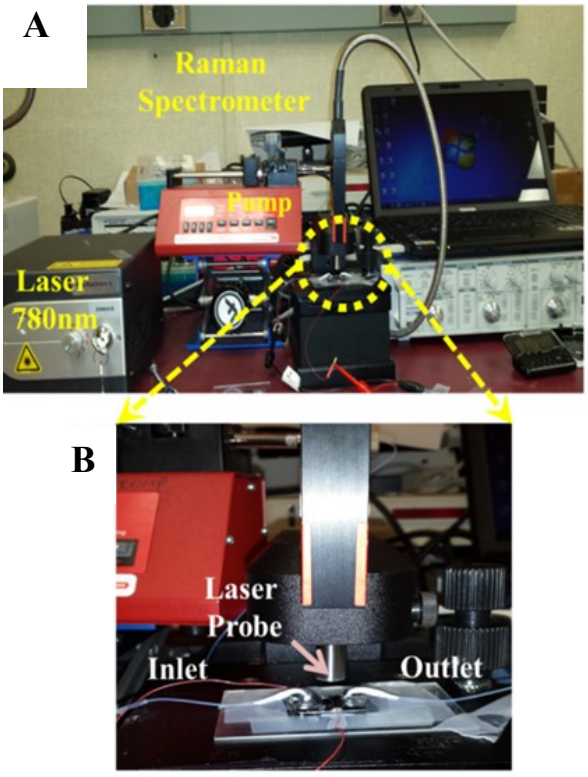


**Figure 5.7: Portable Raman Spectrophotometer**

**(A) The portable Raman Instrument (Pro Raman L, Enwave Optronics Inc.) and (B) the alignment of the microfluidic device under 100 µm probe. (Reprinted with permission from F. R. Madiyar, S. Bhana, L. Z. Swisher, C. T. Culbertson, X. Huang, J. Li, *Nanoscale*, 2015, 7, 3726-3736.)**

## 5.6 Discussion

### *5.6.1 Assessing the Attachment of the Nanoovals to Bacteria*

Figure 5.1 summarizes the procedure to prepare the SERS nanotag nano-ovals (NOVs) that bind to *E. coli* DHα 5. In brief, the NOVs were synthesized from spherical IO nanoparticle cores (~23 nm diameter) onto which an irregular-shaped Au shell was deposited, forming NOVs with the outer dimension of 35 to 50 nm to provide a large SERS enhancement factor.[169, 170] The NOV surfaces were then coated with a mixture of carboxy-polyethylene glycol-thiol (HOOC-PEG-SH, MW 5000) and methoxy-polyethylene glycol-thiol (mPEG-SH, MW 5000) in order to make NOVs biocompatible, stabilize the QSY21 adsorption, and to introduce carboxylic acid groups at the surface for covalent attachment of a Alexa 555-labelled secondary antibodies through amide bond formation. The *E. coli*-specific primary antibody (labeled with FITC for fluorescence validation) was then bound to the secondary antibody on IO-Au SERS NOVs to form the completed SERS nanotag. Before each experiment, these SERS nanotags were mixed with the bacteria sample to allow for the attachment of the nanotag to *E. coli* bacteria through specific immunochemistry. The structure of QSY21 and its typical Raman spectrum is shown at the center of Figure 5.1. Raman bands at 1333, 1584 and 1641 $cm^{-1}$ are from the xanthene ring stretching vibrations of the molecule.[174] The strongest characteristic band is seen at 1496 $cm^{-1}$.

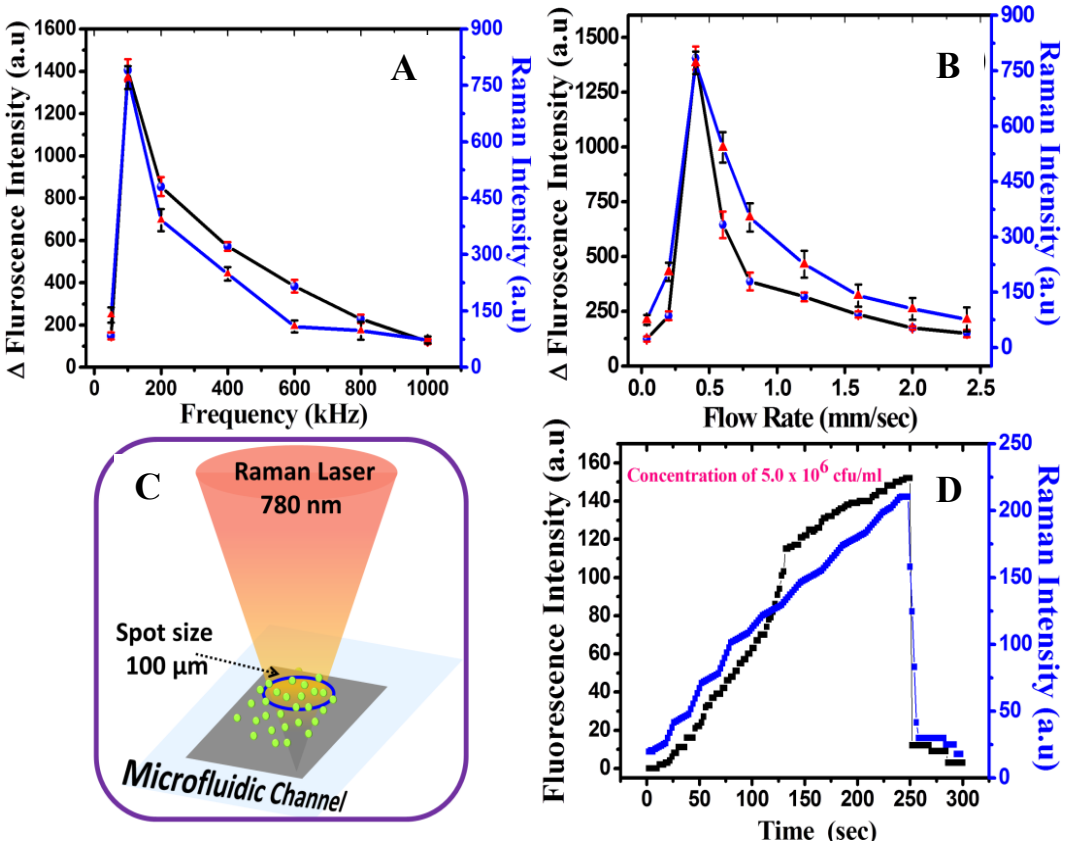


**Figure 5.8: Assessing DEP capture of 5.3 × $10^5$ CFU/mL of IO-Au NOV labeled *E. coli* DHα5 cells with fluorescence and the portable Raman system**

**(A) at varying AC frequency and (B) at varying flow velocity. The optimum frequency of 100 kHz and optimum flow velocity of 0.40 mm/sec were observed. (C) Schematic diagram of 100 µm diameter laser probe focused on the active DEP area of the microfluidic device. (D) The kinetic DEP capture curves measured at an AC frequency of 100 kHz and a voltage of 10 $V_{pp}$ while 5 × $10^6$ CFU/mL IO-Au NOV labeled *E. coli* DHα5 cells flowing through the DEP device at 0.40 mm/sec flow velocity. (Reprinted with permission from F. R. Madiyar, S. Bhana, L. Z. Swisher, C. T. Culbertson, X. Huang, J. Li, *Nanoscale*, 2015, 7, 3726-3736.)**

The signal from the QSY21 attached to the NOV nanotag for this band demonstrates an enhancement factor of $4.9 \times 10^4$ over a 0.1 mM solution of QSY21[162] and thus is used in this study for the quantitative measurement. Figures 5.1B and 5.1C show TEM images of IO-Au SERS NOVs and those bound onto *E. coli*. On average, there are hundreds of NOVs bound to each *E. coli*, which gives a Raman signal sufficient to be detected at the single cell level. The confocal fluorescence microscopy image of Alexa 555 dye-labeled secondary antibody from the *E. coli* cells (Figure 5.1D) clearly illustrates the uniform coating of NOVs on *E. coli* DHα5 through specific immunochemical binding.

### *5.6.2 Assessment of Raman Detection and DEP Optimization*

To validate and optimize the conditions, DEP capture was first monitored under a confocal Raman microscope at various flow velocities (Figure 5.4 A) and AC voltage frequencies (Figure 5.4 F). The results were compared side-by-side with the video of Alex 555 (in the functionalized secondary antibody) under a fluorescence microscope following our previously established method.[106, 117] The Raman intensity is the signal at the Raman shift of 1496 $cm^{-1}$ corresponding to the peak of the QSY21 reporter. Figure 5.4 B and Figure 5.4 G are representative Raman spectra of QSY21 at different flow velocities and AC frequencies. The representative snapshots from a fluorescence video during DEP capture of the NOV-bound bacteria within the 200 μm × 200 μm active NEA area are shown in Figure 5.4C to E.

Similar to our previous report on *E. coli* capture[27], the AC voltage $V_{pp}$ was turned on for 50 s while the bacteria/IO-Au NOVs solution was passed through the channel. The bacteria were collected at randomly distributed VACNF tips that have the highest $\nabla E^2$. Both the fluorescence and SERS signals associated with the captured bacteria were found to increase nearly linearly with time. The difference between the integrated fluorescence intensity ($\Delta F$) at the end of the 50

s capture period with that right before application of the capture voltage was used to quantitatively determine the DEP capture efficiency. The pDEP capture experiments were carried out at flow velocities (*v)* ranging from 0.11 to 2.43 mm/sec using a fixed AC voltage of 10 $V_{pp}$ and frequency of 100 kHz. The number of captured bacteria initially increased with increasing flow rate until a maximum was reached at 0.33 mm/sec (corresponding to the volumetric flow rate of 0.5 μL/s). Further increases in flow velocity resulted in a decrease in capture efficiency. The trend agrees well with our previous study.[27] An image of the final video frame taken for the capture efficiency experiment using the 0.33 mm/sec flow rate is shown in Figure 5.4D. The bright spots represent single captured bacterium. Raman intensity follows the same trend as the fluorescence measurements. At $v \geq 0.33$ mm/sec (Figure 5.4A), the number of captured *E. coli* DHα5 cells decreased because fewer cells can sustain the higher drag force of the fluidic flow. Only a small number of cells retain captured.

Because of the dependence of $F_{DEP}$ (Equation 2.4 and Equation 2.5) of the permittivity of a particle, each type of bio-particle has an optimum DEP frequency depending on its internal composition and structure. As shown in Figure 5.4F, both fluorescence and SERS intensity indicate optimum DEP capture of the NOV-labelled *E. coli* DHα5 cells at ~100 kHz with fixed peak-to-peak voltage of 10 $V_{pp}$ and a flow velocity of 0.33 mm/sec. The optimum frequency was the same as that for bare *E. coli* DHα5 cells[106], indicating that the attachment of IO-Au NOVs on the bacteria surface did not alter their overall DEP properties. In contrast, in Figure Appendix B.1 (page 171), shows that the NOVs alone were not captured via DEP forces at ~100 kHz. Rather they were obtained weakly at an optimum frequency of 10 kHz. The possibility that the measured SERS signal was from free NOV nanotags, therefore, was excluded. Combining these

observations, it is clear that SERS detection with NOV nanotags is viable and highly sensitive for monitoring the DEP capture of labeled *E. coli* DHα5 cells.

The magnitude of $\nabla E^2$ depends on both of the DEP device design and the amplitude of the applied AC voltage. Low voltage capture is preferred for bioparticles to prevent potential cellular damage. Figure 5.5A shows results with the voltage varying between 3 to 10 $V_{pp}$ while other parameters were fixed at the optimized conditions, i.e. flow velocity of 0.33 mm/sec and frequency of 100 kHz. The DEP capture indicated by SERS and fluorescence signals increased monotonically with the voltage and showed strong capture at 10 $V_{pp.}$ However, a large SERS signal was observed even at 6 $V_{pp}$ (Figure 5.5B and C).

Figure 5.5C shows the kinetic curves of DEP capture at a low *E. coli* concentration of 5.4 $\times 10^3$ CFU/mL. Both of the fluorescence and SERS signals slowly increase after the voltage was turned on since the number of available bacteria was limited by the mass transport. The bacteria were immediately released when the AC voltage was turned off. Thus, the device can be repeatedly used. The kinetic curve based on the SERS signal was further converted into the number of captured *E. coli* cells by dividing the measured SERS intensity by the average SERS intensity from a single NOV-labelled *E. coli* cell that was measured in a separate quartz cell counting chamber. The Raman intensity of the individual bacterium was measured using a *Petroff-Hausser* counting chamber made of quartz. The bacteria sample was diluted so that the individual bacterium was far apart and fixed in position. The excitation laser was focused on the cells one by one for confocal Raman measurements. The obtained average Raman intensity of an individual bacterium was 32.5 ± 4.6 a.u., showing a small variation due to the random fluctuation in the number of attached IO-Au NOV nanotags. The Raman kinetic curve showed a nearly step-wise increase as single *E. coli* cells were captured. As illustrated in Figure 5.5D, the small

size of the laser spot (3.1 μm in diameter) likely limited the maximum number of measurable bacteria to only ~4 within this spot. Clearly, a single *E. coli* cell can be easily detected with this device as long as they can be brought under the laser probe.

### *5.6.3 Assessment of DEP capture in complex matrix samples*

In order to demonstrate the capability of the DEP capture and SERS detection of bacterial cells in complex samples, *E. coli* cells were spiked with chicken broth, apple juice and soil solution for testing. Complex matrices present different challenges due to the presence of inorganic and organic substance that may interact with the bacterial cells, antibodies, or SERS nanotags, making it different from the pure bacteria solutions. Additional preparation procedures including washing, centrifugation and filtration (with 0.22 μm membrane) of the complex samples were applied before they were spiked with $5 \times 10^5$ CFU/mL *E. coli* cells. These commonly used sample preparation procedures are necessary to eliminate larger particles that can clog the microchannels. The conductivity of bacteria in distilled water (pH 6.8) was $1.22 \times 10^{-4}$ S/m. The conductivity of the commercial chicken broth (pH 7.22) was 0.45 S/m. The presence of salt in the chicken broth caused the high conductivity but was mostly removed during sample preparation. After the sample processing procedures, *E. coli* DHα5 cells were added and resulted in a conductivity of $1.7 \times 10^{-3}$ S/m (pH = 7.13). The soil solution (pH = 4.58) had a conductivity of 0.027 S/m in the raw sample, which dropped to $2.35 \times 10^{-4}$ S/m (pH = 6.8) after the preparation and *E. coli* spiking. For the apple juice, the conductivity was 0.155 S/m in the raw sample (pH = 2.95) and became 0.158 S/m (pH = 2.81) after the sample preparation and addition of *E. coli* cells.

Figure 5.6 shows the real-time Raman measurements during DEP capture of $5 \times 10^5$ CFU/mL *E. coli* DHα5 cells spiked in the complex matrices at the frequency of 150 kHz and the

flow velocity of 0.44 mm/sec. To judge non-specific binding of the NOVs to the complex matrices, the conjugate NOV nanotags were added to chicken broth in a control experiment. Another controlled study was done with the processed complex matrices alone. Clearly, *E. coli* DHα5 cells can be captured by DEP and detected with SERS using the NOV nanotags in both chicken broth and the soil solution. The interference and nonspecific signal of the matrices were negligible. Systematic optimization by varying the frequency and flow velocity in these two complex matrices are presented in Appendix B.2 (page 172). The results were very similar to those in distilled water (Figure 5.4), only with the optimum AC frequency at 150 kHz in chicken broth in contrast to 100 kHz in distilled water and the soil solution. These are distinct from that of the conjugated NOVs spiked in respective matrices at a concentration of $1.4 \times 10^{10}$ NOVs/ mL. However, the p-DEP capture of the bacteria was not observed in apple juice. This may be due either to the denaturation of the antibodies in the strong acidic solution (pH = 2.81 in the processed apple juice) preventing specific attachment of NOVs to bacteria or to the high conductivity of the apple juice resulting in negative value in Re[$K(\omega)$].

### *5.6.4 Assessment of Detection Sensitivity in a Portable System*

To demonstrate the potential capability of this method for use in a portable system, similar studies including flow velocity and frequency optimization were carried out with a portable Raman instrument (ProRaman L, Enwave Optronics. Inc.) in a manner similar to the earlier studies using the confocal Raman microscope. The results between these two Raman systems were very consistent, with the maximum flow velocity at 0.4 mm/sec (0.55 μl/s) and the maximum frequency of 100 kHz (Appendix B.3 A and B). However, the probe diameter at the focal point in the portable Raman system is about 100 μm (Appendix B.3C and inset of Figure 5.9), which is much larger than the 3.1 μm size in the confocal Raman microscope (Figure 5.5D).

This allows signals to be collected from many more bacteria and yields better statistics, but the laser intensity is lower as it is spread over a larger area.

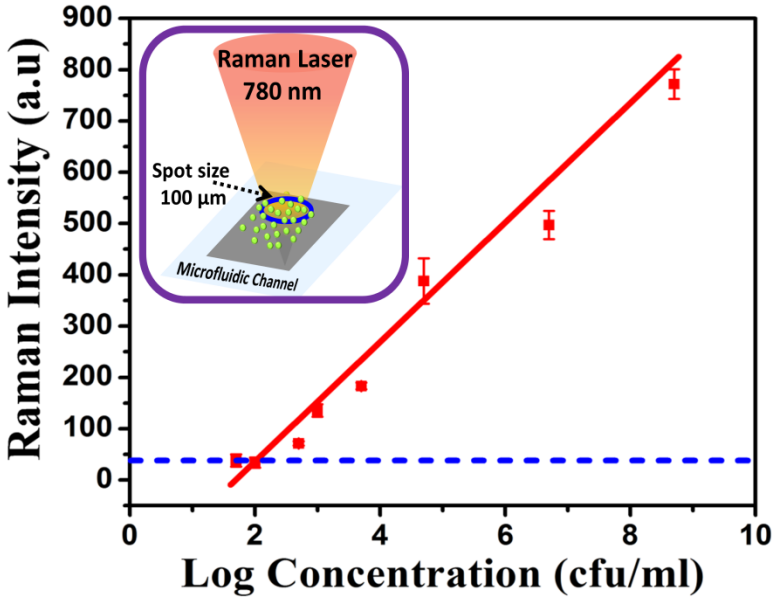


**Figure 5.9: The Raman intensity after 50 s of DEP capture from the bacteria solution with the concentration varying from 5 CFU/mL to 1.0 × $10^9$ CFU/mL.**

**The Raman measurements were carried out by focusing the laser beam within the 200 µm × 200 µm active DEP area with a ProRaman L portable Raman system (Enwave Optronics).Inset shows that 100 µm diameter laser focal spot aligned with 200 µm × 200 µm active DEP area. (Reprinted with permission from F. R. Madiyar, S. Bhana, L. Z. Swisher, C. T. Culbertson, X. Huang, J. Li, *Nanoscale*, 2015, 7, 3726-3736.)**

These two factors need to be balanced for the optimum performance. DEP capture kinetic curves over longer time (~250 s) at higher concentration (5 × $10^6$ CFU/mL) show a similar nearly linear increase in fluorescence and Raman signals over DEP time (AppendixB.3 D).

Figure 5.9 summarizes the SERS intensity of the captured NOV-labelled *E. coli* using the portable Raman setup while the *E. coli* concentration was varied from ~10 to 1 × $10^9$ CFU/mL.

The intensity of the QSY21 marker at the Raman shift of 1496 $cm^{-1}$ could be clearly separated from the carbon nanofiber signals at 1350$cm^{-1}$ (D-band) and 1600$cm^{-1}$ (G-band), respectively. The Raman intensity was found to be a linear function of the logarithm of bacteria concentration when the concentration C is above ~100 CFU/mL as follows:

$$(\text{Raman Intensity})_{\text{portable}} = 108.8 \times \log C - 214.7 \quad (5.1)$$

$$\text{Fluorescence Intensity} = 1224 \times \log C - 2650 \quad (5.2)$$

where RI was the increase in Raman intensity collected from a 100 μm diameter DEP area and FI the increase in the integrated fluorescence intensity over the 200 μm × 200 μm active DEP area, respectively, after 50 s of DEP capture. It is surprising that the RI signal is proportional to log*C* rather than directly proportional to *C*. The exact mechanism responsible for generating this relationship is not clear at this stage, but there are two possibilities to consider: (1) the rapid decay of the electric field at positions further away from the VACNF tip may generate a highly non-uniform DEP force (proportional to $\nabla E^2$) that does not act equally on all cells in the whole solution volume between the NEA and ITO electrodes; or (2) the first captured bacteria may significantly screen the electric field and quickly lower the total DEP force on other cells in the solution. Overall, the larger size of the laser focal spot (100 μm in diameter) allowed the collection of Raman signals from a larger number of captured bacteria. However, further increasing the Raman probe size to 300 μm gave a lower sensitivity, mainly due to lower excitation laser intensity as the power was spread out over a larger area.

For bacteria concentrations below the critical value $C_0$ = ~100 CFU/mL, no measurable signal above the background, i.e. $(RI)_{blank}$ = ~36 a.u., was detected. No captured bacterial cells were detected during the applied DEP period, which was limited by the slow mass transport of bacteria to the active area. However, the Raman intensity increased as more bacteria were passed

into the device at higher concentrations. The detection limit $\log C_{dl}$ was determined using calibration curve as follows:

$$\log C_{dl} = \log C_0 + 3\sigma_{blank}/m \quad \text{..... (5.3)}$$

where $\sigma_{blank}$ (~11.7) is the standard deviation of the Raman signal for bacteria concentration below $C_0$ and $m$ = 108.8 is the slope of the calibration curve. Thus, the concentration detection limit was determined to be ~210 CFU/mL. For fluorescence measurement the $\sigma_{blank}$ (~9.1) is the standard deviation of the fluorescence signal for bacteria concentration below $C_0$ ($C_0$ = ~500 CFU/mL, no measurable signal above the background) and $m$ = 1224 the slope of the calibration curve. Thus, the concentration detection limit for fluorescence measurements was determined to be ~827 CFU/mL (Appendix B.4)

The optimum flow velocity of 0.4 mm/sec corresponded to a volumetric flow rate of 0.55 μL/sec. For a 50 s DEP period, ~6 bacteria passed through the fluidic channel at the concentration detection limit of 210 CFU/mL. Even if the capture efficiency were only 15%, at least one bacteria would be captured, and this event would be detectable by SERS with this portable system. In the current DEP design, the 200 μm width of the active NEA array is much smaller than the total channel width (i.e. the 2 mm diameter circular chamber, see Figure 5.2C) for the ease of aligning the NEA area within the fluidic channel. There detector design is, therefore, far from optimized since many bacterial cells may pass through the active DEP area and not be captured. In the future, the channel size and the active DEP area will be reduced close to the Raman probe size so that all bacteria will be forced to pass through the active DEP zone so that they can be captured for Raman measurement. In addition, the DEP capture time can be increased from 50 s to several minutes to ensure more bacterial cells are captured. With such

optimization, the concentration detection limit is expected to be lowered by a factor of 10, to ~10 CFU/mL.[172]

## 5.7 Conclusion

In conclusion, the integration of a DEP chip for bacteria concentration and SERS detection for specific microorganism identification has been demonstrated. The DEP based on a VACNF NEA acts as an effective and reversible electronic manipulation technique to rapidly concentrate bacteria into a micro area from the solution flowing through the microfluidic channel. A highly sensitive SERS nanotag based on QSY21 adsorbed on IO-Au NOVs provides greatly enhanced Raman signals and specific recognition of *E. coli* DHα5 cell through highly selective immunochemical binding using two specific antibodies. The SERS signal measured with both of a confocal Raman microscope and a portable Raman system during DEP capture was fully validated with fluorescence measurements under all DEP conditions. This detection method yields a concentration detection limit of 210 CFU/mL using the portable Raman system, and 827 CFU/mL by fluorescence microscope, which can be further improved. The results demonstrated the potential to develop a compact portable system for rapid and highly sensitive detection of specific pathogens in fields.[172]

# Chapter 6 - Integration of Nanostructured Dielectrophoretic Device with Impedimetric Detection of *Vaccinia* Virus

## 6.1 Principle of Impedimetric Detection

The change in bio-molecular interactions occurring near the electrode-electrolyte interface can be measured using impedance. For this technique, typically, a small signal perturbation (AC voltage) is applied across the electrode system, and the resulting current that flows through the system is measured. The magnitude and phase response are measured at different frequencies, and hence impedance spectrum is obtained over a wide frequency range (1 mHz to 1 MHz).

Electrical impedance ($Z$) is defined as $V(t)/I(t)$ the ratio of an incremental change in voltage to the resulting change in current.

$$|Z| = \frac{V_o \sin(2\pi ft)}{I_o \sin(2\pi ft + \varphi)} \quad \text{..... (6.1)}$$

Where $V_o$ and $I_o$ are the maximum voltages and current signal, $f$ is the frequency, $t$ is time, $\varphi$ is the phase shift between the voltage-time and current-time functions. The impedance is a complex value affected by multiple factors, which is described either by the modulus $|Z|$ and the phase shift φ or alternatively by the real part, $Z_R$, and the imaginary part, $Z_I$, of the impedance. When the current and the potential are in phase ($\varphi$=0), Equation 6.1 is simply the expression of Ohm's law, and the impedance as a resistor.

### *6.1.1 Principle and Application of Microbiology Impedance*

Electrical impedance measurement of microbial growth was put forward by G.N.Stewart in 1899.[175] In impedance microbiology, the change is typically measured directly or inderectly using a pair of electrodes submerged in the growth medium or the reactant solution. A pair of

metal electrodes is immersed in the medium that is inoculated with the testing bacteria. The bacterial metabolism causes the release of ionic metabolites from the live cells, and these reactions lead to the change in the impedance that is recorded with time. The decrease in impedance is attributed to, (1) the energy metabolism, through which bacteria consumes oxygen and sugars to produce carbon dioxide, lactic acid, carbonic acid, and ions released during this stage. (2) the ion exchange through the cell membrane. Ions (such as $K^+$ and $Na^+$) are actively transported across ion channels embedded in the cell membrane, which serves to regulate the membrane potential and the osmotic difference between the interior and exterior of the cells.

In the indirect technique, electrodes are immersed in a separate solution (usually a potassium hydroxide solution) instead of the inoculated growth medium. The gasses (mainly $CO_2$) produced from bacterial metabolism are absorbed by the potassium hydroxide solution, which leads to a decrease in the conductance of the alkaline solution, which can be measured. The Figure 6.1A shows the two electrodes submerged in the culture medium for bacteria growth. In Figure 6.1B, the impedance is stable in the lag phase of bacteria growth cycle. The impdance starts decreasing with the initiation of the log phase of the bacteria and later reached the plateau phase when ~ $10^8$ CFU/mL bacteria are grown and all the resources in the medium have been metabolized.

In Figure 6.1C, a simple equivalent circuit is illustrated consisting of a resistor and a capacitor in series to represent the behavior of the impedance test system when two electrodes are immersed in a conductive medium. Here, $C_{dl}$ is the double layer capacitor of each electrode and $R_s$ is the solution resistor. Based on the equivalent circuit, when an alternating sinusoidal potential is applied to the system during test, the impedance ($Z$) of the system is a function of its resistance ($R_s$), capacitance ($C_{dl}$) and the applied frequency ($f$), as expressed in Equation 6.2.

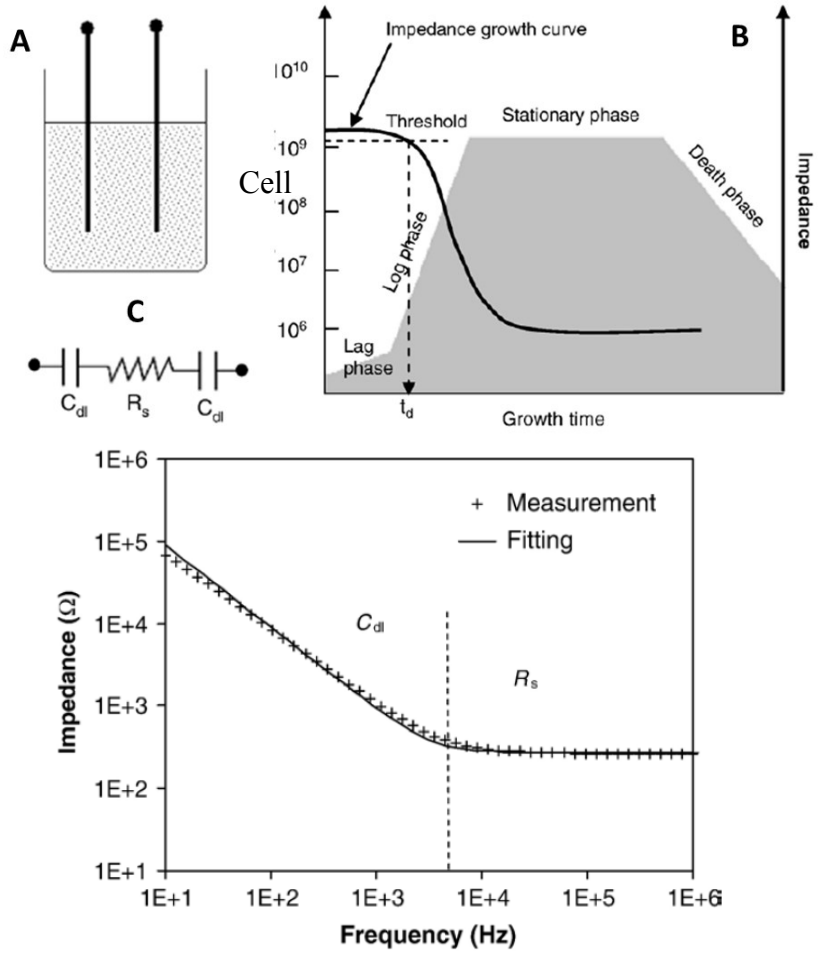


**Figure 6.1: Impedance measurement in microbiological set-up**

**(A) A typical setup of a two-electrode system for impedance measurement. (B) Schematic plot of the growth curve of bacteria and corresponding impedance change. (C) A simplified equivalent circuit for a two-electrode system. $C_{dl}$ and $R_s$ represent the double layer capacitance of the electrode and the solution resistance respectively. (D) The plot of Impedance vs. Frequency. $R_s$ is the medium resistive region. $C_{dl}$ is the double layer capacitive. The applied amplitude was 5.0 mV and the cell number of *S. typhimurium***

**detection was 1.1 × $10^3$ CFU/mL. (Reprinted with permission from *Biosens. Bioelectron.*, L. Yang, et al., 2003).**

$$|Z| = \sqrt{R_s^2 + \left(\frac{1}{2\pi f C_{dl}}\right)^2} \quad \text{..... (6.2)}$$

The Figure, 6.1D shows that $R_s$ of the medium decreases when bacteria metabolize large and uncharged molecules into small and charged particles in the medium but the $C_{dl}$ is unchanged.

The value of double layer capacitance depends on many factors including electrode potential, temperature, ionic concentration, type of ions, and electrode surface properties (e.g., electrode roughness, adsorption, etc.). The impedance measurement depends on the applied frequency. The low-frequency range from 10 Hz – 10 kHz is called the double layer capacitive region. In it the total impedance decreases as the frequency increases. The double layer capacitance ($C_{dl}$ *region)* becomes the primary source contributing to the total impedance, so the medium resistance can be ignored. At the high-frequency range, 500 kHz – 1 MHz, the impedance becomes independent of the frequency, the double layer capacitance is negligible, and the total impedance due to $C_{dl}$ nears zero. Thus, the only contribution to the total impedance at high frequencies is the medium resistance. This region is defined as the resistive region in which the conduction of ions in the medium dominates the signal. The impedimetric detection of metabolites originated from bacterial growth is also known as *'impedance microbiology*'. This technique is applied in a variety of fields: detection and monitoring of microorganisms, detection of antibiotics, analysis of clinical and pharmaceutical microbiology and sampling environmental specimens.[176-180]

### *6.1.2 Impedance Based Biosensing*

Impedance based biosensors take advantage of the changes between electrode and electrolyte interface caused by one of two different mechanisms—one measuring double layer capacitance ($C_{dl}$) and the other charge transfer resistance ($R_{CT}$).

Mechanism 1: The attachment of a biorecognition element to the electrode can decrease the capacitance ($C_{dl}$) due to the increase in the thickness of the double layer. This is called a non-Faradic impedance measurement. The biorecognition element is anchored on the electrode, and when the target molecule attaches to the biorecognition element, $C_{dl}$ is decreased and results in impedance change.

Mechanism 2: The attachement of the bacterial cells to a biorecognition element on the electrode surface can be monitored by the presence of a redox couple $[Fe(CN)_6]^{3-/4}$. The charge transfer resistance ($R_{CT}$) is the parameter measured by the biosensor. This is called a Faradic impedance measurement. The attachment of bacterial cells retards the interfacial charge transfer kinetics and increases the $R_{CT}$. A Nyquist plot ($Z_{im}$ vs.$Z_{re}$) is the best way to visualize and determine the $R_{CT}$ change.

### *6.1.3 Advantages of Impedance Based Sensing*

The following two sections will elaborate on the advantages and challenges concerning impedance based sensing.

**High Sensitivity:** Impedance measurement is highly sensitive to the molecular interactions near the electrode surface.

**Label-free detection:** Impedance relies on the inherent properties of molecules, and it does not require the use of labels. This makes impedance-based sensing suitable for detection of specific molecules, such as proteins, which are difficult to label.

**Real-time detection:** In impedance experiments it is possible to study the evolution of the interface impedance with biomolecular interactions as a function of time. The real-time detection allows us to understand reaction mechanisms and helps us to better estimate the analyte concentration.

**Ease of Integration:** Since the impedance is fully electronic in nature, sensors can be readily incorporated into the standard electronic integrated circuits (ICs). The use of ICs has greatly revolutionized the field of electronics by enabling one to build extremely compact, highly complex, and densely packed electronic systems with excellent yield and reliability. The possibility of creating integrated impedance biosensors which are portable, cost-effective and able to be used for point-of-care applications is exciting.

### *6.1.4 Challenges in Impedance Measurements*

There are three primary challenges when measuring impedance of biomolecules:

**Non-specific binding:** Biomolecules are usually present in complex matrices, and the direct attachment of the target on the electrode can lead to large errors unless the target is separated from the matrices and interfering molecules. To address this challenge, passivation of the electrode must be carried out using Bovine Serum Albumin (BSA) or other self-assembled monolayer molecules that act as blocking (passivation) molecules.

**Surface cleaning:** In order to get rid of the attached molecules on the electrode, active cleaning cycles are required. For the purpose of impedance measurement on a gold electrode, strong acidic chemicals like *Piranha* solutions or *Aqua Regia* are used. For the current method of impedance measurement on the carbon electrode, the device is washed with Clorox solution (1%) for 15 min, deionzed water for 15 min, and isopropanol (50 %) for 15 min to remove the debris of the *Vaccinia* virus.

**Variation in the biomolecules conditions:** The interface impedance varies with the type of biomolecules used. These can differ in size, structure and ionic states under various electrolyte concentrations and pH conditions, making it difficult to theoretically predetermine the magnitude of impedance change. In order to mitigate the effect of variations, it is advisable to make use of real-time detection, in which we measure the changes in impedance rather than the absolute values.

The current study is significantly different from the mechanisms mentioned above in the following ways:

1. To maintain linear response during impedance measurement processes, usual impedance measurements are preceded with small amplitude AC voltage. This method has a poor signal to noise ratio at higher voltages and is not suitable for obtaining sensitive measurements. In contrast, it has been proven that the carbon nanofiber NEAs can operate at high voltages (10 to 200 mV) showing good linearity.[181] This helps to eliminate stochastic errors, provides high stability and improves the signal-to-noise (S/N) ratio. The impedance of *Vaccinia virus* requires a significantly larger voltage amplitude as compared to other bioimpedance techniques where small amplitude is applied.
2. Neither biomolecules (i.e., antigen-antibody complex) nor redox molecules were considered for this study, hence the measurement of *Vaccinia* virus with impedance was considered label-free. Instead, the high electric field generated at the nanoelectrode due to 'point-and-lid' geometry acted as a driving force to attract particles towards the nanoelectrodes. The capture of the virus on the

nanoelectrode caused the changes in properties at the electrode−electrolyte interface, thus affecting both $C_{dl}$ and $R_{CT}$.

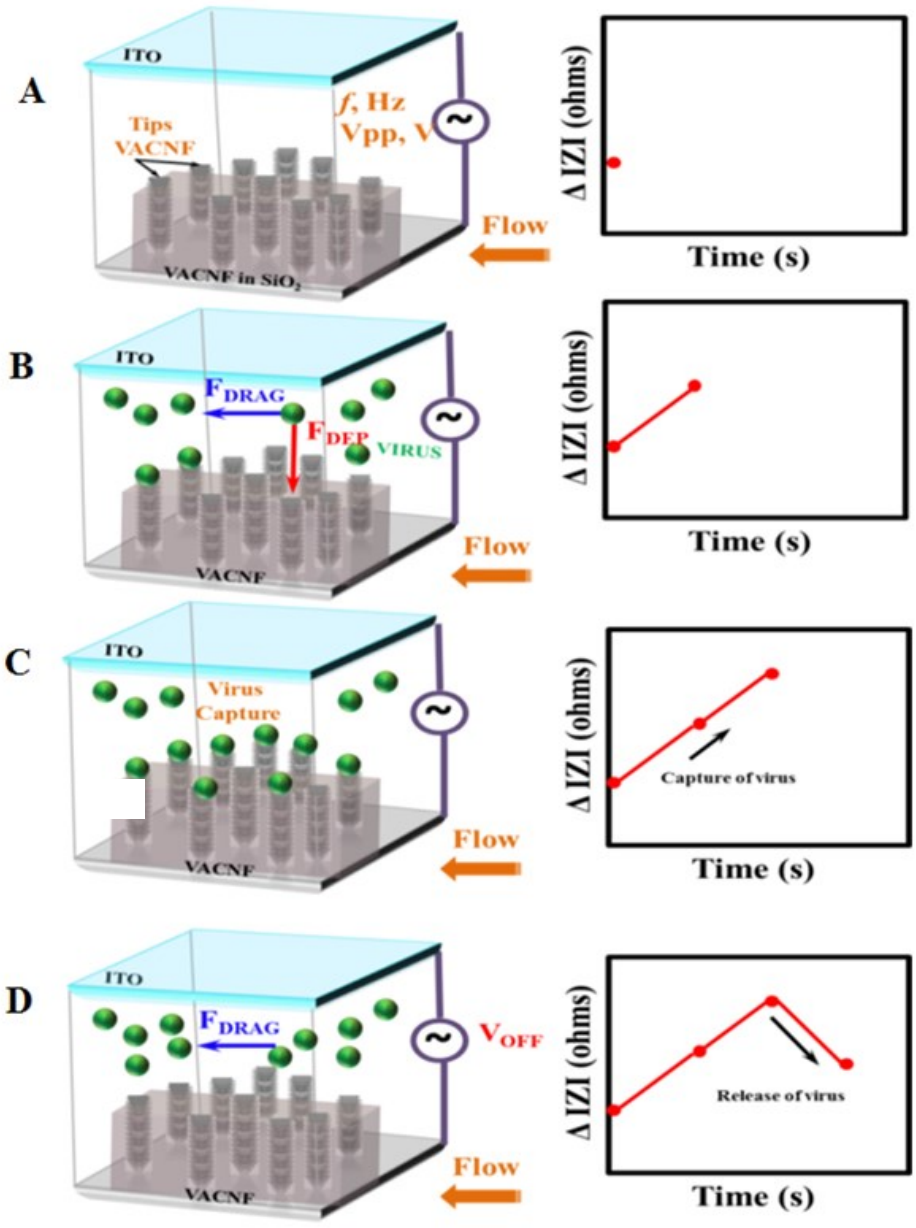


**Figure 6.2: Schematic diagram of 'point-and-lid geometry' with vertically aligned carbon nanofiber (VACNF) and indium tin oxide (ITO).**

**(A) The frequency and voltage applied to vertical carbon nanofiber tips exposed and ITO as a control sample (B) Virus solution is passed through the device. $F_{DRAG}$ is electro-hydrodynamic force acting on the virus in the direction of the flow. $F_{DEP}$ is dielectrophoretic force acting vertically downwards to the tips of the electrode. The increase in impedance due to the capture of the virus in the high electric field on the tips ($F_{DEP}$). (C) The real-time increase in impedance due to the capture of the virus on the nanoelectrode. (D) The release of the viruses causes a decrease in impedance.**

## 6.2 Experimental Details

### *6.2.1 Virus Cell Culture and Labeling*

Stocks of *Vaccinia* virus (Copenhagen strain, VC-2) were amplified by infecting HeLa cells knocked-down for an antiviral protein kinase, PKR (HeLa PKR-KD) to achieve optimal yield. Cells were cultured in a 37˚C incubator in the presence of 5% $CO_2$ in Dulbecco's Modified Eagle's Medium (DMEM) supplemented with 5% Fetal Bovine Serum (FBS) and 25 μg/ mL Gentamicin. All virus work was performed in a BSL-2 laboratory equipped with two biosafety cabinets by trained personnel in Professor Stefan Rothenburg's Lab. Twenty 100 mm tissue culture plates were seeded with a single monolayer of HeLa PKR-KD cells and were infected at a low multiplicity of infection (estimated at around 0.001). For every infection, growth media was removed from each plate of cells, and a volume of virus inoculum was added to cover the bottom of the plate (3.0 mL /100 mm plate). The virus was allowed to adsorb to the cells for one hour before the inoculum was removed, and fresh media was replaced in the plates. The infections were allowed to incubate at 37˚C for 48-60 hr. Infected cells were then collected from each plate, pelleted by low-speed centrifugation (350 g), washed once with 10.0 mL

phosphate-buffered saline and pooled into a single tube to be pelleted again by centrifugation at low speed. The buffer was then removed, and the pellet was frozen and stored at -20˚C.

The cell pellet was warmed to 4˚C and resuspended in 10.0 mL of pH 8.0 10 mM Tris-HCl buffer. Cells were lysed and homogenized in a 40.0 mL sterile glass Dounce homogenizer. The procedure was repeated twice with sonication for 2 min at 50% power in a cup sonicator. All steps were performed at 4˚C to maintain viral integrity. The lysate was spun down at low-speed (350 g) to form pellet of cell debris and discarded. The supernatant contained viruses was further processed for purification.

The virus-containing supernatant was first purified through a 36% sucrose gradient buffered in 10.0 mM Tris-HCl, pH 8.0, using a Beckman-Coulter ultracentrifuge (SW 28 swinging bucket rotor) at 33,000 g for 80 min at 4˚C. After centrifugation, the supernatant was discarded, and the virus pellet was collected in 1.0 mL 10.0 mM Tris-HCl, pH 8.0. The virus suspension was then sonicated again using the cup sonicator at 50% power for 2 min to disrupt viral aggregates and any remaining cellular debris. A second centrifugation step using a 25-40% sucrose gradient (in 10.0 mM Tris-HCl, pH 8.0) at 26,000 g for 50 min was done to collect virus particles, which formed a visible band near the middle of the sucrose gradient, while allowing heavier cell debris to form a pellet at the bottom of the tube. The sucrose gradient was prepared by overlaying a 25% sucrose solution in a 40% sucrose solution and then using a Gradient Master (BioComp) to mix them into a gradient. The collected virus was then pelleted in a final centrifugation step diluted in 1.0 mM Tris-HCl, pH 8.0 at 33,000 g for 60 min and the virus pellet was resuspended in 1-2 mL 1.0 mM Tris-HCl buffer, aliquoted in 1.5 mL tubes and stored at -80˚C.

#### *6.2.1.1 Vaccinia Virus Inactivation*

Before inactivating the virus sample, a small amount was removed to obtain the original titer by plaque assay. The remaining sample was spread on the bottom of a sterile 100.0 mm dish and placed 3-8 cm directly below a UV bulb (234 nm). The plate was manually rocked to distribute the virus solution under the UV light for 10 min and was then collected and stored in a 1.5 mL tube at -80˚C. Virus inactivation was confirmed by plaque assay before the sample was moved out of BSL-2 containment and further work done.

#### *6.2.1.2 Vaccinia Virus Quantification and Imaging*

*Vaccinia* virus prepared for these experiments was titered by standard plaque assay on RK-13 cells expressing two *Vaccinia* virus genes that promoted viral replication by inhibiting antiviral responses in these cells (Rahman, MM, 2013). Briefly, serial dilutions of the original stock (live) and the UV-inactivated virus solution was used to infect 12-well plates of the cells. The number of plaques formed in each dilution was counted to find the original stock concentration in plaque-forming units per milliliter (pfu/mL). Each infected monolayer of cells was overlaid with 1% carboxy-methyl cellulose dissolved in dulbecco's modified eagle's medium (DMEM) supplemented with 5% fetal bovine serum (FBS) to prevent virus dissemination and isolate the forming plaque. Plaque assays were run for three days to obtain an optimal visualization of formed plaques for live viruses and confirm the lack of plaques in UV-inactivated samples. The media was removed from each well and 1% crystal violet in a 20% ethanol solution was added to visualize the virus plaques. Crystal violet is only taken up by living tissue, allowing identification of the clear infected cells. The plaque counting assay is shown in Figure Appendix C.1 (page 176). The transmission electron microscope (TEM) imaging of the *Vaccinia* virus was carried out by adding 5.0 µl of phage suspension to a 400-mesh copper grid with 5.0 µl of 2% uranyl acetate. The droplet wicked off after 45 sec and the

grids were then air-dried. The grids were examined by TEM (FEI CM 100 transmission electron microscope) with AMT digital capturing system as shown in Appendix C.2 (page 177)

#### *6.2.1.3 Vaccinia Virus Labeling with Fluorophores*

Labeling of the viruses was carried out with DiO lipophilic dye (Life Technologies) that stains the outer envelope of the virus and Propidium iodide dye that stains the nucleic acids. The 5.0 mM stock solution was prepared by sonicating solid DiO dye in pure ethanol for 15 min. Before making the working solution, it was essential to ensure the solid DiO dye remained dissolved in the ethanol. The 50 μM working solution was prepared by diluting with water. All these procedures were carried out at room temperature in a dark room to prevent exposure of fluorophores to the light. For optimal labeling of the virus, 200.0 μl of the virus solution was added to 50 μl of 50.0 μM working solution of DiO dye at 37ºC for 2 hr in an incubation oven. To remove excess dye, the viruses were spun at 14,000 rpm for 5 min in a centrifuge (Minispin® plus, Eppendorf) using Amicon® Ultra 0.5 centrifugal filter devices (UFC 510096) with 0.5X PBS buffer. To obtain concentrated virus solution the filter unit was disassembled and placed in the tube upside down to spin at 14,000 rpm for 10.0 min. The solution was collected and washed two times in a similar way to remove the dye residue. The final wash was carried out using aqueous 280 mM D-mannitol (Fisher BP686500) solution. The concentration of the viruses for the experiment was ~$3 \times 10^6$ pfu/mL (except for the concentration tests). The nucleic acid (DNA) of the viruses was labeled with 50 μl 20.0 μM of Propidium Iodide (PI) aqueous solution. All the solutions were filtered and sterilized with 0.20 μm at 121˚C for 20 min.

### *6.2.2 Experimental Setup*

200 μm × 200 μm area in the microfluidic chip was focused under 50X on an upright fluorescence optical microscope (Axioskop 2 FS plus; Carl Zeiss). This microscope was

equipped with Axio Cam MRm digital camera and filter set with an excitation wavelength of 485-20 nm and an emission wavelength of 515-565 nm (filter set 17, Carl Zeiss) for DiO dye and an excitation wavelength of 640-20 nm and an emission wavelength of 690-50 nm (filter set 60, Carl Zeiss) for PI dye. The fluorescence videos were recorded at an exposure time set to 0.5 sec using multi-dimensional acquisition mode in the Axio-vision 4.7.1 release software (Carl Zeiss MicroImaging, Inc.) for 85 sec. During which, no voltage ($V_{off}$) was applied in the initial ~16 sec, fixed AC voltage at different frequencies was applied ($V_{on}$) for ~54 sec, and no voltage was applied ($V_{off}$) in the last ~15 sec. The response of *Vaccinia* Virus cells was monitored using a fluorescence microscope at different frequencies ($f$) of the sinusoidal AC voltage, at different flow velocities and concentration of *Vaccinia* virus. The exact linear flow velocity was calculated within the focal depth of the microscope from NEA surface in the 200 μm × 200 μm by using the videos. Videos were analyzed using interactive measurement module in Axio vision 4.7.1 release software (Carl Zeiss) to quantify the fluorescence intensity in the active region before and after capture.

## 6.3 Discussion

### *6.3.1 Assessing the Labeling of Vaccinia Virus*

Viruses labeled with two different dyes were observed under a fluorescence microscope. The first DiO dye stains the lipophilic membrane of the viruses manifesting green fluorescence. The second dye is a cell-impermeable Propidium Iodide (PI). When the membrane is ruptured, the DNA escapes into the solution intercalating with PI dye, increasing red fluorescence by 500-fold (as shown Figure 6.7A). The virus solution was observed in a *Petroff-Hausser* counting

chamber (Hausser Scientific Partnership, Horsham, PA) to ensure that fluorescence from lipophilic membrane stained with DiO was observed.

### *6.3.2Assessment of Impedance Detection and DEP Optimization*

To validate and optimize the conditions, DEP capture was visually monitored under a fluorescence microscope at various flow velocities (Figure 6.3A) and voltages (Figure 6.3B) following our previously established method.[106, 117] The representative snapshots from a fluorescence video during DEP capture of the *Vaccinia* virus within the 200 μm × 200 μm active NEA area are shown in Figures 6.3C to E. Impedance was measured using the Solartron 1260 SMaRT software and data was analyzed using Origin data analysis software.

Similar to our previous report on the *bacteriophage* capture[27], the AC voltage $V_{pp}$ was turned on for 54 sec while the virus solution was passed through the channel. The viruses were collected on randomly distributed VACNF tips. Both the fluorescence and impedance signals associated with the captured viruses were found to increase linearly with time. The difference between fluorescence signal ($f_{signal}$) and fluorescence background ($f_{background}$) resulted in the integrated fluorescence intensity ($\Delta F$) at the end of the 54 sec capture period. Similarly, the difference between final impedance signal ($Z_F$) and the intial impedance signal ($Z_O$) and its ratio with intial impedance signal resulted in percentage change of impedance [% ($Z_F$ -$Z_O$)/ $Z_O$]. The pDEP capture experiments were carried out at the flow velocities ($v$) ranging from 0.11 to 8.2 mm/sec (Figure 6.3A) at fixed AC voltage of 8 $V_{pp}$ and the frequency of 1.0 kHz. The number of captured viruses initially increased with increasing flow rate until a maximum was reached at 0.401 mm/sec (corresponding to the volumetric flow rate of 1.0 μL/s). Further increase in flow velocity resulted in a decrease in capture efficiency. This trend agrees well with our previous study.[27] An image of the final video frame taken using the 0.401 mm/sec flow rate is shown in

Figure 6.3D. In the snapshots, the bright spots represent single virus particles. The percentage change in impedance measurement follows the same trend as the fluorescence measurements.

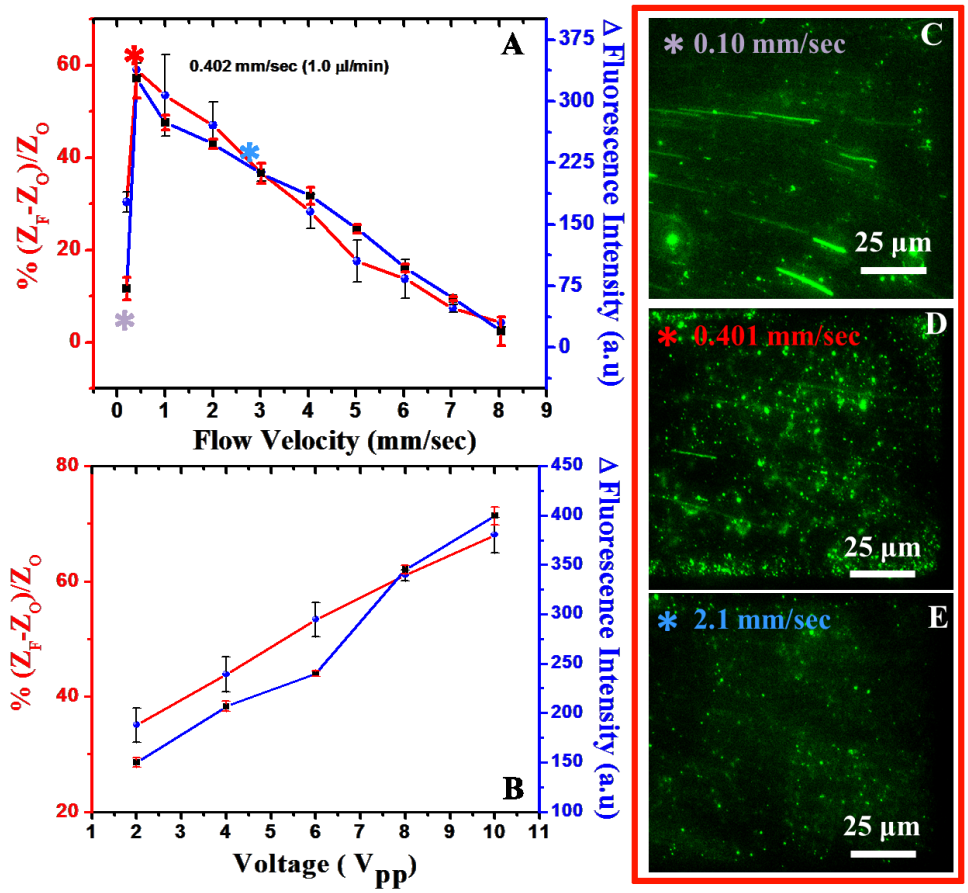


**Figure 6.3: Assessing DEP capture of 3.0 × $10^6$ pfu/mL *Vaccinia Virus* with fluorescence and impedance measurements at various flow velocities.**

**(A) The study of flow velocity at fixed AC frequency (1 kHz) and voltage (8 $V_{pp}$). (B) Systematic study of the voltage at fixed flow velocity (0.401 mm/sec) and fixed AC frequency (1 kHz) (C-D) Corresponding snapshots from the fluorescence videos after 75 s of DEP capture of *Vaccinia virus* at fixed frequency (1 kHz) at (C) 0.1 mm/sec (D) 0.401 mm/sec and (E) 2.10 mm/sec.**

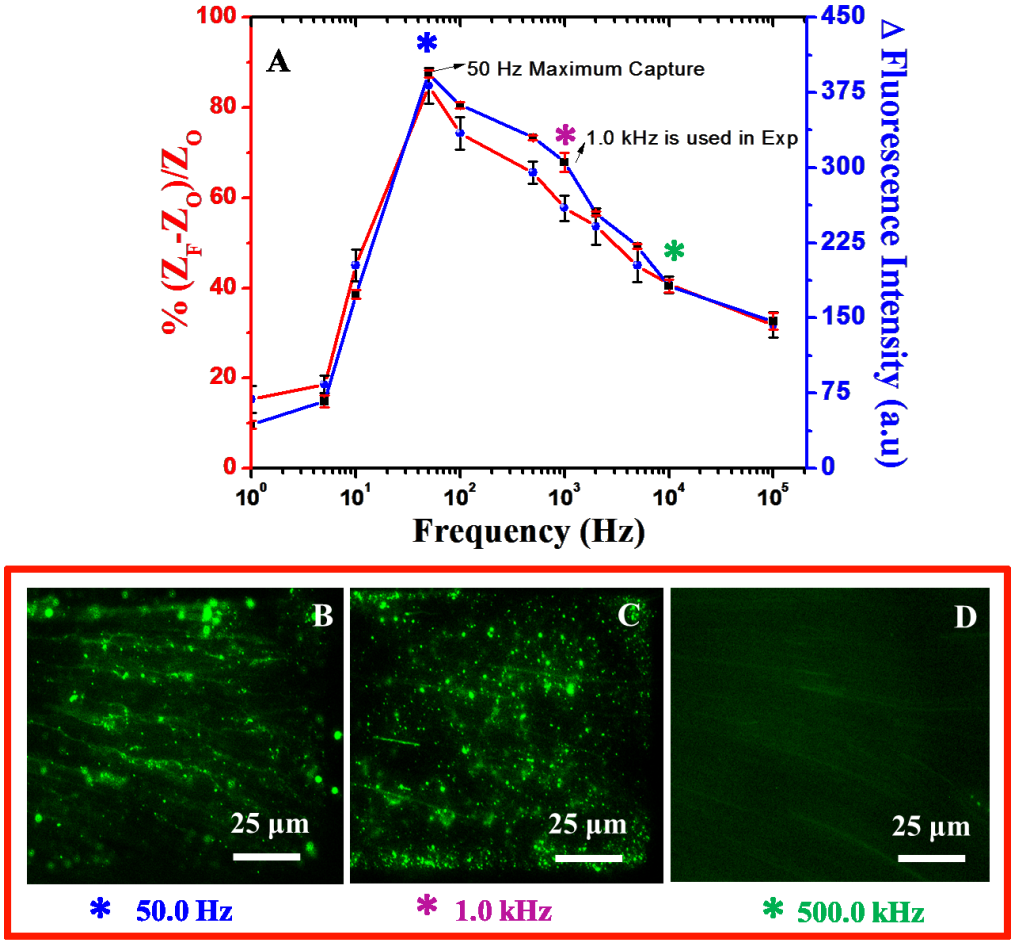


**Figure 6.4: Assessing DEP capture of 3.0 × $10^6$ pfu/mL *Vaccinia Virus* with fluorescence and impedance measurements at various AC frequencies.**

**(A) The study of AC frequency at fixed flow velocity (0.401 mm/sec) and voltage (8 $V_{pp}$). (B-D) Corresponding snapshots from the fluorescence videos after 75 s of DEP capture of *Vaccinia* virus at flow velocity of 0.401 mm/sec at (B) 50.0 Hz, (C) 1.0 kHz, (D) 500.0 kHz.**

At $v \geq 0.401$ mm/sec (Figure 6.3A), the number of captured *Vaccinia virus* decreased because only those viruses near to the VACNF tips were able to be captured, while the rest of the

viruses remained in the fluid flow because of the higher hydrodynamic drag force ($F_{DRAG}$) as compared to the dielectrophoretic force ($F_{DEP}$).

The magnitude of $\nabla E^2$ depends on both the DEP device design and the amplitude of the applied AC voltage. Low voltage capture is preferred for bioparticles to prevent potential cellular damage. Figure 6.3B shows results of the voltage varying between 3 to 10 $V_{pp}$ while other parameters were fixed at the optimized conditions, i.e. flow velocity of 0.401 mm/sec and frequency of 1.0 kHz. The DEP capture indicated by impedance and fluorescence signals increased monotonically with the voltage and showed high capture at 10 $V_{pp}$. However, a large impedance signal was observed even at 4 $V_{pp}$. To prevent virus particle rupture at high voltages, the voltage amplitude was kept lower than 10.0 $V_{pp}$. The experiments were carried out at 8.0 $V_{pp}$ to get a reliable change in impedance.

Relating to particle permittivity dependence of $F_{DEP}$ (Equation 2.3 and 2.4), each type of the bio-particle has an optimum DEP frequency determined by its internal composition and structure. As shown in Figure 6.4A, both fluorescence intensity, and impedance show optimum DEP capture of the *Vaccinia* virus at ~50.0 Hz with a fixed peak-to-peak voltage of 8 $V_{pp}$ and a flow velocity of 0.401 mm/sec. The optimum frequency of the *Vaccinia virus* is different from the bacteriophage virus (10 kHz) used in a previous study. This can be attributed to structure composition of *Vaccinia* virus, which is composed of an outer lipophilic membrane with inner polarizable nucleic acids as compared to *bacteriophage* T4r which is comprised of protein capsid with DNA. The optimum frequency for the capture of the *Vaccinia* virus was at 50 Hz, but this weakened the reversible nature of the pDEP capture. This is confirmed by the impedance measurement that did not reach its initial value of background after the voltage was turned off. This condition led to excessive background impedance and fluorescence intensity. Hence, 1.0

kHz was adopted in all future experiments because reversibility of impedance measurements was observed with reasonable change.

Figure 6.5 shows the kinetic curves of pDEP with virus concentrations between $3.0 \times 10^3$ to $3.0 \times 10^6$ pfu/mL. The impedance and fluorescence measurements were taken simultaneously to replicate real-time capture.

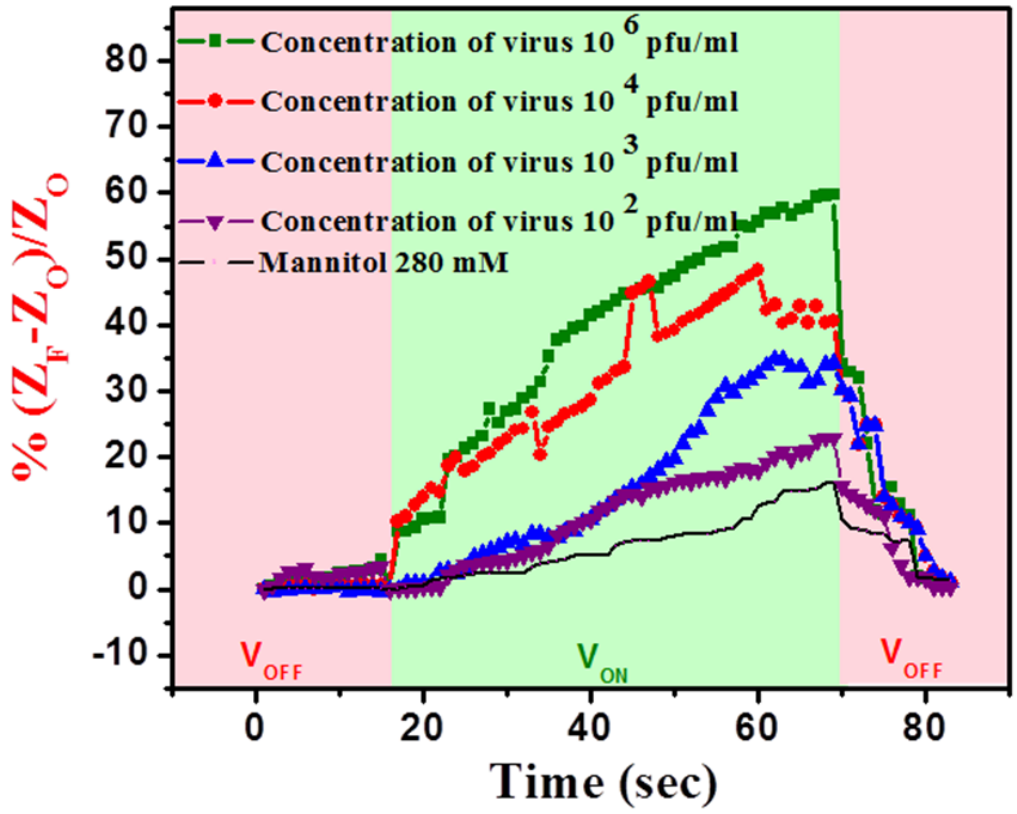


**Figure 6.5: Real-time impedance detection of the *Vaccinia* virus on VACNF.**

**(A) The impedance of *Vaccinia* virus is measured in real-time. In the experiment, a small voltage 0.5 $V_{pp}$ was applied for 15 sec and the capture of the virus takes place in 60 sec at 8 $V_{pp}$. The decrease in impedance takes place when voltage is turned back to 0.5 $V_{pp}$, causing the release of the virus from the VSCNF tips.**

In the real-time experiment, a voltage of 0.5 $V_{pp}$ was applied for 16 sec which served as the background impedance. After 16 sec, the voltage was increased to 8.0 $V_{pp}$ for 54 sec. During this period, the viruses were captured on the tips of the VACNFs lead to increase in impedance. After 54 sec, the voltage was turned back to 0.5 $V_{pp}$ and the captured viruses were immediately released bringing the impedance back to its initial condition. The control experiment was performed using 280 mM Mannitol solution. Even without virus particles, an increase in impedance was displayed under identical conditions used in the experiment (black line in Figure 6.5). This experiment indicates that pDEP capture on VACNF tips is reversible and limited by the mass transport of viruses to the active region. The additional cell debris and species present in the solution are also affected by the high electric field, giving background impedance. The reversible nature of the pDEP after the optimization of the parameters allows us to reuse the device several times.

### *6.3.3 Assessment of Limit of Detection*

To demonstrate the potential capability of the impedance method, a concentration-dependent study was employed to determine the limit of detection. The factors that affect limit of detection during DEP capture are the exogenous molecules in the sample solution, the molecules that attach to the nanoelectrode nonspecifically, and the capture time. The latter two factors can be manually controlled by increasing the capture time and by washing the chamber with a series of solutions (i.e., 1% Clorox solution, 50% isopropanol, double D.I water and 280 mM mannitol solution) to reduce the background impedance.

Figure 6.6 summarizes the percentage of impedance change of the captured *Vaccinia* virus when the concentration varies from ~$3 \times 10^3$ to $3 \times 10^6$ pfu/mL. The experiments were carried out for 54 sec at a flow rate of 0.401 mm/sec with the frequency of 1.0 kHz and a voltage

of 8.0 $V_{pp}$. The percentage impedance change was found to be a linear function of the logarithm of virus concentration when the concentration, $C$, was above ~ 300 pfu/mL as follows:

$$\frac{\Delta Z}{Z_0} = 12.1 \times Log\ C - 8.09 \quad (6.3)$$

where $\Delta Z$ is the difference in final ($Z_F$) and the intial impedance ($Z_O$), hence $\Delta Z/Z_O$ is the percentage impedance change collected over the 200 μm × 200 μm active area, after 54 sec of pDEP capture. At low concentration, the impedance has direct relationship to the log concentration as seen in previous DEPIM studies[94], but the mechanism is not yet completely understood. The rapid decay of the electric field at positions further away from the VACNF tip may generate a highly non-uniform DEP force (proportional to $\nabla E^2$) that does not equally impose on all the cells across the whole solution volume between the nanoelelctrode array (NEA) and the indium tin oxide coated glass (ITO) electrode. For virus concentration below the critical value $C_0$ = ~300 pfu/mL, no measurable signal above the background, i.e. $(I)_{blank}$ = ~ 14.53 ohms, was detected. No virus particles were captured during the applied DEP period, which was limited by the slow mass transport of virus to the active area. However, the impedance intensity increased as more viruses were passed into the device at higher concentrations. The detection limit $\log C_{dl}$ was determined using the equation as following:

$$\log C_{dl} = \log C_0 + 3\sigma_{blank} \quad (6.4)$$

where $\sigma_{blank}$ (~3.77) is the standard deviation of the impedance signal from the viruses concentration below $C_0$ and $m$ = 12.1 is the slope of the calibration curve. Thus, the concentration detection limit was determined to be ~ 2.58 × $10^3$ particles/ mL. It is conceivable that at high concentrations the impedance becomes stable and achieves a plateau phase because the capture is limited by the available sites on the VACNF tips in a microfluidic channel. It

appears that the exposed active area in 200 µm × 200 µm gets completely saturated as the concentration increases.

### *6.3.4 Assessment of Electroporation of Vaccinia Virus under High Electric Field*

The electric field parameters, such as amplitude, length, shape, number of repeats and interval between the electric pulses, have several effects on the membrane of the bioparticles.[182, 183] If the bioparticles are exposed to the high electric field for longer periods of time, the pores become permanent, resulting in leaking of the nucleic acids. This is called irreversible electroporation and it is widely used for nucleic acid extraction.[184-187] Electrical rupture of the membrane to extract nucleic acids is advantageous as compared to conventional methods such as freeze-thaw, sonication, chemical lysis, and heat application because of the high risk of nucleic acid denaturation and breakage.[188] The electrical method of rupture is effective to avoid all these issues when extracting nucleic acids from the cells.

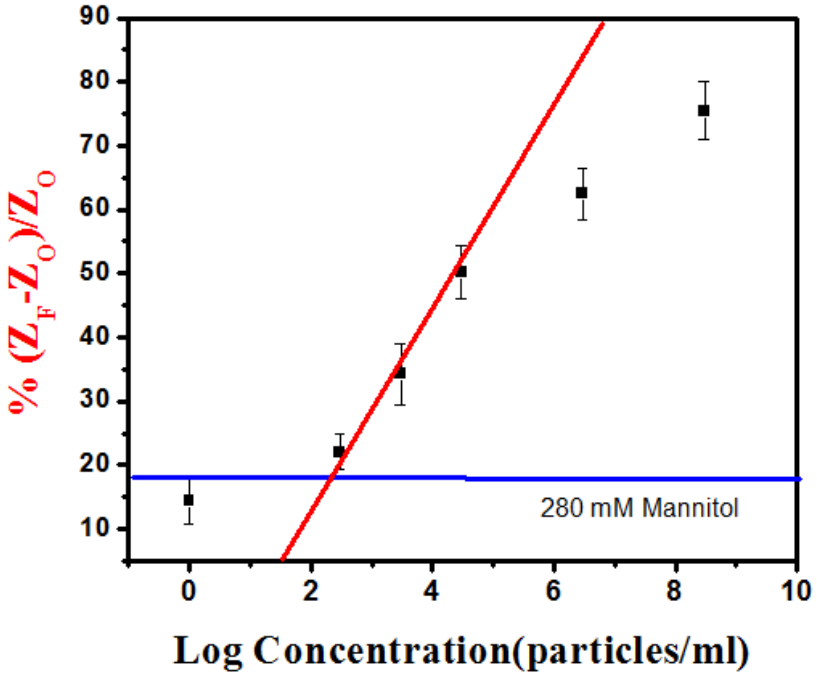


**Figure 6.6: The concentration study with impedance change.**

**The impedance change after 54 sec of pDEP capture of virus solution with the concentration varying from 3.0 × $10^8$ pfu/mL to 3.0 × $10^3$ pfu/mL. 250 mM Mannitol solution without viruses was used as a control sample**.

At this stage, I am interested in the preliminary observation of rupture of the viruses at very high electric field values produced at the tips of VACNFs. In electroporation experiments Propidium Iodide (PI)--a membrane impermeable dye--stains the nucleic acid of *Vaccinia* virus. It was used along with DiO dye that stains the lipophilic membrane of the virus. The working solution of 50 μM DiO dye in DI water was kept at 37 º C for 2 hours in an incubation oven with a 200 μL virus solution to sufficiently stain the lipophilic membrane giving out green fluorescence. For labeling the virus DNA, 50 μl 20.0 μM of Propidium Iodide (PI) aqueous solution was employed. In the intact *Vaccinia* viruses, the DNA dye cannot penetrate inside the cells. Hence, no red fluorescence will be observed. The schematic diagram is shown in Figure 6.7A.

During the experiment, DiO dye-labeled viruses at a concentration of $3.010^6$ pfu/mL in a solution containing PI dye were passed with a velocity of 0.401 mm/sec into a microfluidic chamber. The *Vaccinia* particles were captured in the active region when the voltage was turned to 8.0 $V_{pp}$, with the frequency of 50.0 Hz, and the flow velocity was reduced to 0.05 mm/sec for 60 sec. The high electric field assisted in breaking the lipophilic layer of the virus and extracting nucleic acid DNA into the solution. In Figure 6.7B, the green fluorescence from the DiO dye confirms the capture of the virus at 0.401 mm/sec, 8.0 $V_{pp.}$ As the capture began, the extraction of DNA followed simultaneously, PI dye in solution intercalated with the extracted DNA increasing its fluorescence (~500 folds) giving out intense red fluorescence during the capture

period. The control experiment of 50 µl 20.0 µM of Propidium Iodide (PI) in 280 mM mannitol solution showed absence of fluorescence in the microfluidic channel.

## 6.4 Conclusion

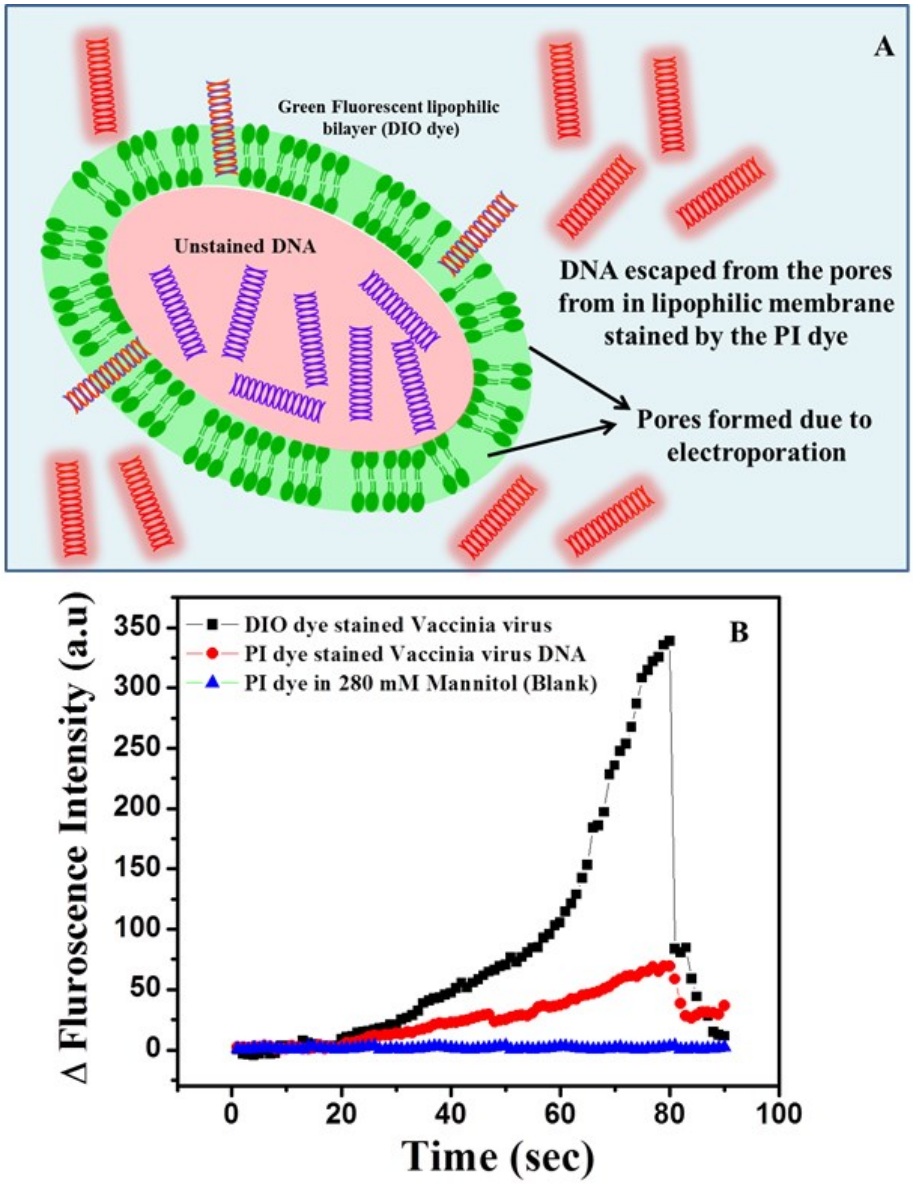


**Figure 6.7: Real-time electroporation of *Vaccinia* virus**

**(A) The *Vaccinia* virus is stained with two fluorophores; DiO dye stains the outer lipophilic membrane and Propidium Iodide (PI) stains the DNA. (B) 3.0 × $10^6$ pfu/mL under flow**

**velocity of 0.401 mm/sec at 8.0 $V_{pp}$ with 50.0 Hz, for 65 sec. During the high voltage application, the flow of the solution was stopped that assists in lysing the virus that is confirmed by the red fluorescence produced by Propidium Iodide (PI) dye intercalated with double-stranded DNA of the virus. 280 mM Mannitol was employed as a blank.**

In conclusion, the successful development of a virus capture and impedance change measurement device using pDEP on VACNF has been demonstrated. The pDEP based on a VACNF NEA acts as an effective and reversible electronic manipulation technique to rapidly concentrate viruses into a micro-area from the solution flowing through the microfluidic channel. Integration of this system to electronically measure the impedance of the viruses is efficient and cost-effective in the detection of virus concentrations in a given sample. The high electric field at the tips of the VACNFs is capable to rupture the lipophilic membrane and extract the DNA. This device with a dual function as a concentrator and DNA extractor can be a prospective device for future downstream processing and testing of biological samples.

# Chapter 7 - Conclusion and Future Outlooks

The goal of this dissertation was to develop rapid diagnostic biosensors with low limits of detection and identification for pathogens using vertically aligned carbon nanofibers (VACNFs). This goal has been achieved through the combined work presented in chapters 4, 5 and 6 using fluorescence, surface enhanced Raman scattering (SERS) and impedance biosensors.

As part of this effort, Chapter 3 described the basic fabrication procedures for VACNFs microfluidic chips. There were two main steps where one need to be cautious during fabrication of the device: the exposure of VACNF tips by reactive ion etching (RIE) which can be monitored by CV and final step bonding the exposed VACNF tips on a silicon wafer with indium tin oxide (ITO) coated glass slide using a vacuum oven to fabricate a microfluidic device. Robust protocols were established to obtain a replicable and consistent microfluidic device.

Chapter 4 discusses the *Bacteriophage* T4r detection on VACNFs using fluorescence measurements. A very different capture profile was observed with *Bacteriophage* T4r compared to a previous study[134] of the *E. coli* bacterial cell. The size *Bacteriophage* T4r is similar to VACNF tips (~100 nm). When captured it displayed unique lightening-like patterns called *Lichtenberg figures*. The lowest concentration of bacteriophage detected was $1 \times 10^4$ pfu/mL.

The identification of specific pathogens using surface enhanced Raman with QSY21 coated nanotags was explored in chapter 5. The complex structure of the nanoovals functionalized with QSY21 and primary antibodies specific to the *E.coli* was used to selectively capture the *E.coli* cells labeled with secondary antibodies from the solution. The detection limit was found to be 210 CFU/mL by portable Raman spectrophotometer. Complex matrix samples of chicken broth, apple juice, and soil solution were used to explore the applications of the device.

Finally, to create a label-free system, electrochemical impedance measurements were performed to detect *Vaccinia* virus, as described in chapter 6. *Vaccinia* virus capture was performed directly on the VACNF tips due to its strong electric field.

The future prospects include the fabrication of SERS biosensors for viruses using VACNFs. We have explored different Raman tags, such as 4-MBA and DSNB with details described below.

## 7.1 Other Schemes of Surface Modification of the Gold Nanoparticles

### *7.1.1 GNP functionalized with 4-MBA*

The functionalization of the gold nanospheres was carried out by the addition of 0.5 mM 4-MBA dissolved in ethanol for 24 h. The solution was spun down at 1000 rpm for 10 min and washed with 1:4 ratio of ethanol and water. The bonding density of MBA was found to be 0.5 nmol/cm$^2$.[189] The enhancement factor calculation of the MBA was done using a confocal Raman microscope at 10 X magnification. The intensity of a 0.5 mM bulk solution in ethanol was 0.1115 and intensity of MBA SERS was found to be 0.4436. One example of the enhancement calculation for QSY21 is shown below:

$$EF = (I_{sers}/I_{bulk}) \times (N_{bulk}/N_{sers}) \quad \text{(7.1)}$$

$$\text{EF} = \frac{671.98}{15.38} \times \frac{0.01 \times 10^6 \left(\frac{nmol}{L}\right) \times \left(\frac{L}{1000mL}\right)}{2.0\,\frac{nmol}{cm^2} \times 6 \times 10^{10} \frac{NPs}{mL} \times 4 \times 3.14 \times (4\,X\,10^{-6})^2 cm^2} \quad \text{(7.2)}$$

**Table 7-1: Calculation scheme and comparison of enhancement factors of 4-MBS, DSNB and QSY 21**

**(F. R. Madiyar et al. unpublished work)**

| Parameters | Explanation | Spheres (30nm) With QSY 21 | Nano ovals (60nm) with QSY 21 | GN Sphere 80nm with DSNB | GN sphere 80 nm with MBA |
|---|---|---|---|---|---|
| $N_{bulk} = C_{bulk}$ | # of molecules sampled in the bulk solution (0.1mM) | 0.1mM | 0.1mM | 0.01mM | 0.5 mM |
| $N_{sers} = D_b C_p 4\pi r^2$ | # of molecules sampled in Nano oval solution $C_p$ =Particle concentration GNPs(6 x $10^{10}$/ml) $D_b$ is boding density 0.5nmol/cm$^2$ | 8.48 x $10^{-1}$ | 3.39 $D_b$ is bonding density **0.5 n mol/cm$^2$** | 24.12 $D_b$ is bonding density for DSNB **2 n mol/cm$^2$** | 1.11 GNPs(1 x $10^{10}$/ml) 0.5 n mol/cm2 x 1.1 x $10^{10}$ NPS/ml x 4 $\pi r^2$ |
| $I_{Bulk}$ | Intensity of Bulk solution | <8.361 cps | <8.361 cps | 15.38 cps | 0.115 |
| $I_{SERS}$ | Intensity of Surface enhanced spectrum | 53.16 cps | 9956.10 cps | 671.98 cps | 0.4226 |
| EF | Enhancement Factor | > 7.5 x $10^{2}$ | > 3.51 x $10^{4}$ | 1.81 x $10^{1}$ | 1.66 x $10^{3}$ |

### *7.1.2 GNP functionalized with DSNB*

5, 5′-dithiobis (succinimidyl-2-nitrobenzoate) (DSNB) was selected for this study because the literature showed the successful use of the bifunctional chemical. DSNB can be used for immobilizing antibodies on the surface of nanoparticles as well as $NO_2$ functional groups act as a Raman marker.

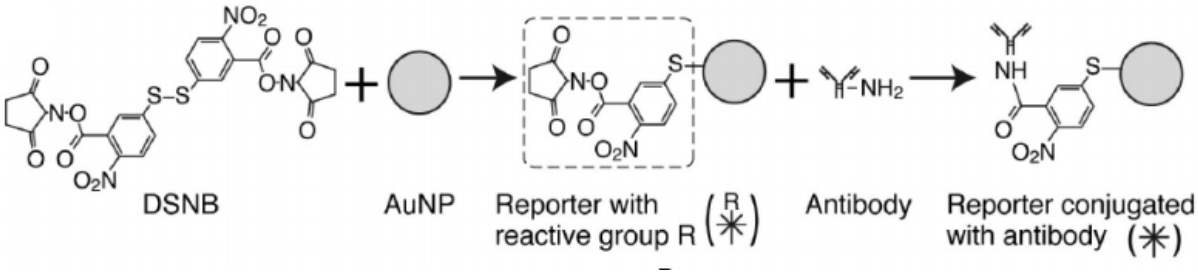


**Figure 7.1: Scheme for attaching Raman marker onto the gold nanoparticles.**

**For attaching DSNB to gold nanoparticles and attachment with an antibody. (Reprinted with permission from Shiv K. Sharma, University of Hawaii Systems, Office of Research Services Honolulu, HI 96822 2010.)**

The protocol (illustrated in Figure 7.1) has been developed for using SERS-based immunoassay using gold nanoparticle probe for femtomolar detection of Prostate Specific Antigen (PSA) by Grubisha, et al.[190] DSNB was used as the bifunctional Raman marker to connect the gold nanoparticles (32 nm) to the monoclonal antibodies to PSA.

This scheme was explored for detection of viruses in the microfluidic device using DSNB.

#### *7.1.2.1 Synthesis of DSNB*

DSNB (5,5′-dithiobis (succinimidyl-2-nitrobenzoate)) synthesis was carried out as previously described.[191] Briefly, 0.50 g of 5, 5′-dithiobis (2-nitrobenzoic acid) (DNBA), 0.52 g of 1, 3-dicyclohexylcarbodiimide (DCCD), and 0.29 g of N-hydroxysuccinimide (NHS) were sequentially added to 50 mL tetrahydrofuran in a 500 mL round-bottom flask equipped with a drying tube. After magnetic stirring for 24 hours at room temperature, the solution was filtered and then roto evaporated to remove the solvent. The product was then recrystallized as a yellow powder with acetone/hexane solvent. Figure 7.2A shows the Raman spectra of DSNB solid, in acetonitrile (ACN) and on 60 nm gold nanoparticles indicating 1347 $cm^{-1}$ is highest peak. The powder spectrum is dominated by ($NO_2$) at 1341 $cm^{-1}$. Other strong bands in the spectrum are at 1568 $cm^{-1}$ (assigned to an aromatic ring mode) and at 1066 $cm^{-1}$ (a succinimidyl N–C–O stretch overlapping with aromatic ring modes). The Raman spectrum matches that reported in the literature by Poter, M., et al.[146] Figure 7.2B shows the acetonitrile itself has a peak at 1349 $cm^{-1}$

which can interfere with the DSNB Raman signal. We still need to consider the enhancement factor (EF) of DSNB that is given in table 7.1

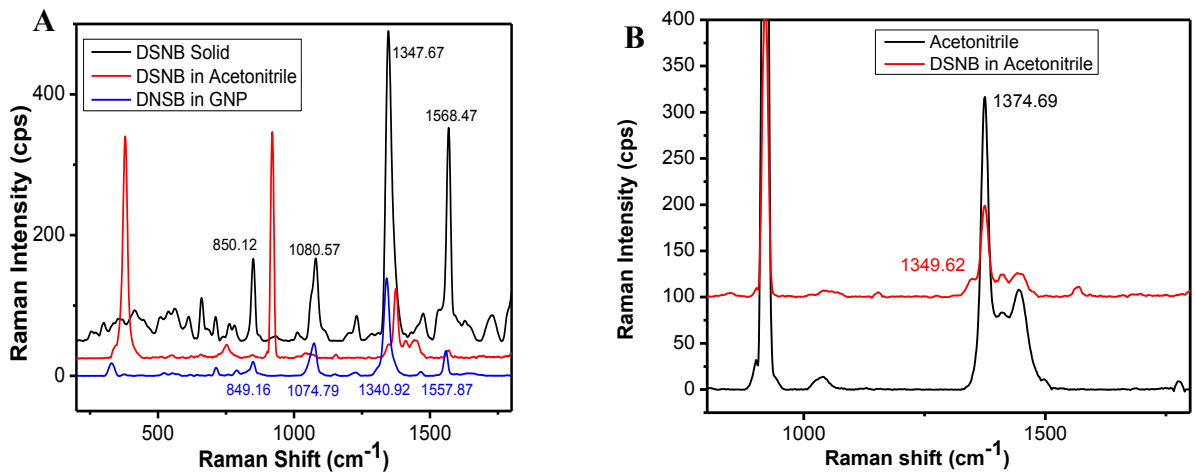


**Figure 7.2: Raman spectrum of DSNB in solid form, in acetonitrile solution and DSNB functionalized on gold.**

**(A) The Raman spectra of DSNB solid (black line) DSNB in acetonitrile (red) and DSNB attached to gold nanoparticles (blue). (B) A close-up of the Raman spectra of Acetonitrile liquid (black) and DSNB in acetonitrile (red) showing 1374 $cm^{-1}$ peak present in both chemicals. (F. R. Madiyar et al. unpublished work)**

### *7.1.3 pH effects on Functionalization of Gold Nanoparticles to the Bacteria*

DSNB (5,5′-dithiobis (succinimidyl-2-nitrobenzoate)) is useful because it has an aromatic $NO_2$ group that has intrinsically high Raman scattering cross section due to symmetric stretching of the $NO_2$ group. DSNB attaches to the gold nanoparticles readily due to disulfide moiety and thiolate adhered layer. The succinimidyl group is used to bind covalently the primary amine on the antibody.

#### *7.1.3.1 Procedure for attaching bacteria to gold nanoparticle using DSNB*

Frozen *E. coli* DHα 5 stock was thawed and grown in LB medium in a sterile culture tube and incubated overnight at 37˚ C to reach a cell concentration of $2.5 \times 10^9$ CFU/mL. The cells were centrifuged at 5000 rpm for 5 min, the supernatant LB media was discarded and the pellet was resuspended and washed in 1.0 mL 1X PBS thrice to eliminate the remaining ingredients of the LB media. The bacteria solution of $2.5 \times 10^9$ CFU/mL was incubated with 50 µl FITC conjugated rabbit anti- E. coli Ab (AbD Serotech, Raleigh NC, USA) at 330 µg/mL for 1 h at 4˚ C. The cells were then centrifuged, washed with deionized (DI) water and diluted to a final concentration of $9.5 \times 10^4$ CFU/mL.

#### *7.1.3.2 Preparation of gold nanoparticles with DSNB and secondary antibody*

The procedure followed to attach DSNB (5,5′-dithiobis (succinimidyl-2-nitrobenzoate)) to bacteria was elaborated given in Yakes.B., et al.[192] Briefly, 10 µl of 0.1 mM solution of DNSB in acetonitrile was mixed with 1.0 mL 60 nm gold nanoparticles for 8 hours at room temperature (28ºC). The solution was centrifuged at 8000 rpm to remove the extra DSNB molecules, and the secondary antibody (Alexa 555 conjugated goat anti-rabbit secondary antibody) was added into the solution for 14 hours. To block the sites, 100 µl of 10% BSA was added to the mixture for 7 hours in 2 mM Borate buffer. After the reaction was completed, a solution with gold nanoparticle, DSNB, and antibody, was spun down and resuspended in borate buffer with 1 µl of 1% BSA in 1000 µl borate buffer. 50 µl DSNB and antibody-coated nanoparticles ($6 \times 10^{10}$ particles/mL) was added to 100 µl of bacteria solution to observe the attachment of the nanoparticles to bacteria. Figure 7.3 shows the transmission electron microscope image after this procedure. It is not convincing from the image that the gold

nanoparticles have attached to the bacteria due to antigen – antibody reaction or capillary forces when drying.

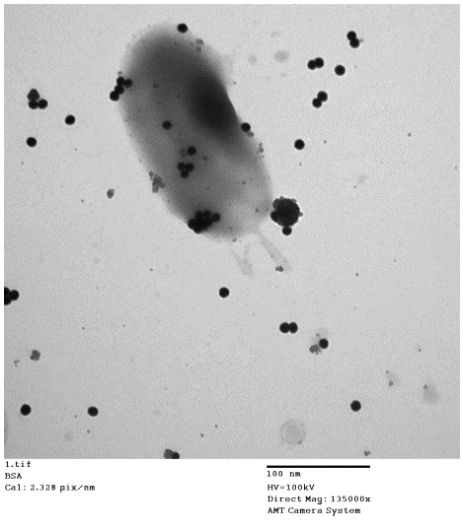


**Figure 7.3: Attachment of DSNB coated 60 nm Gold nanoparticle onto a bacterial cell. (F. R. Madiyar et al. unpublished work).**

So to confirm that the conditions used in the procedures were correct, we attached nanoparticles to 1.0 μm latex particles using the same procedure. It is known that the succinimidyl group is active in the buffer of pH 9.0 for approximately 10 min.[193]

For this experiment, latex beads coated with primary amine groups were purchased from the Sigma Alrich (St. Louis, MO). To attach DSNB to gold nanoparticles, the above procedure was followed. 1 mL of GNP 60 nm was mixed 40 μl of 50 mM borate buffer (pH 8.3) and 10 μl of 0.1 mM DSNB in ACN for 10 min. Then the solution was centrifuged for 5000 rpm for 4 min to remove the extra DSNB molecules and 20 μl of amine coated latex beads ($5 \times 10^{10}$ particles/ mL). Other pH values used were 9 and 9.5. The transmission emission microscope images revealed that when the reaction was carried out in solution of pH 8.5 (Figure 7.4A) no

attachment occurred, in a pH 9.0 solution (Figure 7.4B) some attachment was seen, and in a pH 9.5 solution (Figure 7.4C) attachment was greatest.

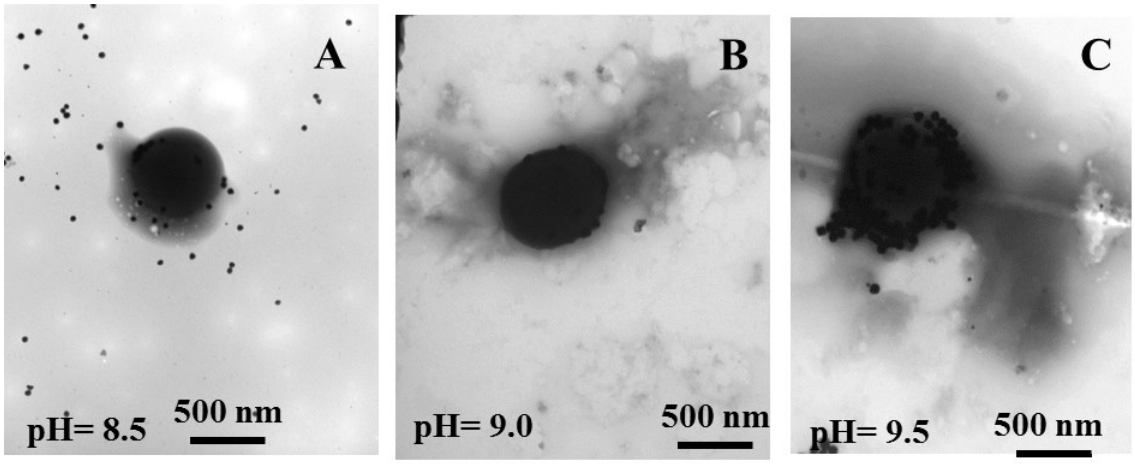


**Figure 7.4: Assessing attachment of gold nanoparticles (60 nm) coated with DSNB to latex beads at different pH.**

**(A) pH 8.5 (B) pH 9.0 (C) pH 9.5 (F. R. Madiyar et al. unpublished work).**

These results set the baseline from which to choose the conditions for bonding primary antibody to the succinimidyl group at pH 9.5. When comparing the enhancement factor of DSNB to QSY21 from Table 7.1(page 129), DSNB has enhancement factor of $1.81 \times 10^{1}$ as compared to QSY21 which has an enhancement factor of $>3.51 \times 10^{4}$. As the enhancement factor of DSNB is lower than QSY21, in future experiments QSY21 will be explored for SERS detection of viruses in the dielectrophoretic scheme in a microfluidic device.

## 7.2 Integrated Micro-Total Analysis Systems

In the past five years (2010-2015) the level of integration of microfluidic devices has increased considerably for pathogen detection.[194, 195] The reason is that chemical analysis on the

nanoliter scale is well suited for five research in the life sciences sector, where there is increased interest in the chemical profile of low-abundance cellular material DNA (genomics),[196] RNA (transcriptomics),[197] proteins (proteomics),[198] metabolites (metabolomics),[199] and lipids (lipidomics).[200] The principal advantage of microfluidic integration is that the miniaturized architecture that allows for dilution and minimized loss of the sample.[201] In addition, contamination becomes negligible because the sample remains in the chip for the entire duration of the experiment instead of being transferred between bench top instruments.[202-204] The ideal micro-total analysis system is one that incorporates every aspect of a quantitative analysis; sample preparation (e.g. cell sorting, extraction, reagent metering, mixing, reactions, purification, preconcentration), sampling, eliminating interferences (separation techniques) and detection.[205-208]

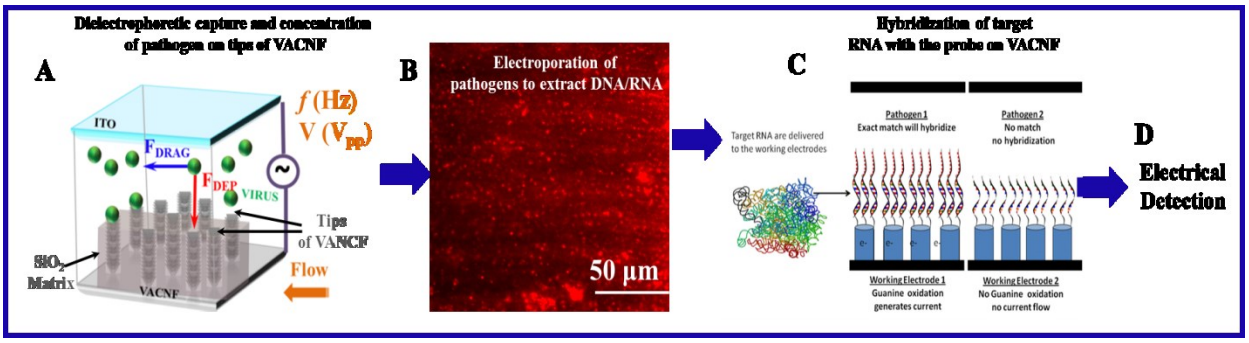


**Figure 7.5: Schematic for an explanation of nucleic acid electrochemical biosensor integrated with dielectrophoresis.**

**(A) Schematic of the dielectrophoresis to capture the particles on tips of VACNF due to the high electric field ($F_{DEP}$). (B) Snapshot of virus capture and electroporation of virus labeled with propidium iodide dye. (C) Schematic of the nucleic acid electrochemical biosensor, in which the probe is functionalized on the tips of VACNF. When the voltage of 1.05 V is applied to the working electrode guanine (probe) and cytosine bases from RNA/ DNA**

**(pathogens) hybridized when there is an exact match. This causes a flow of electrons to the designated working electrode. (Reprinted with permission from http://www.earlywarninginc.com/technologies.php)**

For pathogen detection to be rapid and reliable, the combination of dielectrophoresis and nucleic acid electrochemical biosensors in one chip design can be employed. Dielectrophoresis can be used for capture, separation and electroporation of the pathogens and extract the nucleic acids (Figure 7.5 A and B). Early Warning Inc. developed the identification of pathogen by DNA on VACNF scheme.

In which, DNA and RNA was used as nucleic acid receptors. Guanine is natural constituent of DNA and RNA. The sensor takes advantage of guanine's oxidation activity at 1.05 volts and aids in electrochemical signal transduction. This scheme has been explored by Early Warning Inc. and the working principle is described below.

The VACNF can be used as working electrode and its tips can be chemical functionalized with DNA (single stranded) bioprobes that contain 30 or more base sequences that make them extremely specific for the particular pathogen or individual species such as *E.coli* O157:H7 (Figure 7.5C). When the single strands of RNA from the sample (pathogens) approaches to contact the bioprobes, only complementary strands hybridize to form double helixes. After the hybridization of the strands take place, 1.05 volts is applied across the electrodes. The current signal is observed and recorded only when guanine reacts with cytosine during hybridization. The magnitude of the electrical current is related to the amount of RNA in the sample and subsequently to the concentration of the pathogen in the sample. If there is no hybridization from the absence of the target pathogen, absence of current signal is observed.[209] This scheme is

schematically shown in Figure 7.5. When guanine oxidizes after hybridization, the flow of electrons is extremely low making the resulting electrical current difficult to measure. A Ruthenium bipyridine mediator which also oxidizes at 1.05 volts can amplify the signal by transferring guanine electrons to the electrode surface and improving the measurement accuracy.[210-212] Both guanine and Ruthenium bipyridine lose electrons through oxidization when electrical potential voltage is applied. When the voltage scan is reversed, Ruthenium bipyridine will regain its electrons but guanine will not. As a Ruthenium bipyridine can oxidize and reduce repeatedly and form a baseline to measure the incremental current from guanine alone. The electrical current from Guanine and Ruthenium bipyridine combined in a first scan is much greater than Guanine alone which needs to be distinguished from the background noise for the presence/absence detection threshold.[208] Further studies are required for integration of VACNF in a microfluidic channel with the DNA hybridization for pathogen detection.

# References


1. R. M. Anderson and R. M. May, *Infectious diseases of humans: Dynamics and control*, New York: Oxford University Press, 1992.
2. O. Lazcka, F. J. D. Campo and F. X. Muñoz, Pathogen detection: A perspective of traditional methods and biosensors. *Biosens. Bioelectron.*, **2007**, 22, 1205-1217.
3. R. S. Quilliam, A. P. Williams, L. M. Avery, S. K. Malham and D. L. Jones, Unearthing human pathogens at the agricultural–environment interface: A review of current methods for the detection of *Escherichia coli* O157 in freshwater ecosystems. *Agric Ecosyst Environ*, **2011**, 140, 354-360.
4. D. Y. C. Fung, Rapid Methods and Automation in Microbiology. *Comprehenhive reviews in food science and food safety* **2002**, 1.
5. CDC, Waterborne, and Environmental Diseases.
6. CDC, Estimates of Foodborne Illness in the United States.
7. http://www.cdc.gov/foodsafety/, Food Safety
8. F. Register, DEPARTMENT OF AGRICULTURE, 1996, vol. 61.
9. P. S. Mead, L. Slutsker, V. Dietz, L. F. McCaig, J. S. Bresee, C. Shapiro, P. M. Griffin and R. V. Tauxe, Food-related illness and death in the United States. *Emerging Infectious Diseases*, **1999**, 5, 607-625.
10. M. Tietjen and D. Y. C. Fung, *Salmonellae* and Food Safety. *Crit Rev Microbiol*, **1995**, 21, 53-83.
11. E. Leoni and P. P. Legnani, Comparison of selective procedures for isolation and enumeration of Legionella species from hot water systems. *J. Appl. Microbiol.*, **2001**, 90, 27-33.

12. M. F. Clark and A. N. Adams, Characteristics of the Microplate Method of Enzyme-Linked Immunosorbent Assay for the Detection of Plant Viruses. *J. Gen. Virol.*, **1977**, 34, 475-483.

13. A. M. Sewell, D. W. Warburton, A. Boville, E. F.Daley and K. Mullen, The development of an efficient and rapid enzyme linked fluorescent assay method for the detection of *Listeria spp*. from foods. *Int. J. Food. Microbiol.*, **2003**, 81, 123-129.

14. V. M. Bohaychuk, G. E. Gensler, R. K. King, J. T. Wu and L. M. McMullen, Evaluation of Detection Methods for Screening Meat and Poultry Products for the Presence of Foodborne Pathogens. *J. Food Prot.*, **2005**, 12, 2502-2720.

15. A. K. Bej, M. H. Mahbubani, J. L. Dicesare and R. M. Atlas, Polymerase chain reaction-gene probe detection of microorganisms by using filter-concentrated samples. *Applied Microbiology*, **1991**, 57, 3529-3534.

16. K. Mullis, F. Faloona, S. Scharf, R. Saiki, G. Horn and H. Erlich, Specific Enzymatic Amplification of DNA In Vitro: The Polymerase Chain Reaction. *Cold Spring Harbor Symposia on Quantitative Biology*, **1986**, 51, 263-273.

17. K. B. Mullis and M. Smith, in *Nobel Lectures*, World Scientific Publishing Co., 1997 edn., **1993**.

18. E. H. W and K. Wachsmuth, The polymerase chain reaction: Applications for the detection of foodborne pathogens. *Critical Reviews in Food Science and Nutrition*, **1996**, 36, 123-173.

19. R. K. Saiki, D. H. Gelfand, S. Stoffel, S. J. Scharf, R. Higuchi, G. T. Horn, K. B. Mullis and H. A. Erlich, Primer-directed enzymatic amplification of DNA with a thermostable DNA polymerase. *Science*, **1988**, 239, 487-491.

20. K. B. Mullis and M. Smith, The Unusual Origin of the Polymerase Chain Reaction. *Sci. Am.*, **1990**, 56-65.

21. D. Rodríguez-Lázaro, M. D'Agostino, A. Herrewegh, M. Pla, N. Cook and J. Ikonomopoulos, Real-time PCR-based methods for detection of *Mycobacterium avium subsp. paratuberculosis* in water and milk. *Int. J. Food. Microbiol.*, **2005**, 101, 93-104.

22. M. Zourob, S. Elwary and A. Turner, *Principles of Bacterial Detection: Biosensors, Recognition Receptors and Microsystems*, Springer New York, **2008**.

23. S. Ko and S. A. Grant, Development of a novel FRET method for detection of *Listeria* or *Salmonella*. *Sens. Actuator B-Chem.*, **2003**, 96, 372-378.

24. F. Lucarelli, F. G. Marrazza, A. P. F. Turner and M. Mascini, Carbon and gold electrodes as electrochemical transducers for DNA hybridisation sensors. *Biosens. Bioelectron.*, **2004**, 19, 515-530.

25. J. P. Chambers, B. P. Arulanandam, L. L. Matta, A. Weis and J. J. Valdes, Biosensor Recognition Elements. *Curr. Issues Mol. Biol.*, **2008**, 10, 1–12.

26. A. Touhami, in *Nanomedicine*, **2012**, pp. 374-403.

27. A. F. Collings and F. Caruso, Biosensors: Recent Advances. *Rep. Prog. Phys.*, **1997**, 60, 1397–1445.

28. M. Mehrvar, C. Bis, J. M. Scharer, M. M. Young and J. H. Luong., Fiber-Optic Biosensors-Trends and Advances. *Anal. Sci.*, **2000**, 16, 677-692.

29. F. Long, A. Zhu and H. Shi, Recent Advances in Optical Biosensors for Environmental Monitoring and Early Warning *Sensors*, **2013**, 13.

30. D. Dey and T. Goswami, Optical Biosensors: A Revolution Towards Quantum Nanoscale Electronics Device Fabrication. *J. Biomed. Biotechnol.*, **2011**, 2011.

31. X. Lu and B. Rasco, in *Handbook of Vibrational Spectroscopy*, John Wiley & Sons, Ltd, 2006.

32. A. Alvarez-Ordóñez, D. J. M. Mouwen, M. López and M. Prieto, Fourier transform infrared spectroscopy as a tool to characterize molecular composition and stress response in foodborne pathogenic bacteria. *J. Microbiol. Methods*, **2011**, 84, 369-378.

33. R. Davis, Y. Burgula, A. Deering, J. Irudayaraj, B.L. Reuhs and L. J. Mauer, Detection and differentiation of live and heat-treated *Salmonella enterica* serovars inoculated onto chicken breast using Fourier transform infrared (FT-IR) spectroscopy. *J. Appl. Microbiol.*, **2010**, 109, 2019-2013.

34. S. Meisel, S. Stöckel, M. Elschner, F. Melzer, P. Rösch and J. Popp, Raman Spectroscopy as a Potential Tool for Detection of Brucella spp. in Milk. *Appl. Environ. Microbiol.*, **2012**, 78, 5575-5583.

35. Y. Xie, L. Xu, Y. Wang, J. Shao, L. Wang, H. Wang, H. Qian and W. Yao, Label-free detection of the foodborne pathogens of Enterobacteriaceae by surface-enhanced Raman spectroscopy. *Anal. Methods*, **2013**, 5, 946-952.

36. A. Tripathi, R. E. Jabbour, P. J. Treado, J. H. Neiss, M. P. Nelson, J. L. Jensen and A. P. Snyder, Waterborne Pathogen Detection Using Raman Spectroscopy. *Appl. Spectrosc.*, **2008** 62, 4A-27A.

37. A. Sengupta, M. Mujacic and E. J. Davis, Detection of bacteria by surface-enhanced Raman spectroscopy. *Anal. Bioanal. Chem.*, **2006**, 386, 1379-1386.

38. H. Chu, Y. Huang and Y. Zhao, Silver Nanorod Arrays as a Surface-Enhanced Raman Scattering Substrate for Foodborne Pathogenic Bacteria Detection. *Appl. Spectrosc.*, **2008**, 62, 84A-204A and 833-935.

39. C. Yu, J. Irudayaraj, C. Debroy, Z. Schmilovtich and A. Mizrach, Spectroscopic Differentiation and Quantification of Microorganisms in Apple Juice. *J. Food Sci.*, **2004**, 69, 268-272.

40. M. Lin, M. Al-Holy, S-S. Chang, Y. Huang, A. G. Cavinato, D-H. Kang and B. A. Rasco, Rapid discrimination of Alicyclobacillus strains in apple juice by Fourier transform infrared spectroscopy. *Int. J. Food. Microbiol.*, **2005**, 105, 369-376.

41. R. M. Hochstrasser, New aspects of Raman scattering. *Nature*, **1988**, 336, 621-622.

42. C. V. Raman and K. S. Krishanan, A new type of secondary radiation. *Nature* **1928**, 121, 501-502.

43. Z. Schmilovitch, A. Mizrach, V. Alchanatis, G. Kritzman, R. Kororic, J. Irudayaraj and C. Debroy, Detection of bacteria with low-resolution Raman spectroscopy. *Future Microbiol.*, **2005**, 1843-1850.

44. I. Abdulhalim, M. Zourob and A. Lakhtakia, Surface Plasmon Resonance for Biosensing: A Mini-Review. *Electromagnetics*, **2008**, 28, 214-242.

45. P. Leonard, S. Hearty, J. Brennan, L. Dunne, J. Quinn, T. Chakraborty and R. O'Kennedy, Advances in biosensors for detection of pathogens in food and water. *Enzyme Microb. Technol.*, **2003**, 32, 3-13.

46. J. S. Daniels and N. Pourmand, Label-Free Impedance Biosensors: Opportunities and Challenges. *Electroanalysis*, **2007**, 19, 1239–1257.

47. I. I. Suni, Impedance methods for electrochemical sensors using nanomaterials. *Trends in Analytical Chemistry*, **2008**, 27.

48. Y. Wang, Z. Ye and Y. Ying, New Trends in Impedimetric Biosensors for the Detection of Foodborne Pathogenic Bacteria. *Sensors*, **2012**, 12, 3449–3471.

49. L. Yang and R. Bashir, Electrical/electrochemical impedance for rapid detection of foodborne pathogenic bacteria. *Biotechnology Advances* **2008**, 26, 135-150.

50. H. J. Chung, C. M. Castro, H. Im, H. Lee and R. Weissleder, A magneto-DNA nanoparticle system for rapid detection and phenotyping of bacteria. *Nat. Nano.*, **2013**, 8, 369-375.

51. P. Srivastava, S. Pandey, M. K. M. Aslam, P. Singh and K. P. Singh, Nanobiosensors: Diagnostic Tool for Pathogen Detection. *Int. J. Biol. Sci.*, **2013**, Vol. 2, 76-78.

52. P. J. Vikesland and K. R. Wigginton, Nanomaterial Enabled Biosensors for Pathogen Monitoring - A Review. *Environ. Sci. Technol.*, **2010**, 44, 3656-3669.

53. E. Petryayeva and J. U. Krull, Localized surface plasmon resonance: Nanostructures, bioassays and biosensing—A review. *Anal. Chim. Acta*, **2011**, 706, 8-24.

54. C. Wang and J. Irudayaraj, Gold Nanorod Probes for the Detection of Multiple Pathogens. *Small*, **2008**, 4, 2204-2208.

55. U.Tamer, D. Cetin, Z. Suludere, I. H. Boyaci, H. T.Temiz, H. Yegenoglu, P. Daniel, İ. Dinçer and Y. Elerman, Gold-Coated Iron Composite Nanospheres Targeted the Detection of *Escherichia coli*. *Int. J. Mol. Sci.*, **2013**, 14, 6223–6240.

56. Z. Fan, D. Senapati, S. A. Khan, A. K. Singh, A. Hamme, B. Yust, D. Sardar and P. C. Ray, Popcorn-Shaped Magnetic Core–Plasmonic Shell Multifunctional Nanoparticles for the Targeted Magnetic Separation and Enrichment, Label-Free SERS Imaging, and Photothermal Destruction of Multidrug-Resistant Bacteria. *Chem. Eur. J.*, **2013**, 19, 2839-2847.

57. L. Minati, B. Benetti, A. Chiappini and G. Speranza, One-step synthesis of star-shaped gold nanoparticles. *Colloids Surf.*, **2014**, 441, 623-628.

58. M. Fleischmann, P. J. Hendra and A. J. McQuillan, Raman spectra of pyridine adsorbed at a silver electrode. *Chem. Phys. Lett.*, **1974**, 26, 163-166.

59. D. L. Jeanmaire and R. P. VanDuyne, Surface Raman electrochemistry. Part 1. Heterocyclic, aromatic and aliphatic amines adsorbed on the anodised silver electrode. *J. Electroanal. Chem.*, **1977**, 84.

60. B. Sharma, R. R. Frontiera, A-I. Henry, E. Ringe and R. P. VanDuyne, SERS: Materials, applications, and the future. *Materials Today*, **2012**, 15, 16-25.

61. E. Ringe, B. Sharma, A-I. Henry, L. D. Marks and R. P. VanDuyne, Single nanoparticle plasmonics. *Phys. Chem. Chem. Phys.*, **2013**, 15, 4110-4129.

62. P. C. Ray, S. A. Khan, F. Zhen and S. Dulal, in *Advances in Applied Nanotechnology for Agriculture*, American Chemical Society, 2013, vol. 1143, ch. 1, pp. 1-19.

63. M. E. Stewart, C. R. Anderton, L. B. Thompson, J. Maria, S. K. Gray, J. A. Rogers and R. G. Nuzzo, Nanostructured Plasmonic Sensors. *Chem. Rev.*, **2008**, 108, 494-521.

64. W. R. Premasiri, D. T. Moir, M. S. Klempner, N. Krieger, G. Jones and L. D. Ziegler, Characterization of the Surface Enhanced Raman Scattering (SERS) of Bacteria. *J. Phys. Chem. B*, **2005**, 109, 312-320.

65. R. M. Jarvis and R. Goodacre, Discrimination of Bacteria Using Surface-Enhanced Raman Spectroscopy. *Anal. Chem.* , **2003**, 76, 40-47.

66. D. R. Albrecht, R. L. Sah and S. N. Bhatia, Geometric and Material Determinants of Patterning Efficiency by Dielectrophoresis. *Biophys J.*, **2004**, 87, 2131–2147.

67. S. Tsukahara, K. Yamanaka and H. Watarai, Flow fractionation of microparticles under a dielectrophoretic field in a quadrupole electrode capillary. *Anal Chem.*, **2001**, 73, 5661-5668.

68. G. Fuhr, H. Glasser, T. Müller and T. Schnelle, Cell manipulation and cultivation under a.c. electric field influence in highly conductive culture media. *Biochim. Biophys. Acta*, **1994**, 1201, 353-360.

69. S. N. Ibrahim and M. M. Alkaisi, The octupole microelectrode for dielectrophoretic trapping of single cells-design and simulation, **2012**.

70. T. Schnelle, R. Hagedorn, G. Fuhr, S. Fiedler and T. Müller, Three-dimensional electric field traps for manipulation of cells--calculation and experimental verification. *Biochim. Biophys. Acta*, **1993**, 1157, 127-140.

71. B. M. Taff and J. Voldman, A Scalable Addressable Positive-Dielectrophoretic Cell-Sorting Array. *Anal. Chem.*, **2005**, 77, 7976-7983.

72. D. S. Gray, J. L. Tan, J. Voldman and C. S. Chen, Dielectrophoretic registration of living cells to a microelectrode array. *Biosens. Bioelectron.*, **2004**, 19, 1765-1774.

73. F. H. Labeed and H. O. Fatoyinbo, *Microfluidics in Detection Science*, Royal Society of Chemistry, 2014.

74. J. Voldman, Electrical forces for microscale cell manipulation. *Annu. Rev. Biomed. Eng.*, **2006**, 8, 425-454.

75. K. Khoshmanesh, S. Nahavandi, S. Baratchi, A. Mitchell and K. Kalantar-zadeh, Dielectrophoretic platforms for bio-microfluidic systems. *Biosens. Bioelectron.*, **2011**, 26, 1800-1814.

76. I. Fang Cheng, H-C. Chang, T-Y. Chen, C. Hu and F.-L. Yang, Rapid (<5[emsp14]min) Identification of Pathogen in Human Blood by Electrokinetic Concentration and Surface-Enhanced Raman Spectroscopy. *Sci. Rep.*, **2013**, 3.

77. A. F. Chrimes, K. Khoshmanesh, P. R. Stoddart, A. Mitchell and K. Kalantar-zadeh, Microfluidics and Raman microscopy: current applications and future challenges. *Chem. Soc. Rev.*, **2013**, 42, 5880-5906.

78. A. Bogomolova, E. Komarova, K. Reber, T. Gerasimov, O. Yavuz, S. Bhatt and M. Aldissi, Challenges of Electrochemical Impedance Spectroscopy in Protein Biosensing. *Anal. Chem.*, **2009**, 81, 3944-3949.

79. D. Grieshaber, R. MacKenzie, J. Vörös and E. Reimhult, Electrochemical Biosensors - Sensor Principles and Architectures. *Sensors*, **2008**, 8, 1400-1458.

80. S. Flint, A. Naila and R. Bashir, in *High Throughput Screening for Food Safety Assessment*, eds. A. K. Bhunia, M. S. Kim and C. R. Taitt, Woodhead Publishing, 2015, pp. 285-300.

81. M. Varshney and Y. Li, Interdigitated array microelectrodes based impedance biosensors for detection of bacterial cells. *Biosens. Bioelectron.*, **2009**, 24, 2951-2960.

82. S. M. Radke and E. C. Alocilja, A high density microelectrode array biosensor for detection of E. coli O157:H7. *Biosens. Bioelectron.*, **2005**, 20, 1662-1667.

83. S. M. Radke and E. C. Alocilja, A microfabricated biosensor for detecting foodborne bioterrorism agents. *Sensors J.*, **2005**, 5, 744-750.

84. L. Yang and Y. Li, AFM and impedance spectroscopy characterization of the immobilization of antibodies on indium–tin oxide electrode through self-assembled monolayer of epoxysilane and their capture of *Escherichia coli* O157:H7. *Biosens. Bioelectron.*, **2005**, 20, 1407-1416.

85. L.Yang, Y. Li and G. F. Erf, Interdigitated Array Microelectrode-Based Electrochemical Impedance Immunosensor for Detection of *Escherichia coli* O157:H7. *Anal. Chem.*, **2004**, 76, 1107-1113.

86. F. Patolsky, M. Zayats, E. Katz and I. Willner, Precipitation of an Insoluble Product on Enzyme Monolayer Electrodes for Biosensor Applications: Characterization by Faradaic Impedance Spectroscopy, Cyclic Voltammetry, and Microgravimetric Quartz Crystal Microbalance Analyses. *Anal. Chem.*, **1999**, 71, 3171-3180.

87. B. C.Towe and V. B. Pizziconi, A microflow amperometric glucose biosensor. *Biosens. Bioelectron.*, **1997**, 12, 893-899.

88. C. Berggren, B. Bjarnason and C. Johansson, An immunological interleukine-6 capacitive biosensor using perturbation with a potentiostatic step. *Biosens. Bioelectron.*, **1998**, 13, 1061-1068.

89. Y. Li and X.-L. Su, Microfluidics -based optical biosensing method for rapid detection of *Escherichia coli* O157:H7 *J. Rapid. Methods. Autom. Microbiol.* , **2006**, 14, 96-109.

90. S. M. Radke and E. C. Alocilja, Design and fabrication of a microimpedance biosensor for bacterial detection. *Sensors J.*, **2004**, 4, 434-440.

91. M. Varshney, Y. Li, B. Srinivasan and S.Tung, A label-free, microfluidics and interdigitated array microelectrode-based impedance biosensor in combination with nanoparticles immunoseparation for detection of Escherichia coli O157:H7 in food samples. *Sens. Actuator B-Chem.*, **2007**, 128, 99-107.

92. R. Gómez-Sjöberg, D. T. Morisette and R. Bashir, Impedance microbiology-on-a-chip: Microfluidic bioprocessor for rapid detection of bacterial metabolism. *J. Microelectromech. Syst.*, **2005**, 14, 829-838.

93. J. Suehiro, R.Yatsunami, R. Hamada and M. Hara, Quantitative estimation of biological cell concentration suspended in aqueous medium by using dielectrophoretic impedance measurement method. *J. Phys. D. Appl. Phys.*, **1999**, 32, 2814-2820.

94. J. Suehiro, D. Noutomi, R. Hamada and M. Hara, Selective detection of bacteria using dielectrophoretic impedance measurement method combined with antigen-antibody reaction, **2001**.

95. J. Suehiro, A. Ohtsubo, T. Hatano and M. Hara, Selective detection of bacteria by a dielectrophoretic impedance measurement method using an antibody-immobilized electrode chip. *Sens. Actuator B-Chem.*, **2006**, 119, 319-326.

96. L. Yang, P. P. Banada, M. R. Chatni, K. Seop Lim, A. K. Bhunia, M. Ladisch and R. Bashir, A multifunctional micro-fluidic system for dielectrophoretic concentration coupled with immuno-capture of low numbers of *Listeria monocytogenes*. *Lab Chip*, **2006**, 6, 896-905.

97. Y-H. Su, M. Tsegaye, W. Varhue, K-T. Liao, L. S. Abebe, J. A. Smith, R. L. Guerrant and N. S. Swami, Quantitative dielectrophoretic tracking for characterization and separation of persistent subpopulations of Cryptosporidium parvum. *Analyst*, **2014**, 139, 66-73.

98. D. J. Bakewell, in *Encyclopedia of Nanotechnology*, ed. B. Bhushan, Springer Netherlands, 2012, ch. 132, pp. 543-559.

99. V. Vamvakaki, K.Tsagaraki and N. Chaniotakis, Carbon Nanofiber-Based Glucose Biosensor. *Anal. Chem.*, **2006**, 78, 5538-5542.

100. S.-U. Kim and K.-H.Lee, Carbon Nanofiber Composites for the Electrodes of Electrochemical Capacitors. *Chem. Phys. Lett.* , **2004**, 400 (1–3), 253-257.

101. J. Koehne, H. Chen, J. Li, A. M. Cassell, Q. Ye, H.T. Ng, J. Han and M. Meyyappan, Ultrasensitive label-free DNA analysis using an electronic chip based on carbon nanotube nanoelectrode arrays. *Nanotechnology* **2003**, 14, 1239-1245.

102. J. E. Koehne, H. Chen, A. M. Cassell, Q. Ye, J. Han, M. Meyyappan and J. Li, Miniaturized Multiplex Label-Free Electronic Chip for Rapid Nucleic Acid Analysis Based on Carbon Nanotube Nanoelectrode Arrays. *Clinic. Chem. Phys. Lett.*, **2004**, 50, 1886-1893.

103. J. Li, H. T. Ng, A. Cassell, W. Fan, H. Chen, Q. Ye, J. Koehne, J. Han and M. Meyyappan, Bottom-up Sample Preparation Technique for Interfacial Characterization of Vertically Aligned Carbon Nanofibers. *Nano Lett.* , **2003**, 3, 597-602.

104. J. Koehne, J. Li, A. M. Cassell, H. Chen, Q. Ye, H. T. Ng, J. Han and M. Meyyappan, The fabrication and electrochemical characterization of carbon nanotube nanoelectrode arrays *J. Mater. Chem.*, **2004**, 14, 676-684.

105. L. U. Syed, J. Liu, A. M. Prior, D. H. Hua and J. Li, Enhanced electron transfer rates by AC voltammetry for ferrocenes attached to the end of embedded carbon nanofiber nanoelectrode arrays. *Electroanalysis*, **2011**, 23, 1709-1717.

106. L. U. Syed, J. Liu, A. K. Price, Y-f. Li, C. T. Culbertson and J. Li, Dielectrophoretic capture of E. coli cells at micropatterned nanoelectrode arrays. *Electrophoresis*, **2011**, 32, 2358-2365.

107. J. Li, J. E. Koehne, A. M. Cassell, H. Chen, H. T. Ng, Q. Ye, W. Fan, J. Han and M. Meyyappan, Inlaid Multi-walled Carbon Nanotube Nanoelectrode Arrays for Electroanalysis. *Electroanalysis*, **2005**, 17, 15-27.

108. J. Li, Q. Ye, A. Cassell, H. T. Ng, R. Stevens, J. Han and M. Meyyappan, Bottom-up approach for carbon nanotube interconnects. *Applied Physics Letters*, **2003**, 82, 2491-2493.

109. A. V. Melechko, V. I. Merkulov, T. E. McKnight, M. A. Guillorn, K. L. Klein, D. H. Lowndes and M. L. Simpson, Vertically aligned carbon nanofibers and related structures: Controlled synthesis and directed assembly. *J. Appl. Phys.*, **2005**, 97, 041301.

110. T. E. McKnight, V. M. A, M. A. Guillorn, V. J. Merkulov, D. M. J, C. T. Culbertson, S. C. Jacobson, D. H. Lowndes and M. L. Simpson, Effects of Microfabrication Processing on the Electrochemistry of Carbon Nanofiber Electrodes. *J. Phys. Chem. B*, **2003**, 107, 10722-10728.

111. P. U. Arumugam, H. Chen, S. Siddiqui, A. P. Weinrich, A. Jejelowo, J. Li and M. Meyyappan, Wafer-scale fabrication of patterned carbon nanofiber nanoelectrode arrays: A route for development of multiplexed, ultrasensitive disposable biosensors. *Biosens. Bioelectron.*, **2009**, 24, 2818-2824.

112. J. R. Creighton and P. Ho, Introduction to Chemical Vapor Deposition (CVD). **2001**.

113. A. J. Bard, G. Inzelt and F. Scholz, in *Electrochemical Dictionary*, eds. A. J. Bard, G. Inzelt and F. Scholz, Springer Berlin Heidelberg, 2012, ch. 19, pp. 817-912.

114. J. Li and N. Wu, *Biosensors Based on Nanomaterials and Nanodevices*, CRC Press 2013

115. J. Li and M. Meyyappan, in *BioMEMS and Biomedical Nanotechnology*, ed. A. P. L. M. Ferrari, L. J. Lee, Springer US, **2006**, ch. 1, pp. 1-17.

116. P. U. Arumugam, H. Chen, A. M. Cassell and J. Li, Dielectrophoretic Trapping of Single Bacteria at Carbon Nanofiber Nanoelectrode Arrays. *J. Phys. Chem. A*, **2007**, 111, 12772-12777.

117. F. R. Madiyar, L. U. Syed, C. T. Culbertson and J. Li, Manipulation of bacteriophages with dielectrophoresis on carbon nanofiber nanoelectrode arrays. *Electrophoresis*, **2013**, 34, 1123-1130.

118. K. Svoboda and S. M. Block, Biological applications of optical forces. *Annu. Rev. Biophys. Biomol. Struct*, **1994**, 23, 247-285.

119. J. Wu, Acoustical tweezers. *J. Acoust. Soc. Am.*, **1991**, 89, 2140-2143.

120. B. H. Lapizco-Encinas, B. A. Simmons, E. B. Cummings and Y. Fintschenko, Insulator-based dielectrophoresis for the selective concentration and separation of live bacteria in water. *Electrophoresis*, **2004**, 25, 1695-1704.

121. E. Kłodzińska and B. Buszewski, Electrokinetic Detection and Characterization of Intact Microorganisms. *Anal. Chem.*, **2008**, 81, 8-15.

122. M. J. Desai and D. W. Armstrong, Separation, Identification, and Characterization of Microorganisms by Capillary Electrophoresis. *Microbiol. Mol. Biol. Rev.*, **2003**, 67 38-51

123. H. A. Pohl, *Dielectrophoresis: The behavior of neutral matter in nonuniform electric fields*, Cambridge Univ. Press: Great Britain, **1978**.

124. J. Suehiro, R. Hamada, D. Noutomi, M. Shutou and M. Hara, Selective detection of viable bacteria using dielectrophoretic impedance measurement method. *J. Electrostat.*, **2003**, 57, 157-168.

125. M. Castellarnau, A. Errachid, C. Madrid, A. Juárez and J. Samitier, Dielectrophoresis as a Tool to Characterize and Differentiate Isogenic Mutants of *Escherichia coli*. *Biophys. J.*, **2006**, 91, 3937-3945.

126. K. Park, D. Akin and R. Bashir, Electrical capture and lysis of vaccinia virus particles using silicon nano-scale probe array. *Biomed Microdevices*, **2007**, 9, 877-883.

127. J. O. Suehiro, A.; Hatano, T.; Hara,, , *Sens. Actuator B-Chem.*, **2006**, 119, 319-326. .

128. L. Yang, P. P. Banada, M. R. Chatni, K. Seop Lim, A. K. Bhunia, M. Ladisch and R. Bashir, A multifunctional micro-fluidic system for dielectrophoretic concentration coupled with immuno-capture of low numbers of Listeria monocytogenes. *Lab on a Chip*, **2006**, 6, 896-905.

129. M. A. Guillorn, M. D. Hale, V. I. Merkulov, M. L. Simpson, G. Y. Eres, H. Cui, A. A. Puretzky and D. B. Geohegan, Operation of individual integrally gated carbon nanotube field emitter cells. *Appl. Phys. Lett.*, **2002**, 81, 2860-2862.

130. K. B. K. Teo, E.Minoux, L. Hudanski, F. Peauger, J-P. Schnell, L. Gangloff, P. Legagneux, D. Dieumegard, G. A. J. Amaratunga and W. I. Milne, Microwave devices: Carbon nanotubes as cold cathodes. *Nature*, **2005**, 437, 968-968.

131. S. Tuukkanen, J. J. Toppari, A. Kuzyk, L. Hirviniemi, V. P. Hytonen, T. Ihalainen and P.Torma, Carbon Nanotubes as Electrodes for Dielectrophoresis of DNA. *Nano Lett.*, **2006**, 6, 1339-1343. .

132. M. P. Hughes, H. Morgan, F. J. Rixon, J. P. H. Burt and R. Pethig, Manipulation of herpes simplex virus type 1 by dielectrophoresis. *Biochimica et Biophysica Acta (BBA) - General Subjects*, **1998**, 1425, 119-126.

133. M. P. Hughes, H. Morgan and F. J. Rixon, Dielectrophoretic manipulation and characterization of herpes simplex virus-1 capsids. *Eur Biophys J*, **2001**, 30, 268-272.

134. F. R. Madiyar, L. U. Syed, P. U. Arumugam and J. Li, in *Advances in Applied Nanotechnology for Agriculture*, eds. B. Park and M. Appell, American Chemical Society, Washington DC, **2013**, vol. 1143, ch. 6, pp. 109-124.

135. H. Morgan and N. G. Green, Dielectrophoretic manipulation of rod-shaped viral particles. *J. Electrostat.*, **1997**, 42, 279-293.

136. I. Ermolina, J. Milner and H. Morgan, Dielectrophoretic investigation of plant virus particles: Cow Pea Mosaic Virus and Tobacco Mosaic Virus. *Electrophoresis*, **2006**, 27, 3939-3948.

137. M. P. Hughes, H. Morgan, F. J. Rixon, J. P. H. Burt and R. Pethig, Manipulation of herpes simplex virus type 1 by dielectrophoresis. *Biochim. Biophys. Acta*, **1998**, 1425, 119-126.

138. M. P. Hughes, H. Morgan and F. J. Rixon, Dielectrophoretic manipulation and characterization of herpes simplex virus-1 capsids. *Eur. Biophys. J.*, **2001**, 30, 268-272.

139. P. U. Arumugam, H. Chen, S. Siddiqui, J. A. P. Weinrich, A. Jejelowo, J. Li and M. Meyyappan, Wafer-scale fabrication of patterned carbon nanofiber nanoelectrode arrays: A route for development of multiplexed, ultrasensitive disposable biosensors. *Biosens. Bioelectron.*, **2009**, 24, 2818-2824.

140. J. Suehiro, R. Yatsunami, R. Hamada and M. Hara, Quantitative estimation of biological cell concentration suspended in aqueous medium by using dielectrophoretic impedance measurement method. *J. Phys. D-Appl. Phys.*, **1999**, 32, 2814-2820.

141. J. L. Baylon-Cardiel, B. H. Lapizco-Encinas, C. Reyes-Betanzo, A. V. Chavez-Santoscoy and S. O. Martinez-Chapa, Prediction of trapping zones in an insulator-based dielectrophoretic device. *Lab on a Chip*, **2009**, 9, 2896-2901.

142. P. L. Stiles, J. A. Dieringer, N. C. Shah and R. R. Van Duyne, in *Annu.Rev.Anal.Chem.*, 2008, vol. 1, pp. 601-626.

143. K. A. Willets and R. P. VanDuyne, Localized Surface Plasmon Resonance Spectroscopy and Sensing. *Annu. Rev. Phys. Chem.*, **2007**, 58, 267-297.

144. S. Nie and S. R. Emory, Probing Single Molecules and Single Nanoparticles by Surface-Enhanced Raman Scattering. *Science*, **1997**, 275, 1102-1106.

145. R. S. Golightly, W. E. Doering and M. J. Natan, Surface-Enhanced Raman Spectroscopy and Homeland Security: A Perfect Match? *ACS Nano*, **2009**, 3, 2859-2869.

146. M. D. Porter, R. J. Lipert, L. M. Siperko, G. Wang and R. Narayanan, SERS as a bioassay platform: fundamentals, design, and applications. *Chem. Soc. Rev.*, **2008**, 37, 1001-1011.

147. K. L. Y. Wang, J. Irudayaraj, Silver Nanosphere SERS Probes for Sensitive Identification of Pathogens. *J. Phys. Chem. C*, **2010**, 114, 16122-16128.

148. J. D. Driskell, K. M. Kwarta, R. J. Lipert, M. D. Porter, J. D. Neill and J. F. Ridpath, Low-Level Detection of Viral Pathogens by a Surface-Enhanced Raman Scattering Based Immunoassay. *Anal. Chem.*, **2005**, 77, 6147-6154.

149. K. Kneipp, H. Kneipp, I. Itzkan, R. R. Dasari and M. S. Feld, Surface-enhanced Raman scattering and biophysics. *J. Phys. Condens. Matter*, **2002**, 14, R597.

150. R. E. Holt and T. M. Cotton, Surface-enhanced resonance Raman and electrochemical investigation of glucose oxidase catalysis at a silver electrode. *J. Am. Chem. Soc.*, **1989**, 111, 2815-2821.

151. L. Zeiri, B. V. Bronk, Y. Shabtai, J. Eichler and S. Efrima, Surface-Enhanced Raman Spectroscopy as a Tool for Probing Specific Biochemical Components in Bacteria. *Appl. Spectrosc.*, **2004**, 58, 33-40.

152. M. Kahraman, M. Müge Yazici, F. ŞahİN, O. F. Bayrak, E. TopÇu and M. Çulha, Towards single-microorganism detection using surface-enhanced Raman spectroscopy. *Int. J. Environ. Anal. Chem.*, **2007**, 87, 763-770.

153. M. Kahraman, M. M. Yazıcı, F. Şahin and M. Çulha, Convective Assembly of Bacteria for Surface-Enhanced Raman Scattering. *Langmuir*, **2008**, 24, 894-901.

154. K. R. Wigginton and P. J. Vikesland, Gold-coated polycarbonate membrane filter for pathogen concentration and SERS-based detection. *Analyst*, **2010**, 135, 1320-1326.

155. W. R. Premasiri, D. T. Moir, M. S. Klempner, N. Krieger, G. Jones and L. D. Ziegler, Characterization of the Surface Enhanced Raman Scattering (SERS) of Bacteria. *J. Phys. Chem. B*, **2004**, 109, 312-320.

156. I. S. Patel, W. R. Premasiri, D. T. Moir and L. D. Ziegler, Barcoding bacterial cells: A SERS based methodology for pathogen identification. *J. Raman. Spectrosc.*, **2008**, 39, 1660–1672.

157. S. Efrima and L. Zeiri, Understanding SERS of bacteria. *J. Raman Spectrosc.*, **2009**, 40, 277-288.

158. P. L. Stiles, J. A. Dieringer, N.C. Shah and R. P. VanDuyne, Surface-Enhanced Raman Spectroscopy. *Annu.Rev.Anal.Chem.*, **2008**, 1.

159. A. V. Zayats, I. I. Smolyaninov and A. A. Maradudin, Nano-optics of surface plasmon polaritons. *Phys. Rep.*, **2005**, 408 131–314.

160. S. R. Y. Wang, J. Irudayaraj, Separation and detection of multiple pathogens in a food matrix by magnetic SERS nanoprobes. *Anal. Bioanal. Chem.*, **2011**, 399, 1271-1278.

161. B. J. Yakes, R. J. Lipert, J. P. Bannantine and M. D. Porter, Detection of *Mycobacterium avium* subsp. *paratuberculosis* by a Sonicate Immunoassay Based on Surface-Enhanced Raman Scattering. *Clin Vaccine Immunol.*, **2008**, 15, 227-234.

162. E. C. Dreaden, A. M. Alkilany, X. Huang, C. J. Murphy and M. A. El-Sayed, The golden age: gold nanoparticles for biomedicine. *Chem. Soc. Rev*, **2012**, 41, 2740-2779.

163. A. Walter, A. Marz, W. Schumacher, P. Rosch and J. Popp, Towards a fast, high specific and reliable discrimination of bacteria on strain level by means of SERS in a microfluidic device. *Lab Chip*, **2011**, 11, 1013-1021.

164. E. Temur, I. H. Boyacı, U. Tamer, H. Unsal and N. Aydogan, A highly sensitive detection platform based on surface-enhanced Raman scattering for *Escherichia coli* enumeration. *Anal. Bioanal. Chem.*, **2010**, 397, 1595-1604.

165. A. Berthod, J. J. Laserna and J. D. Winefordner, Surface Enhanced Raman Spectrometry on Silver Hydrosols Studied by Flow Injection Analysis. *Appl. Spectrosc.*, **1987**, 41, 1137-1141.

166. K. R. Strehle, D. Cialla, P. Rösch, T. Henkel, M. Köhler and J. Popp, A Reproducible Surface-Enhanced Raman Spectroscopy Approach. Online SERS Measurements in a Segmented Microfluidic System. *Anal. Chem.*, **2007**, 79, 1542-1547.

167. R. Wilson, P. Monaghan, S. A. Bowden, J. Parnell and J. M. Cooper, Surface-Enhanced Raman Signatures of Pigmentation of Cyanobacteria from within Geological Samples in a Spectroscopic-Microfluidic Flow Cell. *Anal. Chem.*, **2007**, 79, 7036-7041.

168. B. Guven, N. Basaran-Akgul, E. Temur, U. Tamer and I. Boyac, SERS-based sandwich immunoassay using antibody coated magnetic nanoparticles for *Escherichia coli* enumeration. *Analyst*, **2011**, 136, 740-748.

169. S. Bhana, E. Chaffin, Y. Wang, S. R. Mishra and X. Huang, Capture and detection of cancer cells in whole blood with magnetic–optical nanoovals. *Nanomedicine*, **2013**, 1-14.

170. S. Bhana, B. K. Rai, S. R. Mishra, Y. Wang and X. Huang, Synthesis and properties of near infrared-absorbing magnetic-optical nanopins. *Nanoscale*, **2012**, 4, 4939-4942.

171. J. Voldman, Electrical forces for microscale cell manipulation. *Annu. Rev. Biomed. Eng.*, **2006**, 8, 425-454.

172. F. R. Madiyar, S. Bhana, L. Z. Swisher, C. T. Culbertson, X. Huang and J. Li, Integration of a nanostructured dielectrophoretic device and a surface-enhanced Raman probe for highly sensitive rapid bacteria detection. *Nanoscale*, **2015**, 7, 3726-3736.

173. D. C. Rodrigues, M. L. de Souza, K. S. Souza, D. P. dos Santos, G. F. S.Andrade and M. L. A. Temperini, Critical assessment of enhancement factor measurements in surface-enhanced Raman scattering on different substrates. *Phys. Chem. Chem. Phys.*, **2015**.

174. A. J. Bonham, G. Braun, I. Pavel, M. Moskovits and N. O. Reich, Detection of Sequence-Specific Protein-DNA Interactions via Surface Enhanced Resonance Raman Scattering. *J.Am.Chem.Soc.*, **2007**, 129, 14572-14573.

175. G. N. Stewart, Researches on circulation time and on the influences which affect it *J. Physiol.*, **1987**, XXII.

176. J. Strassburger, J. Hossbach and R. Seidel, Application of impediometry to rapid assessment of liquid culture media. *Zentralblatt fur Bakteriologie*, **1991**, 274, 481-489.

177. P. Silley and S. Forsythe, Impedance microbiology - A rapid change for microbiologists. *J. Appl. Bacteriol.* , **1996**, 80, 233-243.

178. M. Wawerla, A. Stolle, B. Schalch and H. Eisgruber, Impedance microbiology: Applications in food hygiene. *J. Food Prot.*, **1999**, 62, 1488-1496.

179. R. Gómez-Sjöberg, D. T. Morisette and R. Bashir, Impedance microbiology-on-a-chip: Microfluidic bioprocessor for rapid detection of bacterial metabolism. *Journal of Microelectromechanical Systems*, **2005**, 14, 829-838.

180. R. Gómez, R. Bashir and A. K. Bhunia, Microscale electronic detection of bacterial metabolism. *Sensor Actuator: Chemical*, **2002**, 86, 198-208.

181. S. Siddiqui, P. U. Arumugam, H. Chen, J. Li and M. Meyyappan, Characterization of Carbon Nanofiber Electrode Arrays Using Electrochemical Impedance Spectroscopy: Effect of Scaling Down Electrode Size. *ACS Nano*, **2010**, 4, 955-961.

182. K. Park, D. Akin and R. Bashir, Electrical capture and lysis of vaccinia virus particles using silicon nano-scale probe array. *Biomedical Microdevices*, **2007**, 9, 877-883.

183. M. G. Moisescu, M. Radu, E. Kovacs, L. M. Mir and T. Savopol, Changes of cell electrical parameters induced by electroporation. A dielectrophoresis study. *Biochim. Biophys. Acta Biomembranes*, **2013**, 1828, 365-372.

184. A. G. Pakhomov, D. Miklavcic and M. S. Markov, *Advanced Electroporation Techniques in Biology and Medicine*, CRC Press, **2010**.

185. D. Chen, M. Mauk, X. Qiu, C. Liu, J. Kim, S. Ramprasad, S. Ongagna, W. R. Abrams, D. Malamud, P. Corstjens and H. H. Bau, An integrated, self-contained microfluidic cassette for isolation, amplification, and detection of nucleic acids. *Biomed Microdevices*, **2010**, 12, 705-719.

186. M. M. Bahi, M. N. Tsaloglou, M. Mowlem and H. Morgan, Electroporation and lysis of marine microalga Karenia brevis for RNA extraction and amplification. *J. R. Soc. Interface.*, **2011**, 8, 601-608.

187. J. Kim, M. Johnson, P. Hill and B. K. Gale, Microfluidic sample preparation: cell lysis and nucleic acidpurification. *Integr. Biol.*, **2009**, 1, 574-586.

188. T. S. Pierce, Thermo Scientific Pierce, vol. 2.

189. C. J. Orendorff, A. Gole, T. K. Sau and C. J. Murphy, Surface-Enhanced Raman Spectroscopy of Self-Assembled Monolayers: Sandwich Architecture and Nanoparticle Shape Dependence. *Anal. Chem.*, **2005**, 77, 3261-3266.

190. D. S. Grubisha, R. J. Lipert, H. Y. Park, J. Driskell and M. D. Porter, Femtomolar Detection of Prostate-Specific Antigen: An Immunoassay Based on Surface-Enhanced Raman Scattering and Immunogold Labels. *Anal. Chem.*, **2003**, 75, 5936-5943.

191. M. Dribek, E. Rinnert, F. Colas, M-P. Crassous, N. Thioune, C. David, M. de la Chapelle and C. Compère, Organometallic nanoprobe to enhance optical response on the polycyclic aromatic hydrocarbon benzo[a]pyrene immunoassay using SERS technology. *Environ Sci Pollut Res*, **2014**, 1-7.

192. B. J. Yakes, R. J. Lipert, J. P. Bannantine and M. D. Porter, Impact of Protein Shedding on Detection of Mycobacterium avium subsp. paratuberculosis by a Whole-Cell Immunoassay Incorporating Surface-Enhanced Raman Scattering. *Clin. Vaccine. Immunol.*, **2008**, 15, 235-242.

193. X. Li, I. Barasoain, R. Matesanz, J. Fernando Díaz and W.-S. Fang, Synthesis and biological activities of high affinity taxane-based fluorescent probes. *Bioorganic & Medicinal Chemistry Letters*, **2009**, 19, 751-754.

194. M. A. McClain, C. T. Culbertson, S. C. Jacobson, N. L. Allbritton, C. E. Sims and J. M. Ramsey, Microfluidic Devices for the High-Throughput Chemical Analysis of Cells. *Anal. Chem.*, **2003**, 75, 5646-5655.

195. C. T. Culbertson, T. G. Mickleburgh, S. A. Stewart-James, K. A. Sellens and M. Pressnall, Micro Total Analysis Systems: Fundamental Advances and Biological Applications. *Anal. Chem.*, **2014**, 86, 95-118.

196. T. C. Mockler and J. R. Ecker, Applications of DNA tiling arrays for whole-genome analysis. *Genomics*, **2005**, 85, 1-15.

197. F. Ozsolak and P. M. Milon, RNA sequencing: advances, challenges and opportunities. *Nature reviews. Genetics*, **2011**, 12, 87-98.

198. K. Chandramouli and P. Quain, Proteomics: Challenges, Techniques and Possibilities to Overcome Biological Sample Complexity. *Human Genomics and Proteomics : HGP*, **2009**, 2009, 239204.

199. T. Ramirez, M. Daneshian, H. Kamp, F. Y. Bois, M. R. Clench, M. Coen, B. Donley, S. M. Fischer, D. R. Ekman, E. Fabian, C. Guillou, J. Heuer, H. T. Hogberg, H. Jungnickel, G. Krennrich, G. E. Krupp, A. Luch, F. Noor, E. Peter, B. Riefke, M. Seymour, S. Skinner, L. Smirnova, E. Verheij, S. Wagner, T.Hartung, B. van Ravenzwaay and M. Leist, Metabolomics in Toxicology and Preclinical Research. *ALTEX*, **2013**, 30, 209-225.

200. M. Kliman, J. C. May and J. A. McLean, Lipid Analysis and Lipidomics by Structurally Selective Ion Mobility-Mass Spectrometry. *Biochim. Biophys. Acta*, **2011**, 1811, 935-945.

201. A. M. Streets and Y. Huang, Chip in a lab: Microfluidics for next generation life science research. *Biomicrofluidics*, **2013**, 7, 011302.

202. M. L. Kovarik, D. M. Ornoff, A. T. Melvin, N. C. Dobes, Y. Wang, A. J. Dickinson, P. C. Gach, P. K. Shah and N. L. Allbritton, Micro Total Analysis Systems: Fundamental Advances and Applications in the Laboratory, Clinic, and Field. *Anal. Chem.*, **2013**, 85, 451-472.

203. T. Vilkner, D. Janasek and A. Manz, Micro Total Analysis Systems. Recent Developments. *Anal. Chem.*, **2004**, 76, 3373-3386.

204. A. van den Berg and T. S. J. Lammerink, in *Microsystem Technology in Chemistry and Life Science*, eds. A. Manz and H. Becker, Springer Berlin Heidelberg, **1998**, vol. 194, ch. 2, pp. 21-49.

205. A. K. Price and C. T. Culbertson, Chemical Analysis of Single Mammalian Cells with Microfluidics. *Anal. Chem.*, **2007**, 79, 2614-2621.

206. D. A. Skoog, D. M. West and F. J. Holler, *Fundamentals of Analytical Chemistry*, Saunders College Publishing, Philadelphia, 1996.

207. N-T. Nguyen and S. T. Wereley, *Fundamentals and Applications of Microfluidics*, Artech House, Inc., Boston, 2006.

208. M. J. Madou, *Fundamentals of Microfabrication: The Science of Miniaturization*, CRC Press, Boca Raton, 2002.

209. B. Gale, Highly Specific Detection of Individual Species, http://www.earlywarninginc.com/technologies.php.

210. M. M. Collinson, B. Novak, S. A. Martin and J. S. Taussig, Electrochemiluminescence of Ruthenium(II) Tris(bipyridine) Encapsulated in Sol−Gel Glasses. *Anal. Chem.*, **2000**, 72, 2914-2918.

211. W. Gao, Y. Chen, S. L. J. Xi, Y. Chen, L. Lin and Z. Chen, A novel electrochemiluminescence ethanol biosensor based on tris(2,2′-bipyridine) ruthenium (II) and alcohol dehydrogenase immobilized in graphene/bovine serum albumin composite film. *Biosens. Bioelectron.*, **2013**, 41, 776-782.

212. J. Ballesta-Claver, R. Rodríguez-Gómez and L. F.Capitán-Vallvey, Disposable biosensor based on cathodic electrochemiluminescence of tris (2,2-bipyridine) ruthenium (II) for uric acid determination. *Anal. Chim. Acta*, **2013**, 770, 153-160.

# Appendix A- Culture, Enumeration of Bacteriophages and Dielectrophoresis Experiment using Microelectrode Gap.

## Appendix A.1: Set-up and Culture of Bacteriophages

The cultures were grown in sterilized flasks. Flask A was used for growth of culture, and the flask B was used to trap any overflow of the media and allowed passage for outgoing air. The flasks and tubes were wet-sterilized at 121˚C for 20min, and rubber stoppers were dry-heat sterilized at 160˚C for 4 hours. After cooling, 30 mL of the sterilized nutrient tryptone broth was added to the flask, incubated at 37˚C for overnight. The clear broth in the flask is used to test the sterility of the assembly.

*Bacteriophage* T4r and *E.coli* B stock solutions were obtained from the Carolina Biological Supply Company (121150), and *Bacteriophage* T1 was obtained from ATCC (11303-B1). The host *E.coli* B was grown in a sterile culture tube of nutrient peptone broth medium and incubated overnight at 37˚ C. The concentration of the bacteria obtained was ~2.25 × $10^9$ CFU/mL 0.5 mL of overnight culture of *E.coli* B was used to inoculate 30 mL of the sterile medium in the flask A and incubated for ~2 hours at 37˚C for bacteria to reach mid logarithmic phase. 1 mL of high titer solution of *Bacteriophage* T4r (phage) 1 × $10^9$ pfu/mL was added to the sensitive bacteria solution. Periodic examination of the virus-host culture was done to check the turbidity of the solution. Lysis of the medium began with an hour and indicated by frothing in the solution. Turbidity of the solution decreases as the lysis progresses and eventually turns clear in three hours. The solution is filtered by filter 0.2 μm from Fisher (09-719C) to remove any live bacteria or bacterial debris. The phage culture was stored in the refrigerator at 4˚C with chloroform to kill and to ensure none of the bacteria is in the solution. For the determination of

the titer of the phages, done double layer agar (DLA) method was used. All culture broths and agar was sterilized at 121˚ for 20min.


**Tube A:** It contains Tryptone broth (30 mL) with *E.coli* B (1.0 mL of $2.25 \pm 0.5 \times 10^9$ CFU/mL) and *Bacteriophage* T4r (0.8 mL of $5 \times 10^9$ pfu/mL). This assembly was incubared ar 37°C till the turns clear after the bacteria growth.

**Tube B:** Acts as a buffer for air and overflow of the medium

**Figure A. 1: Culture of *Bacteriophage*T4r set-up**

**(F. R Madiyar et al. unpublished work).**

## Appendix A.2: Double layer agar quantification of Bacteriophages

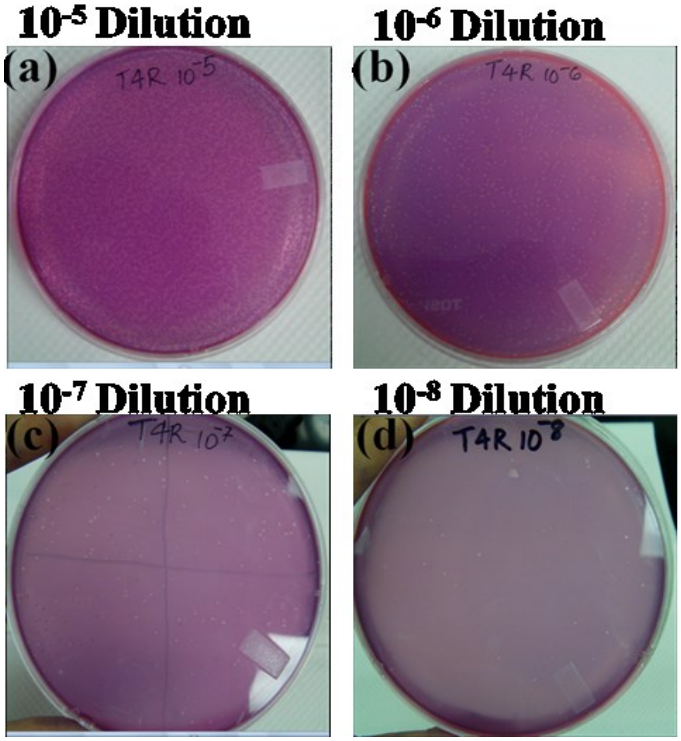


**Figure A. 2: The counting of bacteriophage is carried out by double layer agar (DLA) method**

**(Reprinted with permission from supplementary information of F. R. Madiyar, L. U. Syed, C. T. Culbertson, J. Li, Electrophoresis, 2013, 34, 1123-1130.)**

**Total Number of plaques formed 112 in $10^{-7}$ dilution culture**

**Concentration 1.12 × $10^{9}$ pfu/mL**

The counting of the *Bacteriophage* T4r by double layer agar (DLA) method. A high titer of the phages was serially diluted with nutrient peptone broth by tenfold at each step. DLA plates were prepared by mixing the 100 µl of overnight culture of bacterial host (*E. coli* B) and 1 mL diluted phage in molten soft agar and pouring the mixture on top of the base layer agar. Plates

were incubated overnight at 37˚ C till the plaques were formed. The infective titers of the phages were calculated by the number of plaques formed on the assay plates. Assay dilutions of $10^{-5}$ to $10^{-9}$ were sufficient to determine the titer. The purple-pink color was due to gram staining of *E. coli B*. The transparent spots are plaques formed on the base layer agar. The number of plaque on the plate which could be clearly counted with reliable statistics was used for the concentration calculation.

## Appendix A.3: Transmission Electron Microscope of Bacteriophages

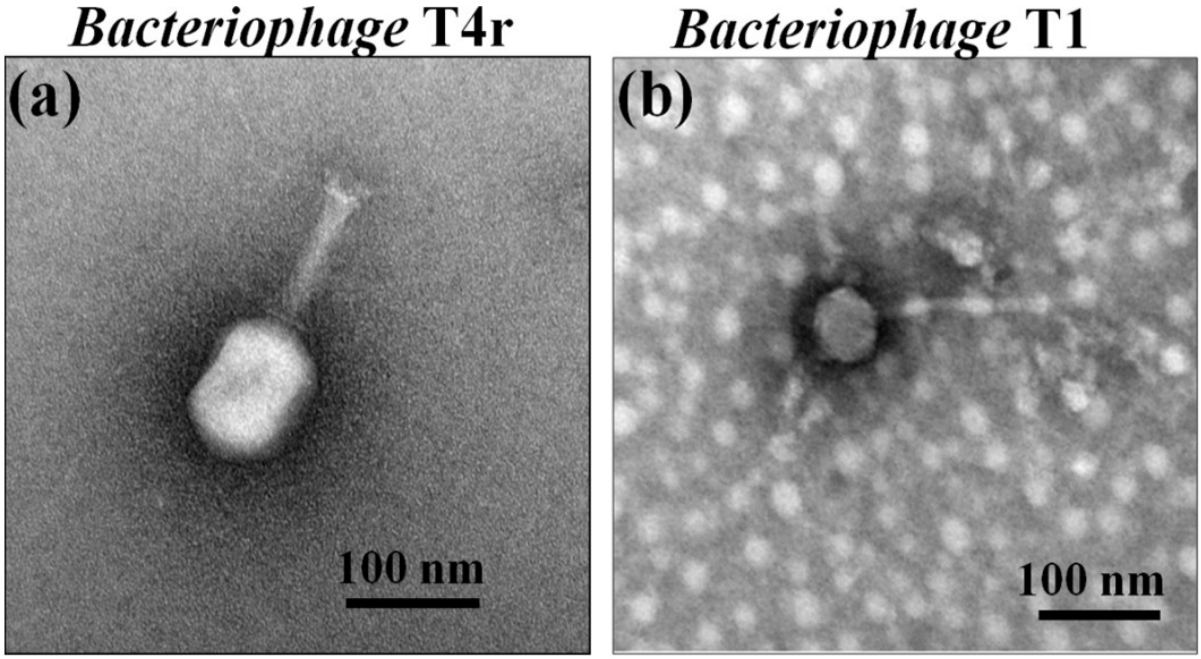


**Figure A. 3: Transmission electron microscope images of the two types of bacteriophages used in this study.**

**(A)** ***Bacteriophage*** **T4r (B)** ***Bacteriophage*** **T1. (Reprinted with permission from supplementary information of F. R. Madiyar, L. U. Syed, C. T. Culbertson, J. Li,** ***Electrophoresis,*** **2013, 34, 1123-1130.)**

## Appendix A.4: Results of SYBR GREEN –I labeling

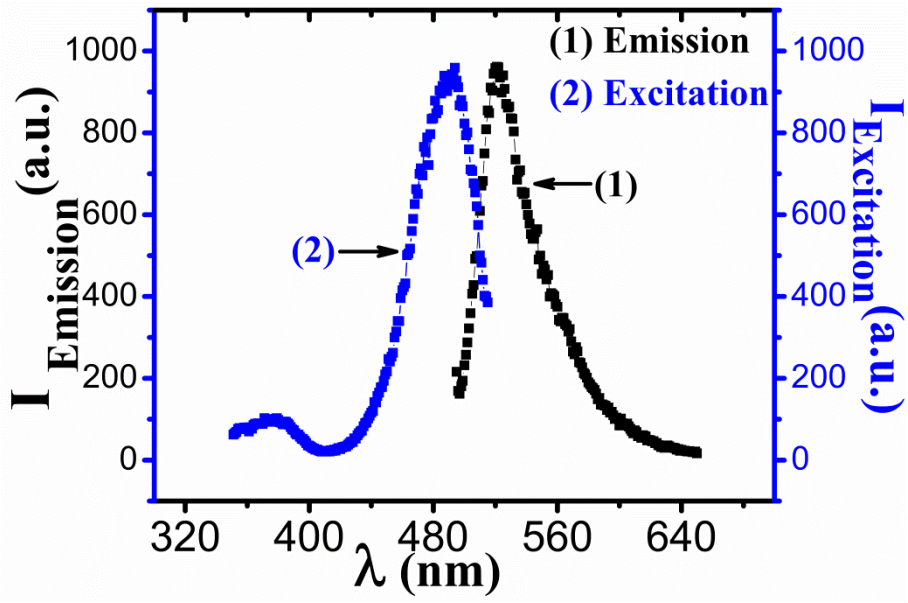


**Figure A. 4: After labeling of the *Bacteriophage* T4r with SYGR Green –I, the excitation and fluorescence emission spectra showing excitation wavelength 490 nm and emission 520 nm.**

**(Reprinted with permission from supplementary information of F. R. Madiyar, L. U. Syed, C. T. Culbertson, J. Li, Electrophoresis, 2013, 34, 1123-1130.)**

Excitation $\lambda_{max}$ : 493.92 nm  Emission λmax: 521.03 nm

## Appendix A.5: Dielectrophoresis Experiment with Microelectrode Gap

To check the dielectrophoresis of *bacteriophages* T4r the experiment was initially carried out using microelectrode. The gap between electrodes is 2.0 µm that is connected with gold contact pad seen in Appendix Figure A6. A 20 µl drop was added on top of the microelectrodes and flattened it with cover slip or PDMS well is used to make solution stay on top of the microelectrodes. The voltage was applied using the pins connected to gold pads seen Figure A5 D using a function generator.

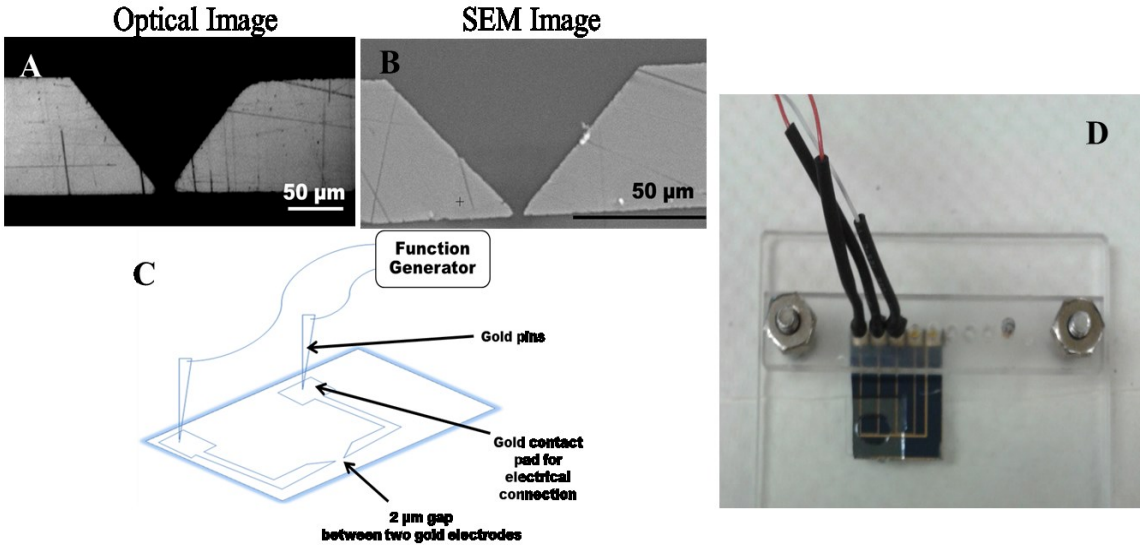


**Figure A. 5: Microelectrode Gap set-up**

**(A) Optical image of the microelectrode gap. (B) Scanning electron microscope image of microelectrode gap. (C) Schematic of the connections of microelectrode gap (D) Image of the set of microelectrode gap.**

**(F. R Madiyar et al. unpublished work)**

## Appendix A.6: Assessing of the Capture of Bacteriophages in Microelectrode Gap

The capture of bacteriophage on the microelectrode gap was successful when voltage is applied at the particular frequency. The appendix A.6A. is a plot was obtained by plotting the fluorescence intensity at the captured area versus the log of the frequency. When voltage of 10 $V_{pp}$ was applied at the frequency of 5.0 kHz in static condition the capture can be observed under optical fluorescence microscope as the phages were labeled with SYBR GREEN I. The snapshots in Figure Appendix A.6 B and C evidently show the phages were captured at the gap.

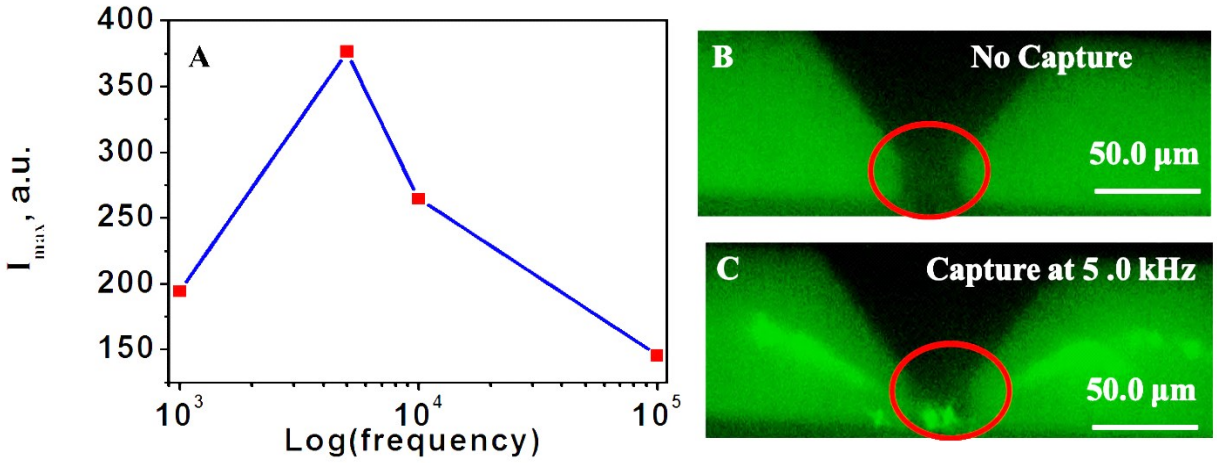


**Figure A. 6: Assessing the capture of bacteriophages at microelectrode gap.**

**(A) The plot of fluorescence intensity maximum at the captured area versus log frequency, showing 5.0 kHz is the optimum frequency for capture at a voltage of 10 $V_{pp}$. (B) Moreover, (C) is the snapshots when no voltage is applied (No capture) and when frequency and voltage are applied (Capture). (F. R Madiyar et al. unpublished work)**

# Appendix B-Supplementary Information of Chapter 5

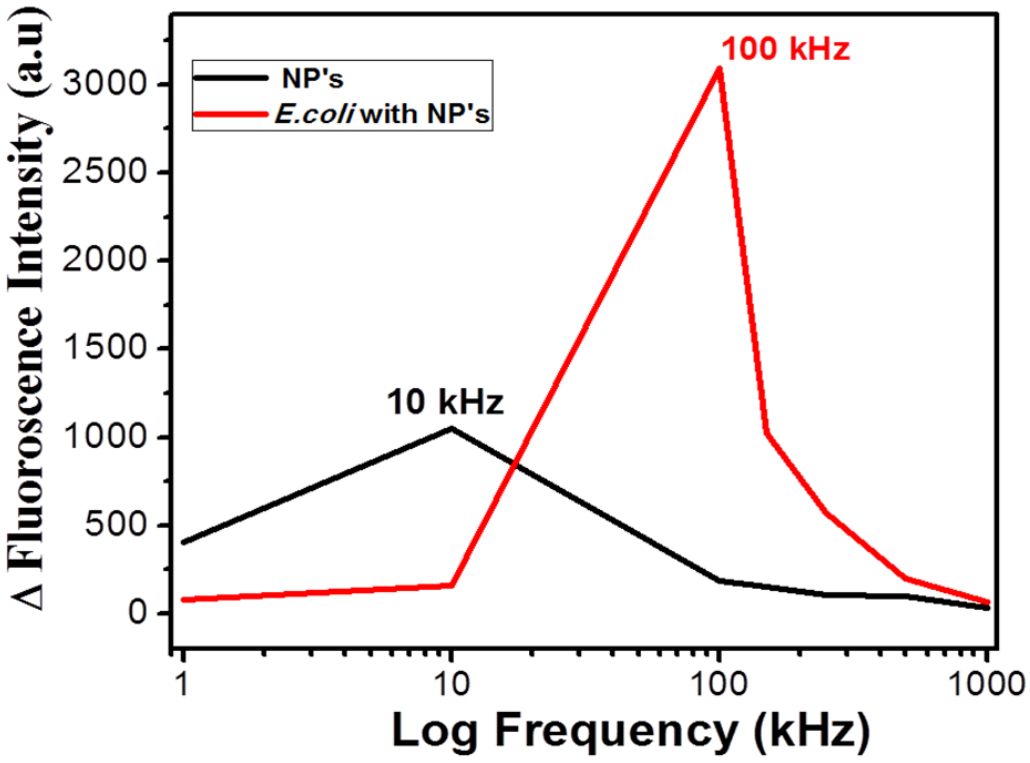


**Figure B. 1: The difference in DEP capture efficiency of IO-Au NOV labeled *E. coli* DHα5 cells and free IO-Au NOV solution, as monitored by the fluorescence intensity change after 50 s of DEP capture. The concentration of IO-Au NOV labeled *E. coli* DHα5 cells is 5.3 × $10^5$ CFU/mL and the concentration of free IO-Au NOV solution is equivalent to the amount of NOVs in the 9 × $10^5$ CFU/mL of labeled *E. coli* sample. The DEP experiments were carried out at the varying frequency from 1 kHz to 1000 kHz while other parameters are fixed: voltage (10 $V_{pp}$) and flow velocity (0.33 mm/s). The capture of free IO-Au NOV at 100 kHz is negligible. (Reprinted with permission from supplementary information F. R. Madiyar, S. Bhana, L. Z. Swisher, C. T. Culbertson, X. Huang, J. Li, *Nanoscale*, 2015, 7, 3726-3736.)**

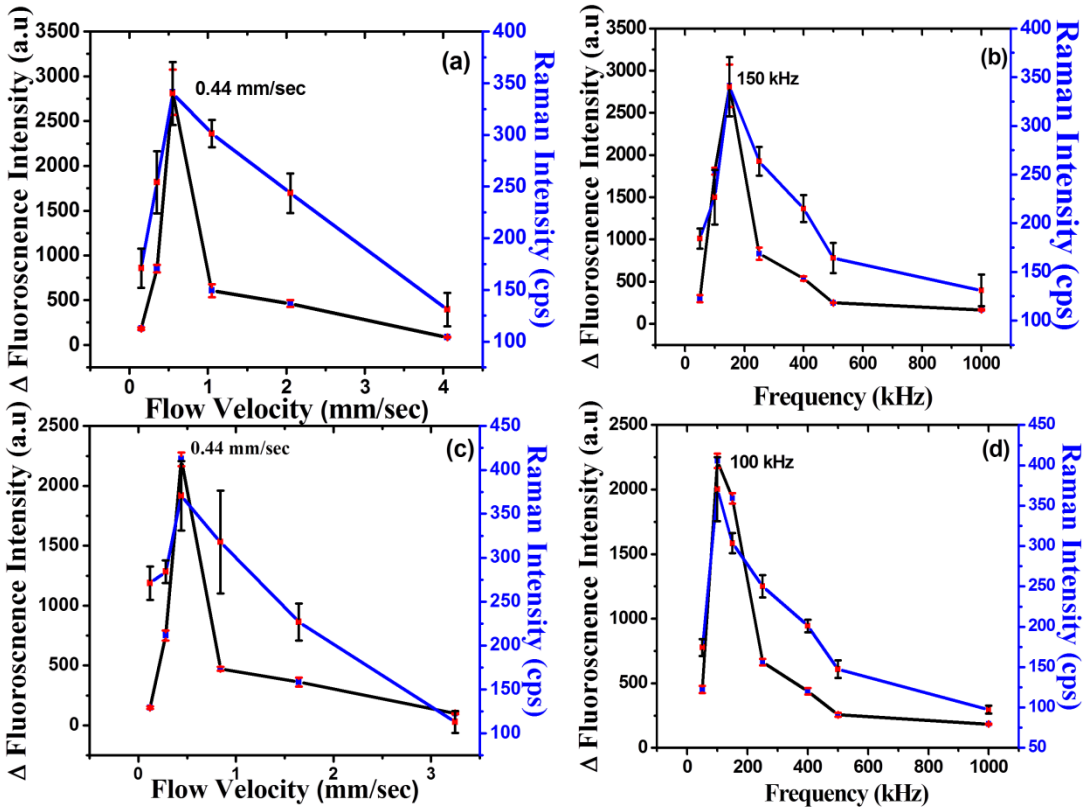


**Figure B. 2: Assessing DEP capture of IO-Au NOV labeled *E. coli* DHα5 cells in complex matrices by fluorescence and the confocal Raman measurements. The DEP capture of 5 × $10^5$ CFU/mL of *E. coli* DHα5 cells spiked in the chicken broth (A) at varying AC frequency and (B) at varying flow velocity. The optimum conditions are 150 kHz in frequency and 0.44 mm/sec in flow velocity. The DEP capture of 5 × $10^5$ CFU/mL of *E. coli* DHα5 cells spiked in soil solution (C) at varying AC frequency and (D) at varying flow velocity. The optimum conditions are 100 kHz in frequency and 0.44 mm/sec in flow velocity. . (Reprinted with permission from supplementary information F. R. Madiyar, S. Bhana, L. Z. Swisher, C. T. Culbertson, X. Huang, J. Li, *Nanoscale*, 2015, 7, 3726-3736.)**

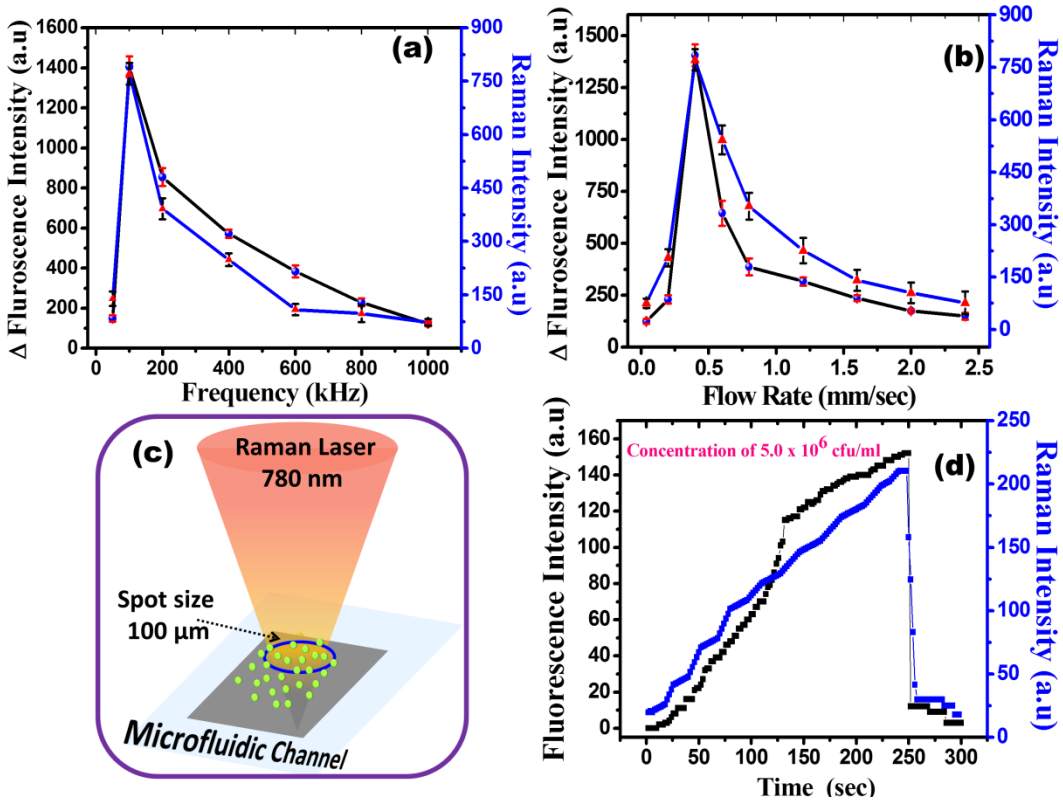


**Figure B. 3: Assessing DEP capture of 5.3 × $10^5$ CFU/mL of IO-Au NOV labeled *E. coli* DHα5 cells with fluorescence and the portable Raman system (A) at varying AC frequency and (B) at varying flow velocity. The optimum frequency of 100 kHz and optimum flow velocity of 0.40 mm/sec were observed. (C) Schematic diagram of 100 µm diameter laser probe focused on the active DEP area of the microfluidic device. (D) The kinetic DEP capture curves measured at an AC frequency of 100 kHz and a voltage of 10 $V_{pp}$ while 5 × $10^6$ CFU/mL IO-Au NOV labeled *E. coli* DHα5 cells flowing through the DEP device at 0.40 mm/sec flow velocity. (Reprinted with permission from supplementary information F. R. Madiyar, S. Bhana, L. Z. Swisher, C. T. Culbertson, X. Huang, J. Li, *Nanoscale*, 2015, 7, 3726-3736.)**

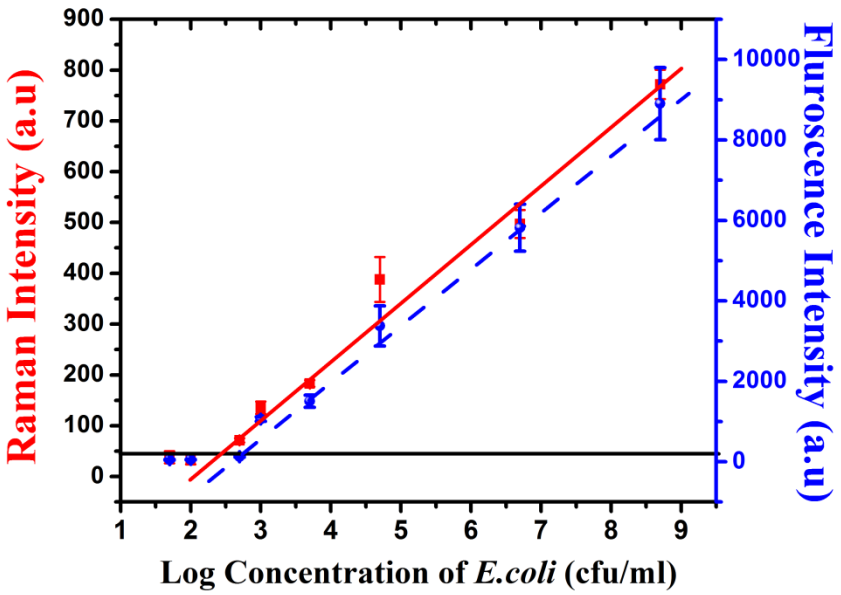


**Figure B. 4: The increase in the Raman (left) and fluorescence (right) intensity after 50 s of DEP capture of *E. coli* cells from the bacteria solution as the concentration varying from 5 CFU/mL to 1.0 × $10^9$ CFU/mL. The Raman measurements were carried out by focusing the 100-µm-diameter laser beam within the 200 µm × 200 µm active DEP area with a ProRaman L portable Raman system (Enwave Optronics). The fluorescence intensity was integrated over the whole 200 µm × 200 µm active DEP area with the CCD videos recorded using Carl Zeiss microscope (50X objective at excitation wavelength of 540-552 nm and emission wavelength of 567-647 nm). (Reprinted with permission from supplementary information F. R. Madiyar, S. Bhana, L. Z. Swisher, C. T. Culbertson, X. Huang, J. Li, *Nanoscale*, 2015, 7, 3726-3736.)**

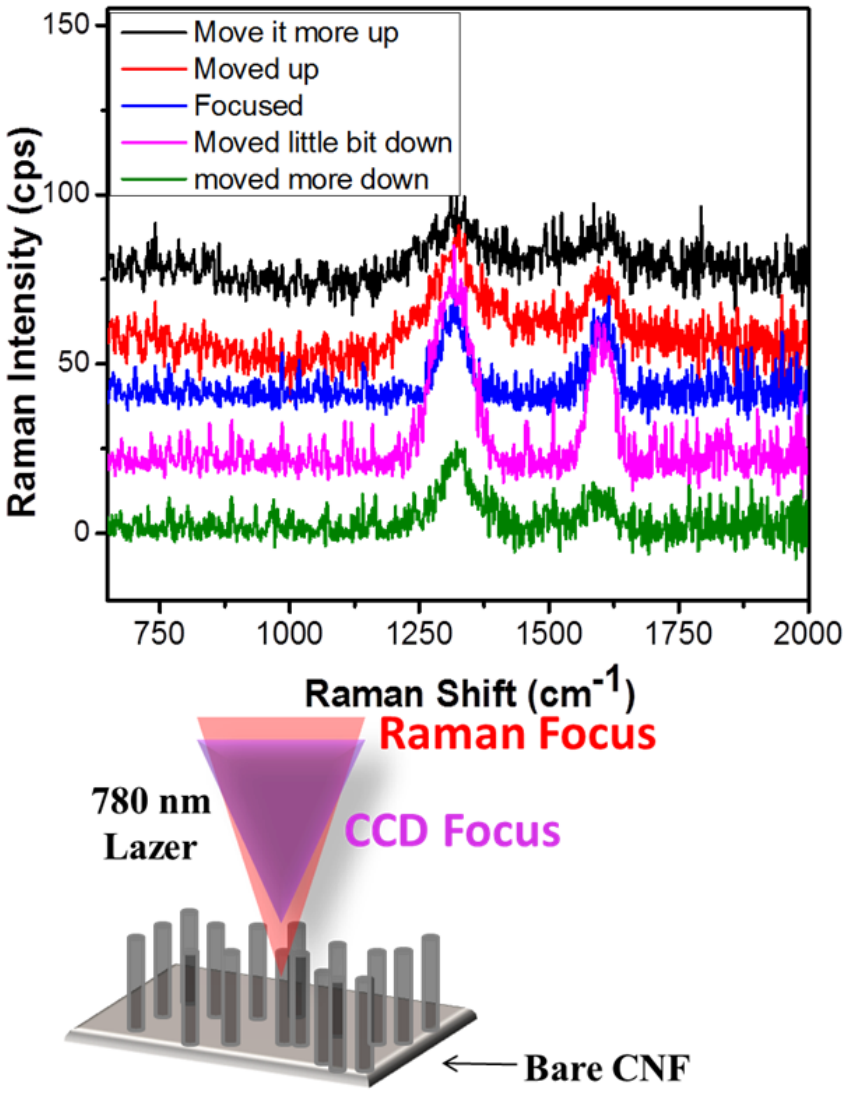


**Figure B. 5: Focusing of the vertically aligned carbon nanofiber Raman signal on confocal Raman microscope by the controlled motion of Z stage (F. R. Madiyar et al. unpublished work).**

# Appendix C- Supplementary Information for Chapter 6

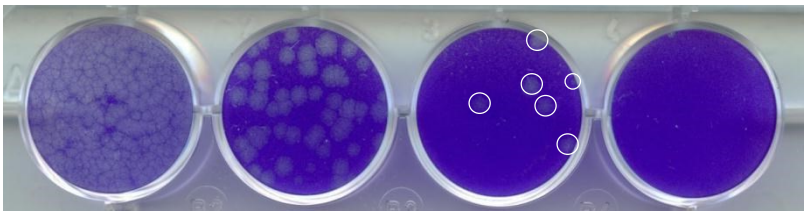

VC-2, untreated

**Figure C. 1: Standard plaque assay on RK-13 cells in a 12-well plate of the cells for counting the number of plaques formed in each dilution and calculating back to the total plaque-forming units per milliliter (pfu/mL) of the original stock. (Foram R. Madiyar, Sherry Basset, Luxi Swisher, Christopher T Culbertson, Stefan Rothenberg and Jun Li; "Nano-Dielectrophoresis capture and Electroporation of Vaccinia virus by Impedance Method. (F. R. Madiyar et al. unpublished work).**

Plaque forming unit = 1 infection particle

pfu/ml = (pfu/well) × (1/dilution factor) × (1/ml of inoculum)

Count plaques in lowest dilution having between 5-100 pfu/well

For VC-2:

6 pfu/well x $(1/10^{-7})$ x (1/0.3ml inoculum) = **$2.0 \times 10^{8}$ pfu/ml**

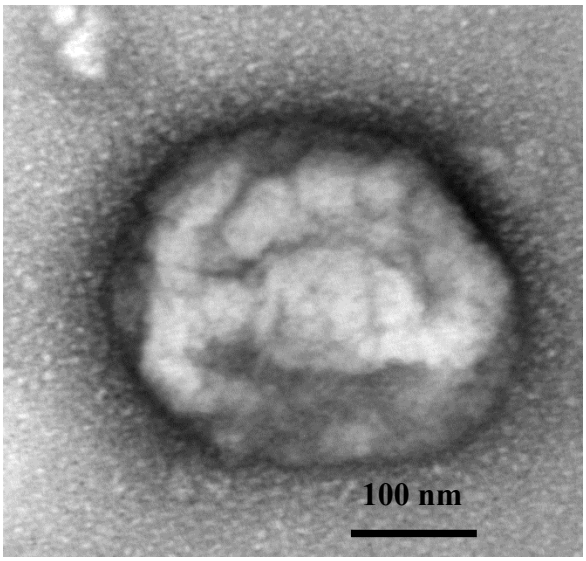


**Figure C. 2: Transmission Electron Microscope Image of *Vaccinia* virus with average diameter of 312 nm ± 0.5 nm. (Foram R. Madiyar, Sherry Basset, Luxi Swisher, Christopher T Culbertson, Stefan Rothenberg and Jun Li; "Nano-Dielectrophoresis capture and Electroporation of Vaccinia virus by Impedance Method. (F. R. Madiyar et al. unpublished work).**

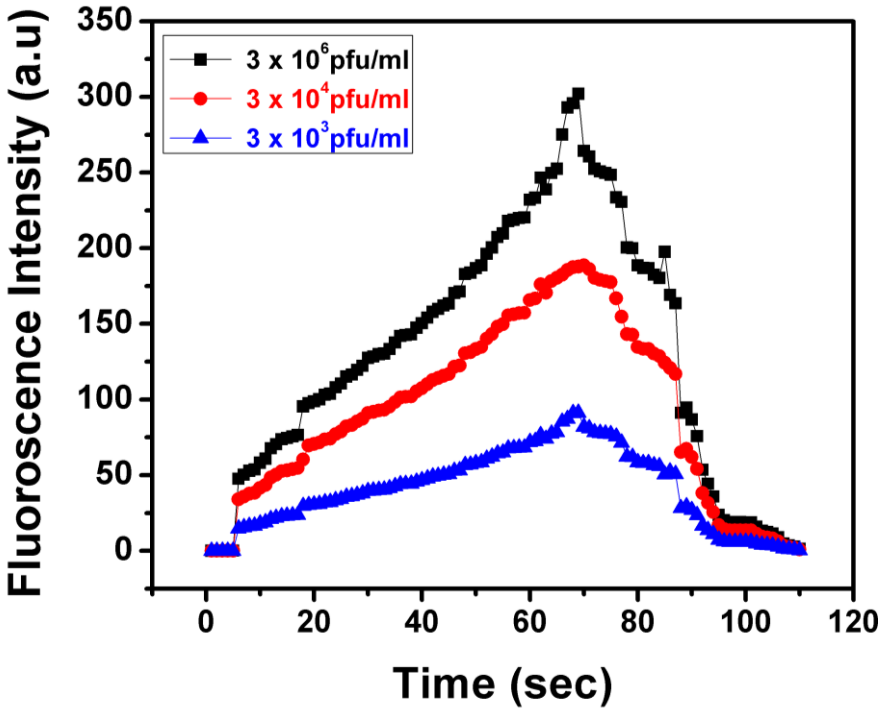


**Figure C.3: Real-time fluorescence capture of *Vaccinia* virus are various concentrations 3 × $10^3$ pfu/mL (blue), 3 × $10^4$ pfu/mL (red), 3 × $10^6$ pfu/mL (black). (Foram R. Madiyar, Sherry Basset, Luxi Swisher, Christopher T Culbertson, Stefan Rothenberg and Jun Li; "Nano-Dielectrophoresis capture and Electroporation of Vaccinia virus by Impedance Method. (F. R. Madiyar et al. Unpublished work).**

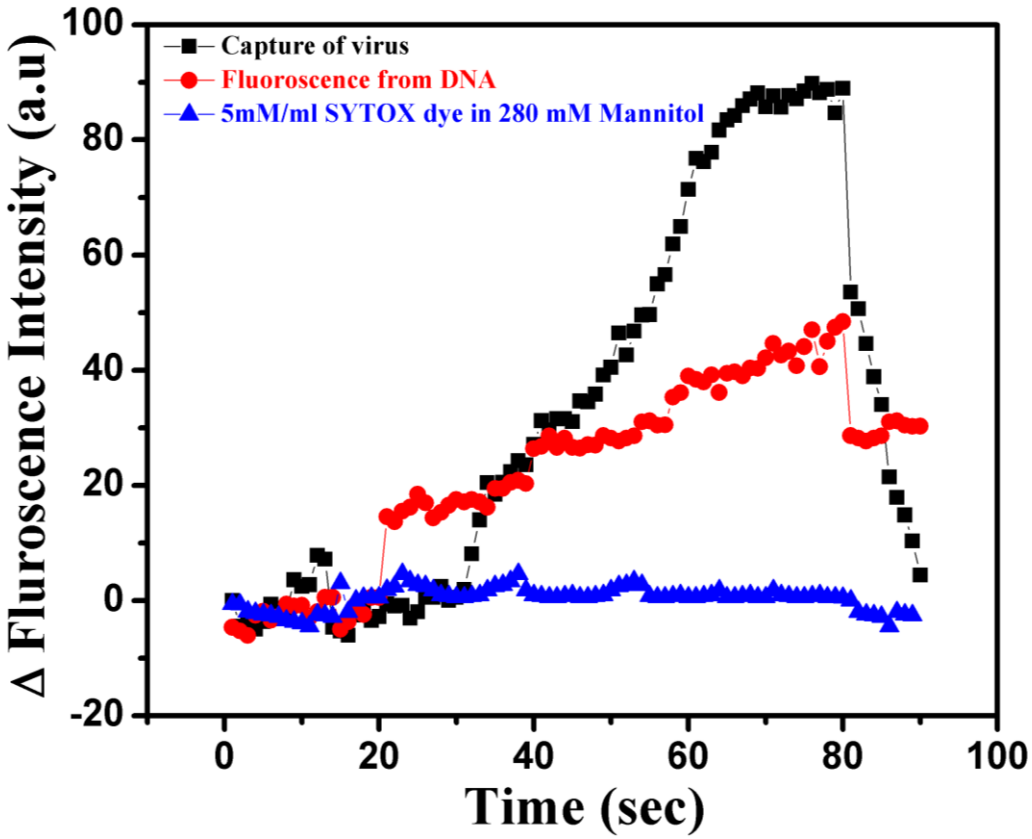


**Figure C. 4: Real-time electroporation of the Vaccinia virus**

**The lipophilic membrane of the viruses is stain with DiO dye that can be observed using filter 3 in Carl Zeiss microscope (black), after electroporation the DNA of the virus is stained with cell impermeable SYTOX 59 dye (red) and the SYTOX 59 dye in 280 mM Mannitol solution as a control (blue). (Foram R. Madiyar, Sherry Basset, Luxi Swisher, Christopher T Culbertson, Stefan Rothenberg and Jun Li; "Nano-Dielectrophoresis capture and Electroporation of Vaccinia virus by Impedance Method. (F. R. Madiyar et al. Unpublished wor)).**

# Appendix D-List of Publications and Presentations

## PUBLICATIONS

- **Foram R. Madiyar**, Sherry Basset, Luxi Swisher, Stefan Rothenberg and Jun Li; "Nano-Dielectrophoresis capture and Electroporation of *Vaccinia* virus by Impedance Method." In preparation.

- **Foram R. Madiyar**, Saheel Bhana, Luxi Swisher, Xiaohua Huang, Christopher Culbertson, and Jun Li; "Integration of Nano-Dielectrophoretic Bacteria Capture and Surface-Enhanced Raman Detection." Nanoscale, 2015,(7), pages 3726-3736. **DOI:** 10.1039/C4NR07183B.

- Luxi Swisher, Allan M. Prior, Medha J. Gunaratna, Stephanie Shishido, **Foram R. Madiyar**, Thu A. Nguyen, Duy H. Hua, and Jun Li; "Quantitative Electrochemical Detection of Cathepsin B Activity in Breast Cancer Cell Lysates Using Carbon Nanofiber Nanoelectrode Arrays and Its Correlation with Cancer Progression." Submitted in *Nanomedicine.*

- **Foram R. Madiyar**, Lateef Syed, Christopher Culbertson, and Jun Li; "Manipulation of Bacteriophages with Dielectrophoresis on Carbon Nanofiber Nanoelectrode Arrays," *Electrophoresis* 2013, 34 (7) pages 1123-1130**.**

  **Front page cover in Special Issue of *Electrophoresis* (2013). DOI: 10.1002/elps.201200486**.

- Luxi Swisher, Lateef U. Syed, Allan M. Prior, **Foram R. Madiyar**, Kyle R. Carlson, Thu A. Nbuyen, Duy H. Hua, and Jun Li; "Electrochemical Protease Biosensor Based on Enhanced AC Voltammetry Using Carbon Nanofiber Nanoelectrode Arrays," *J. Phys. Chem C,* 2013, 117 (8) pages 4268–4273. **DOI:** 10.1021/jp312031u.

## BOOK CHAPTERS

- **Foram R. Madiyar**, Lateef Syed, Prabhu Arumugam, and Jun Li; "Electrical Capture and Detection of Microbes Using Dielectrophoresis and Nanoelectrode Array," *Advances in Applied Nanotechnology for Agriculture, ACS books*, Chapter 6, pages 109-124. **Chapter DOI:** 10.1021/bk-2013-1143.ch006.

- Jun Li**, Foram R. Madiyar**, Luxi Swisher; "Carbon nanomaterials with special architectures for biomedical applications," *Carbon Nanomaterials for Biomedical Applications*, Submitted to Carbon Nanomaterials for Biomedical Applications, editors Liming Dai, Rajesh Naik, Mei Zhang, Springer.

## CONFERENCE PRESENTATIONS

- **Foram R. Madiyar**, Saheel Bhana, Luxi Swisher, Xiaohua Huang, Christopher Culbertson, and Jun Li; "Integration of Nano-Dielectrophoretic Bacteria Capture and Surface-Enhanced Raman Detection," 249th ACS National Meeting in Denver, Colorado, Division: Division of Agricultural and Food chemistry, Session: Applied Nanotechnology for Food and Agriculture, March 25, 2015.

- Chao Wang, **Foram Madiyar**, Jun Li, and Chenxu Yu; "Multiplex self-referencing SERS pathogen detection using microfluidics" *Sensors and Biosensors, 2015 Annual Meeting*, St. Louis, MO, March 5-7, 2015

- **Foram R. Madiyar**, Saheel Bhana, Luxi Swisher, Xiaohua Huang, Christopher Culbertson, and Jun Li; "Integration of Nano-Dielectrophoretic Bacteria Capture and Surface-Enhanced Raman Detection," *49th Midwest Regional Meeting of American Chemical Society*, November 13, 2014.

- **Foram R. Madiyar**, Saheel Bhana, Luxi Swisher, Xiaohua Huang, Christopher Culbertson, and Jun Li; "Integration of Nano-Dielectrophoretic Bacteria Capture and Surface-Enhanced Raman Detection," *Kansas Physical Chemistry Symposium*, October 18, 2014.

- Chao Wang, **Foram Madiyar**, Jun Li, and Chenxu Yu; "A Self-Referencing Detection of Pathogens Using Surface Enhanced Raman Scattering Nanoprobes in a nano-DEP Microfluidic Biosensor," *24th Anniversary World Congress on Biosensors*, Melbourne, April 14, 2014.

- **Foram R. Madiyar**, Lateef Syed, Christopher Culbertson, and Jun Li; "Dielectrophoretic Capture Viruses on Vertically Aligned Carbon Nanofibers," *University of Missouri*, Columbia, 4th *Annual Nanofrontier's Symposium*, June 6, 2013.

- **Foram R. Madiyar**, Jianwei Liu, Alex Price, Yifen Li, Christopher Culbertson, Lateef Syed, and Jun Li; "Using Dielectrophoresis for Reversible Capture and Release of *E. coli* cells at Micro-patterned Nanoelectrode Arrays," *46th Midwest Regional Meeting of the American Chemical Society***,** October 20, 2011.

## POSTER PRESENTATIONS

- **Foram R. Madiyar**, Saheel Bhana, Luxi Swisher, Xiaohua Huang, Christopher Culbertson, and Jun Li; "Integration of Nano-Dielectrophoretic Bacteria Capture and Surface-Enhanced Raman Detection," *Silicon Prairie International Microfluidics Symposium*, University of Kansas, November 1, 2014.

- **Foram R. Madiyar**, Lateef Syed, Christopher Culbertson, and Jun Li; "Dielectrophoretic Phenomenon used for Rapid Capture and Detection of Pathogens," *K-State Research Summit*, August 2013.

- **Foram R. Madiyar**, Lateef Syed, Christopher Culbertson, and Jun Li; "Dielectrophoretic Capture Viruses on Vertically Aligned Carbon Nanofibers," *University of Missouri*, Columbia, 4th *Annual Nanofrontier's Symposium*, June 6, 2013.

- **Foram R. Madiyar**, Lateef Syed, Christopher Culbertson, and Jun Li; "Dielectrophoretic Capture Viruses on Vertically Aligned Carbon Nanofibers," *K-State Research Summit*, August 2012.